Accretion History of Super Massive Black Hole

Tesi di dottorato di:

Cocchia Filomena

Filomena Cocchia
2005

Abstract

Since their discovery in 1960's Active Galactic Nuclei (AGN) became, due to their remarkable features, one of the most mysterious and intriquing objects in the Universe. Today theoretical and observational evidences suggest that they are closely linked to the formation and evolution of galaxies and cosmic structures. The study of the nuclear activity, its cosmological evolution and correlation with the assembly and evolution of galaxies and with the environment is one of the primary goal of observational cosmology.

However, despite more than 40 years of study, a comprehensive picture of AGN (and galaxy) evolution is still lacking. AGNs have been studied in all accessible wavebands but hard X-rays turn out to be the most efficient band to a) discriminate accretion-powered sources, such as AGNs, from normal galaxy; b) obtain samples less biased against highly obscured sources; and c) probe the physical processes occuring in the heart of the active galaxies and their evolution with cosmic time. Deep X-ray surveys could be performed only starting from the last decade, using first the concentrators on board ASCA and BeppoSAX. Another breakthrough occurred at the end of the 90' with the launch of Chandra and XMM-Newton, with their X-ray telescopes with much higher throughput and arcsec image quality. Chandra and XMM-Newton are performing both ultra-deep, pencil beam surveys, to probe accretion up the highest redshifts and lower nuclear luminosities and wide area surveys, to probe higher luminosity AGN on wide redshift intervals. Both surveys are clearly needed to obtain a uniform coverage of the redshift-luminosity plane and therefore to study AGN evolution on wide luminosity and redshift ranges.

In the context of the wide area surveys, we performed the HELLAS2XMM survey, which provides a sample of hard X–ray sources detected in ~ 2 square deegres at 2-10 keV fluxes in the range of $\sim 10^{-14} \div 10^{-12}\ ergcm^{-2}s^{-1}$. The large area covered, and the hard X-ray selection allowed us to obtain a statistically significant sample of high luminosity, highly obscured sources (type 2 QSOs), detected at fluxes where a significant fraction ($\sim 50\%$) of the X-ray background (XRB) is resolved. These type 2 QSOs have fluxes higher than the analogous sources in the ultra-deep surveys, and therefore their optical counterparts are accessible to spectroscopy with 8m class telescopes. Indeed we were able to obtain a spectroscopic redshifts for one of the largest samples of type 2 QSOs ever identified.

We used the HELLAS2XMM survey, together with other deeper surveys like the Chandra Deep Field South and North surveys, to derive, over a wide range of redshifts and luminosities, the luminosity function of obscured and unobscured AGNs and its evolution. We then compared these luminosity functions with predictions of semianalitical models for the formation and evolution of the structure in the Universe. Although such models compute self-consistently both the Black Hole (BH) mass and accretion rate, the present data do not allow to disentangle the contribution of BH mass and accretion to the observed luminosity function; in fact, different accretion rate and BH masses can combine to yield the same luminosity function. To constraint more tightly the specific predictions of the models a better approach would be to compare them to, mass, or accretion rate, selected AGN luminosity functions. This comparison can help in both disentangling among competing models, and in understanding the role of relative feedbacks and delays between nuclear activity, star formation and galaxy evolution.

We envisaged a strategy to attack this problem. A first steep was the study of the optical and near infrared morphology of the host galaxies of highly obscured type 2 AGN.

This can allow us to estimate their bulge luminosity and therefore the mass of the central BH, using the well known correlations between bulge properties and BH mass. A second step was the estimate of the BH mass of unobscured type 1 AGN through the width of their Broad Emission Lines. We present the first results of these two approaches.

Desiderata

.....

Take kindly the counsel of the years,
gracefully surrendering the things of youth.
Nurture strength of spirit to shield you in sudden misfortune.
But do not distress yourself with dark imaginings.
Many fears are born of fatigue and loneliness.
Beyond a wholesome discipline,
be gentle with yourself.

You are a child of the universe,
no less than the trees and the stars;
you have a right to be here.
And whether or not it is clear to you,
no doubt the universe is unfolding as it should.

Therefore be at peace with God,
whatever you conceive Him to be,
and whatever your labors and aspirations,
in the noisy confusion of life keep peace with your soul.

With all its sham, drudgery, and broken dreams,
it is still a beautiful world.
Be cheerful.
Strive to be happy.

M. Ehrmann

A mamma e papà,
.....

Contents

Chapter 1

Introduction

One of the still open astrophysical questions is the evolution of Active Galactic Nuclei (AGN).
Since their discovery in 1960's AGNs became, due to their remarkable features, one of the most mysterious and almost pathological objects in the Universe.
Today theoretical and observational evidences suggest that they are closely linked to the formation and evolution of galaxies and cosmic structures.
Consequentely, to trace nuclear activity and its evolution along the assembly history of galaxies as a function of redshift and environment is one of the primary goals of observational cosmology.
AGNs have been studied in all accessible wavebands but the hard X-ray band turn out to be the most efficient to discriminate accretion-powered sources, such as AGNs, and to understand the evolution of the physical processes occuring in the heart of the active galaxies.

1.1 Generalities - The SMBH paradigm - Unification Models

All observed AGNs share several remarkable traits:

- They are extremely louminous, $10 \div 100$ times the total optical luminosity of

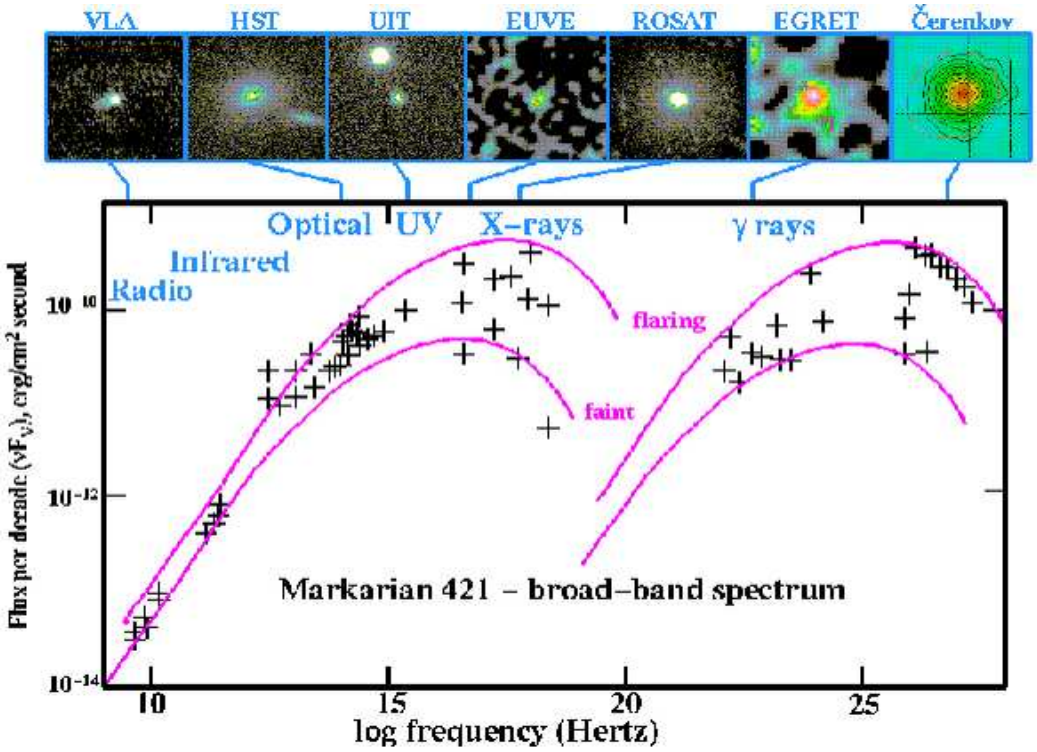

FIGURE 1.1. Active nuclei are among the few kinds of astronomical objects which are prominent across the whole electromagnetic spectrum. This figure illustrates the spectrum of Markarian 421, a BL Lacertae object, from the radio to extreme gamma–ray regimes, in both bright (flaring) and faint states.

the brightest galaxies, with bolometric luminosity of $10^{41} \div 10^{48}\ erg/s$.

- AGNs are unique among objects of the universe in the observable span of their spectra.
  Their broad-band emission covers basically the whole observable electromagnetic spectrum, from the radio to the $\gamma - ray$ band, covering almost 20 orders of magnitude in frequency, i.e. Fig. 1.1.

- Their continuum spectrum is not a Planck spectrum of thermal radiation as in ordinary stars and galaxies.
  To a sufficient approximation it is well represented by a power law $f_\nu \propto \nu^{-\alpha}$, where α ranges typically between $0 - 1$[a], over all frequencies, Fig 1.2.

[a]The mean value of α, the dispersion of this value, and even the validity of the power law parameterization as well as the evolution of such parameters with redshift are still under debate (Pentericci et al. 2003 and reference therein).

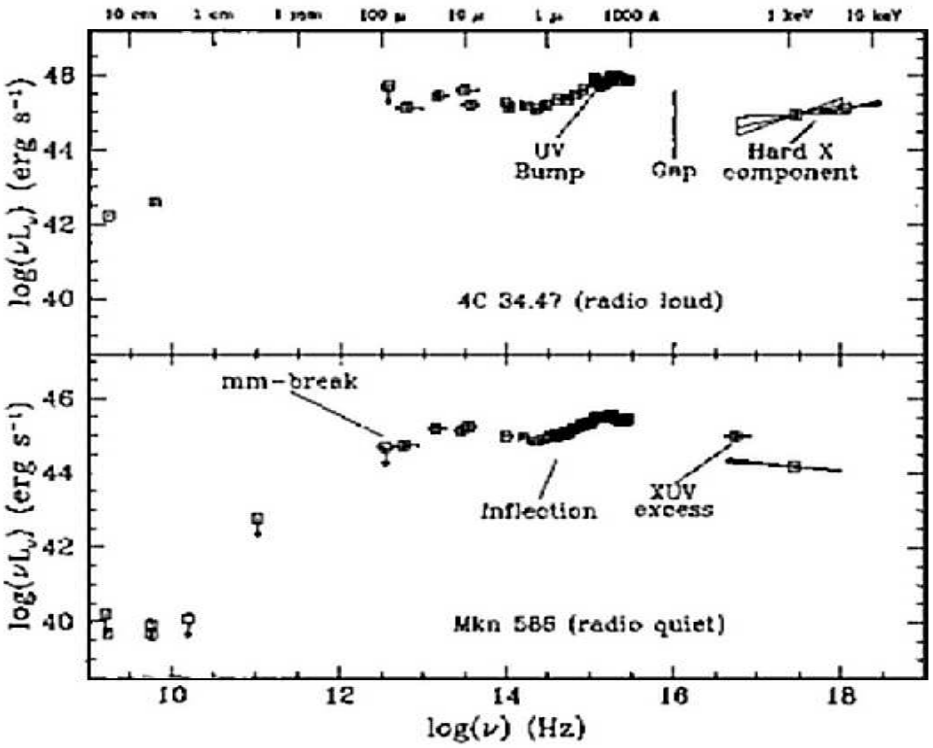

FIGURE 1.2. Examples of radio-loud (4C 34.47, top) and radio-quiet (Mrk 586, bottom) quasar energy distributions, illustrating the main continuum features. The energy distributions show the logarithm of the energy per unit logarithmic frequency interval, in the rest frame. Elvis et al 1994.

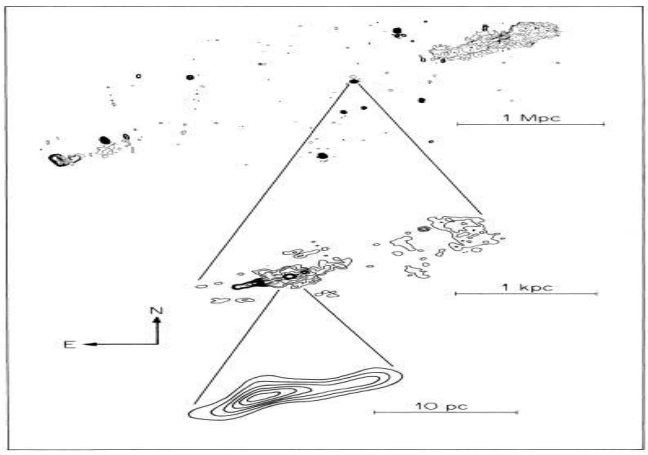

FIGURE 1.3. Composite map showing the radio morphology of 3C236; linear scale are indicated.

– RADIO

AGNs whose continuum properties at all other parts of the spectrum appear almost identical can have drastically different radio powers, as shown in Fig. 1.2.

Two main classes are present in the classification schemes of AGNs: radio-loud ($L_{5GHz}/L_B > 10$) and radio-quiet (otherwise) AGNs.

The radio spectra of the central compact sources in AGNs are flat, and thus radiation is generally taken to be non–thermal in origin, with a synchrotron mechanism usually invoked.

The flatness of the radio spectrum is attribuited to a complex source structure (Fig. 1.3).

– INFRARED

The nuclear infrared continuum is generally associated to AGN emission reprocessed by dust, either in the putative torus or on somewhat larger scales (Narrow Line Region, see sect.1.1.2).

The observed emission is thus a function not only of the AGN luminosity but also of the distribution of the obscuring matter.

Three strong pieces of evidence support the thermal interpretation of the IR continuum:

* the 1μm minimum, thought to represent the minimum between a hot thermal spectrum (the "big blue bump") and a cool thermal spectrum due to emission by warm, $T \leq 2000K$, dust grains (the smooth bump

at wavelengths longward of 1μm is often referred as the IR-bump);

* the IR continuum variability shows the same variations as the UV/optical continuum but with a significant time delay interpreted as light travel time effect due to the separation between the UV/optical and IR emitting regions.
  The picture that emerges is that within the sublimation radius[b], dust is destroyed. Farther out, however it survives and is heated by the UV/optical radiation from the central source to approximately the equilibrium blackbody temperature.
  The IR continuum arises as this energy is re–radiated by the dust;
* the submillimeter break: the sharp cut–off is not reproduced by a synchrotron self–absorbed spectrum; instead, a thermal spectrum can well reproduce it as the emitting efficiency of small grains is a sensitive function of frequency, so the emitted spectrum can have a very strong frequency dependence (Draine and Lee 1984).

– UV/OPTICAL
  The UV/Optical continuum is chracterized by the so-called "big blue bump" which is attribuited to integrated emission of thermal radiation from regions with different temperature of an accretion disk surrounding a supermassive black hole (see sect.1.1.1; Fig. 1.9): models show that the sovrapposition of black body radiation (temperatures in the range $T = 10^{5\pm1}$ K) yields a maximum at wavelengths longward of $\sim 100\dot{A}$.

– X
  The typical broad band UV-X-γ ray spectrum of a Seyfert galaxy has been reported in Fig. 1.4.
  We clearly see different components (apart from the UV bump already discussed):

  * A strong emission in the X-ray band which can be generally fitted by a cut-off power law shape with a power law photon index $\Gamma \simeq 1.9$ (Nandra and Pounds 1994; Fabian 1996; Petrucci 2002) and a cut-off energy E_c near 200–300 keV.
  * A neutral fluorescence FeK line near 6.4 keV.
  * A bump peaking near $30keV$.

[b]The minimun distance from the AGN at which grains of a given composition can exist.

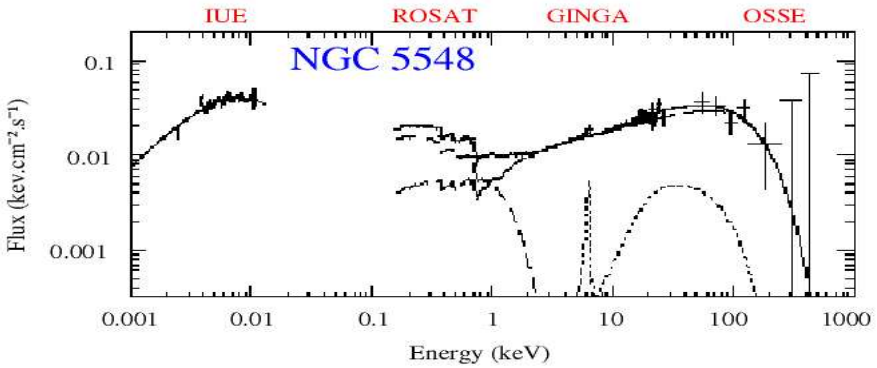

FIGURE 1.4. Typical broadband $UV - X - \gamma$ ray spectrum of a Seyfert galaxy. This spectrum has been obtained from quasi simultaneous observations of different satellites indicated in the figure. Petrucci 2002.

* A soft component below 2 keV, in excess to the extrapolation of the high energy power law, called the soft excess.

These different components are generally interpreted in the reprocessing upscattering model framework.
The scheme of this model is reported in Fig. 1.5.

It supposes the presence of 2 phases, a cold one, the accretion disc, which produces the UV emission, and a hot one, the corona, a plasma of energetic particles, supposed to radiate X-rays by Compton upscattering the UV photons coming from the disc. Inversely, part of the X-ray emission

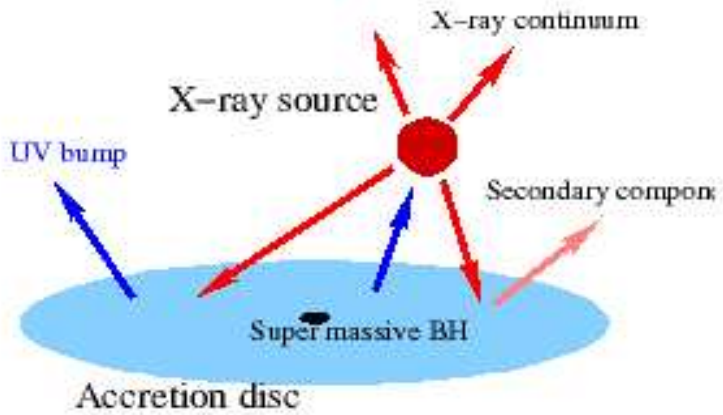

FIGURE 1.5. Schematic view of the reprocessing/upscattering model. Petrucci 2002.

of the corona is absorbed by the cold material and reprocessed in X-ray. Finally, part of the X-ray emission ($\sim 10\%$) is Compton reflected on the disc surface and give birth to the fluorescent Iron line and the reflection bump.
The origin of the soft excess is still unclear, it may be the hard tail of the disc emission.

- γ
  $\sim 10\%$ of all AGNs are γ–ray emitters. All γ–ray emitters are bright in the MeV band (Mukherjee et al. 1999) but for a number of sources the spectrum extends up to TeV (Punch et al. 1992, Piron et al. 2001).
  Variability is very fast in γ–ray band.
  Blazars are radio loud AGNs whose jet is pointing toward us. The spectral energy distribution (SED) of the radiation emitted by the jets can be directly observed, Fig. 1.1.
  The jet models explain the radio to UV continuum from blazars as synchrotron radiation from high–energy electrons in a relativistically out–flowing jet that has been ejected from an accreting supermassive black hole. The emission in the MeV–GeV range is believed to be due to the inverse Compton scattering of low–energy photons by the same relativistic electrons in the jet. However, the source of the soft photons that are inverse Compton scattered remains unresolved: they can originate as synchrotron emission either from within the jet ("synchrotron self–Compton" (SSC) mechanism, e.g., Maraschi, Ghisellini, Celotti 1992; Bloom & Marscher 1996), or from a nearby accretion disk ("external radiation Compton" (ERC) mechanism, e.g., Dermer & Schlickeiser 1994), or they can be disk radiation reprocessed in broad–line region (BLR) clouds.

- Their radiation is characterized by strong emission lines (narrow lines with Full Width at Half Maximum – FWHM $\sim 10^3$ km/s; broad with FWHM up to $\sim 10^4$ km/s), while ordinary stars and galaxies produce light with strong absorption lines (Fig. 1.6).

- Their radiation is variable (Fig.1.7) in every waveband they have been studied. Typical time scales (dt) range from minutes to few months so, on the basis of simple causality arguments ($R \leq cdt$), much of the radiation must came from regions of order of light days in size ($\sim$ pc).

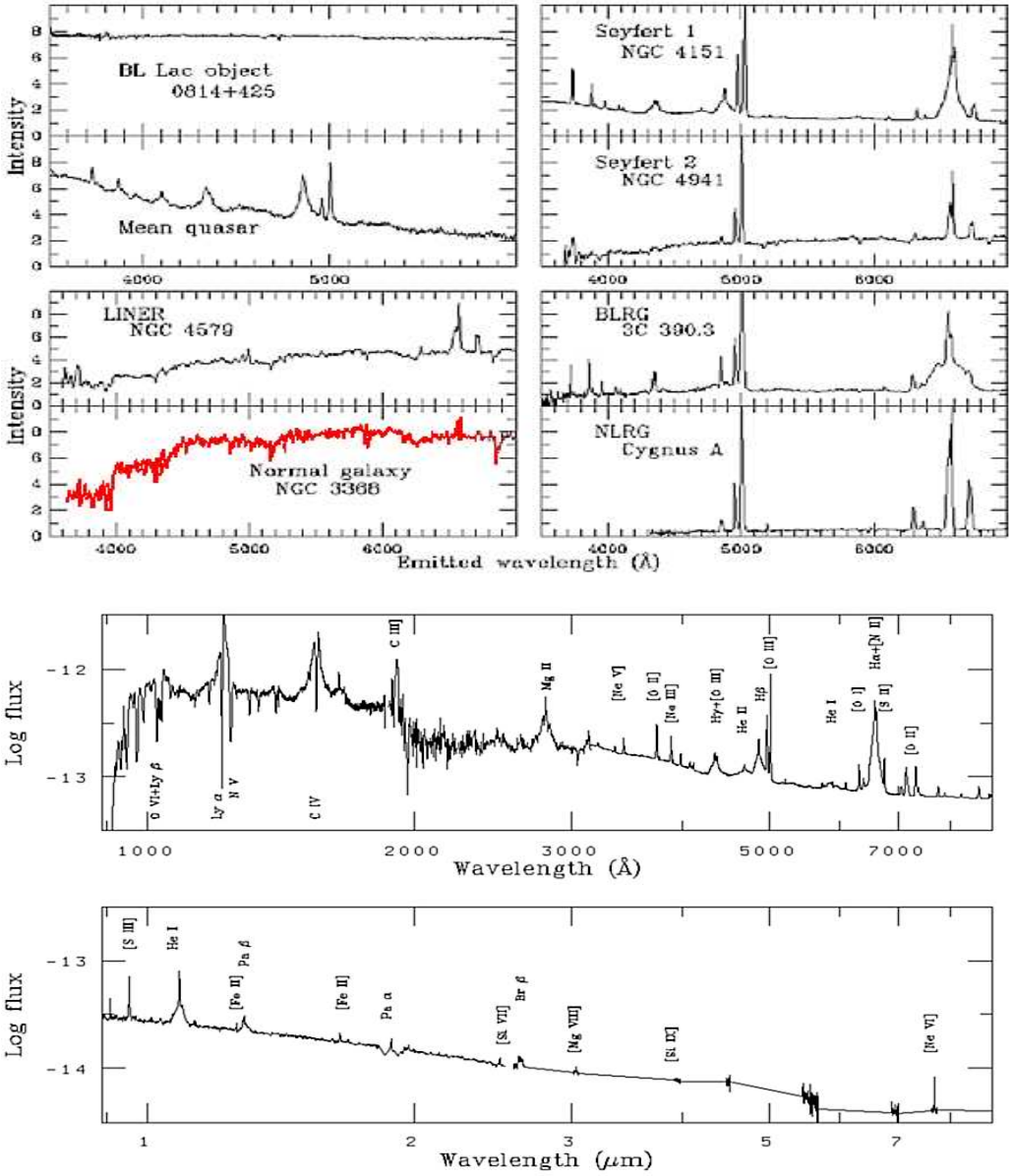

FIGURE 1.6. Upper – Many of the distinctions among the various flavors of AGN rely on spectroscopic clues: BL Lacertae objects have virtually featureless spectra, making even their redshifts difficult to measure unless the surrounding galaxy can be detected; lower activity levels are present in LINERs galaxies; Seyfert 1 and Broad Line Radio Galaxies show broad emission lines (Type 1) while Seyfert 2 and Narrow Line Radio Galaxies (Type 2) show narrow emission lines. A normal galaxy typical spectrum is reported for comparison.

Bottom – This composite spectrum of the archetypal Seyfert NGC 4151 shows the wide variety of emission lines present, from the Lyman limit at 912 A to the mid-infrared at about 9 microns. NGC 4151 is a bit unusual in showing strong absorption in several lines, especially Lyman alpha and C IV. The absorption is blueshifted with respect to the line centers, so that it arises in some kind of wind or other gaseous outflow.

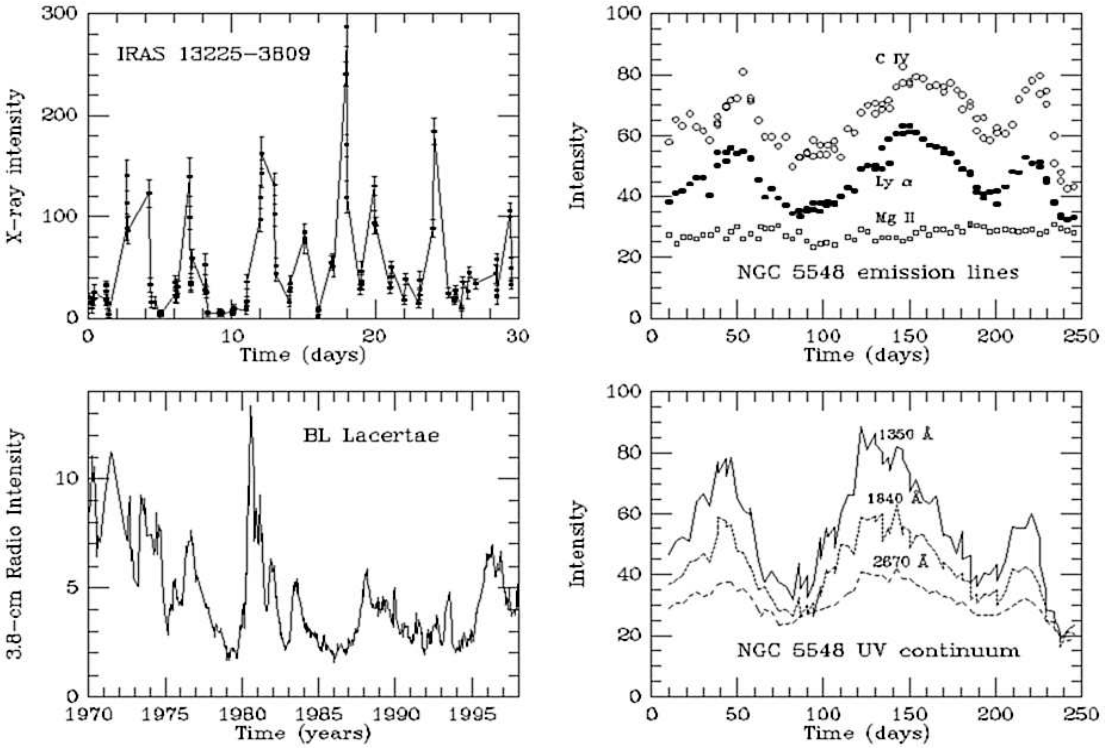

FIGURE 1.7. This graph compares three objects showing characteristic kinds of variability.

BL Lacertae show a series of flares over a 28–year period.

A recent discovery has been that the class of Seyfert nuclei known as narrow-line Seyfert 1 (having the broad lines of type 1 Seyferts but with some of the narrowest widths ever seen for these lines) are continually and strongly variable in the X-ray range, as seen in the ROSAT data series of the Seyfert IRAS 13224–3809. Several Seyfert galaxies have been the subjects of intense spectroscopic campaigns to enable reverberation mapping of their nuclei.

The data here are from a series of IUE observations of NGC 5548, with the continuum measured at three ultraviolet wavelengths compared to three strong emission lines which have very different ionization levels and so might be expected to arise in quite different regions. The continuum is most variable in the deep ultraviolet, as can be seen by comparing the three continuum bands. The Lyman alpha and C IV emission lines follow the continuum changes closely, indicating that they come from areas a few light–days in extent, while Mg II hardly changes at all, coming from a region at least light–months in radius. More sophisticated modelling suggests that the shapes as well as sizes of these regions differ as well.

The most puzzling features is that an AGNs produce huge luminosities in a volume significantly smaller than a cubic parsec.
These luminosities in such a small volumes, in the conventional view, are attributed to the presence of super massive black holes (SMBHs) in the centers of the galaxies (as already metioned above).
The physical arguments which underlie this view are very basic, and date back at least as far as Zel'dovich & Novikov 1964 and Salpeter 1964.

1.1.1 The SMBH paradigm

Luminosity generation can be accounted for in many ways; in principle, simply putting enough star together could create arbitrarily high luminosities.
The most shocking discovery for AGNs came with the realization that their luminosity arise from volumes far too small to contain the star needed to account for energy generation by nuclear processes. That is why AGNs were recognized as being really different from processes normally associated with galaxies: something other than the energy of nuclear fusion had to be used.
The simplest way to produce huge energy outputs is to utilize the gravitational energy.
Systems dependent on gravitational energy, such as gas clouds, dense star cluster and supermassive stars all undergo an inexorable runaway as the central potential well gets deeper and deeper: the almost inevitable endpoint of all these systems will be the collapse to a black hole (Fig. 1.8).
Furthermore, physical processes involving black holes offer a more efficient power supply than any of the "precursor" objects depicted in Fig. 1.8 (Rees 1984).
The prevailing picture of the physical structure of AGNs is illustrated in Fig. 1.9: this structure offer a simple way to explain all the features mentioned above.

The black hole paradigm is supported by a number of observations.
Black holes can be detected through the gravitational effects they produce: the motion of gas and stars on parsec scales has provided irrefutable dynamical evidence for the presence of $10^6 - 10^9$ $M_\odot$ black holes (BHs) in active galaxies Fig. 1.10 (Kormendy & Richstone 1995).
Moreover, dynamical evidence for the existence of a massive black hole in AGNs comes from high spatial resolution VLBI observations of water masers[c]: i.e., in the

[c]This emission is produced by the $6_{16} - 5_{23}$ rotational transition of H_2O at a rest frequency of 22.235080 GHz.

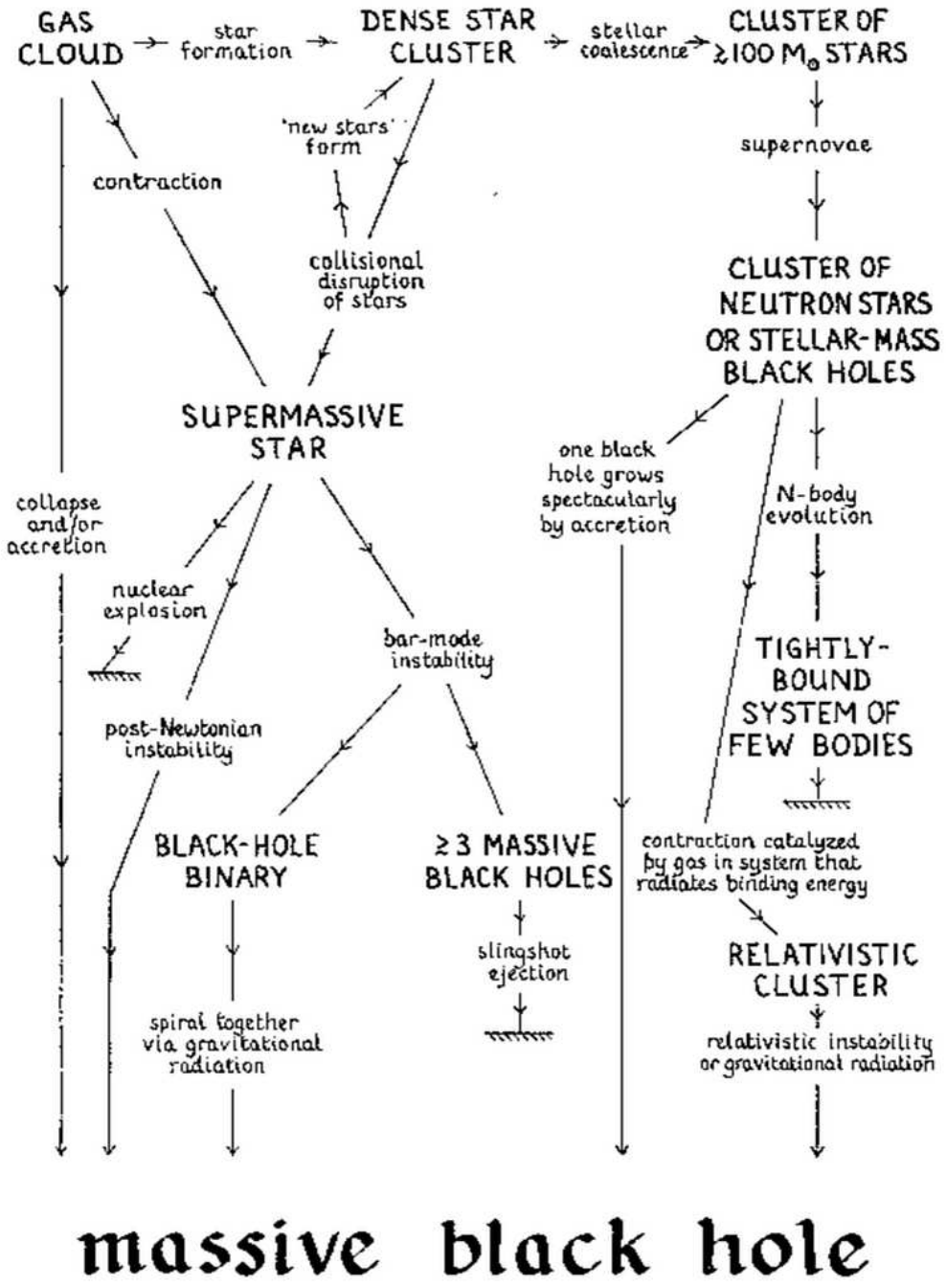

FIGURE 1.8. Schematic diagram showing possible routes for runaway evolution in active galactic nuclei. Rees 1984.

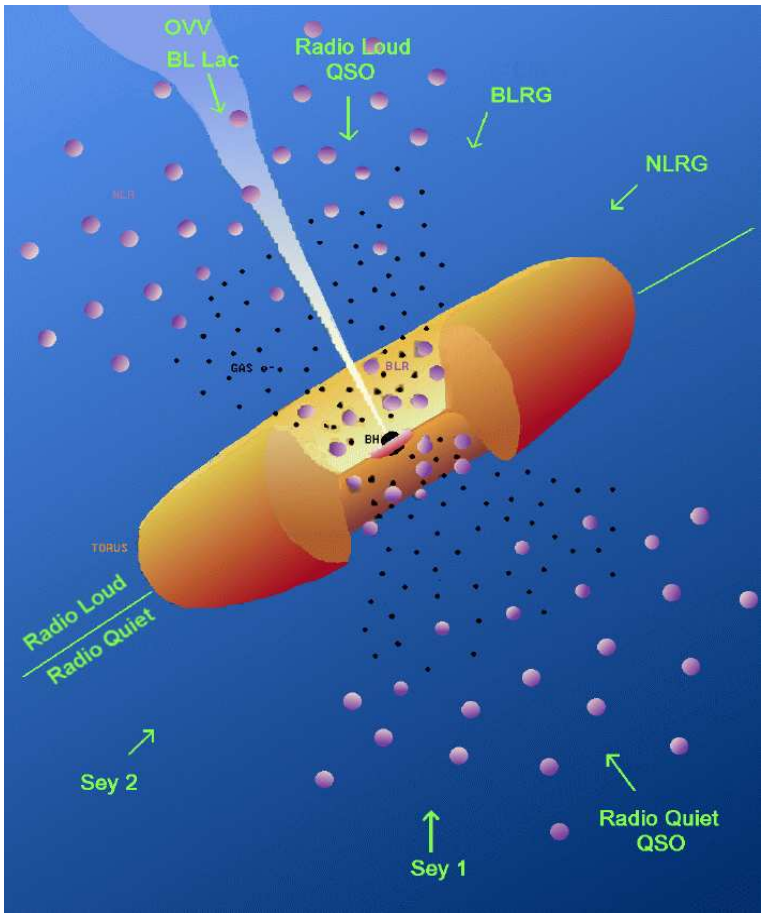

FIGURE 1.9. At the center is a SMBH whose gravitational potential energy is the ultimate source of the extreme AGN luminosity. Matter pulled toward the SMBH loses angular momentum through viscous or turbolent processes in an accretion disk, which glows brightly at ultraviolet and X–ray wavelengths.
Hard X-ray emission is produced very near the black hole, perhaps in connection with the corona above the disk.
Strong optical and ultraviolet emission lines are produced in clouds of gas moving rapidly in the potential of the SMBH, clouds forming the so–colled "Broad–Line Region" (BLR; dark blobs in Fig...).
The optical and ultraviolet radiation is obscured along some line of sight by a torus or warped disk of gas and dust well outside the accretion disk and BLR. Beyond the torus, slowing moving clouds, forming the so-colled "Narrow–Line Region" (NLR), produce emission lines with narrower widths (grey blobs).
Outflows of energetic particles may occur along the poles of the disk or torus, escaping and forming collimated radio–emitting jets. The plasma in the jets, at least on the smallest scales, streams outward at very high velocities, beaming radiation relativistically in the forward direction.

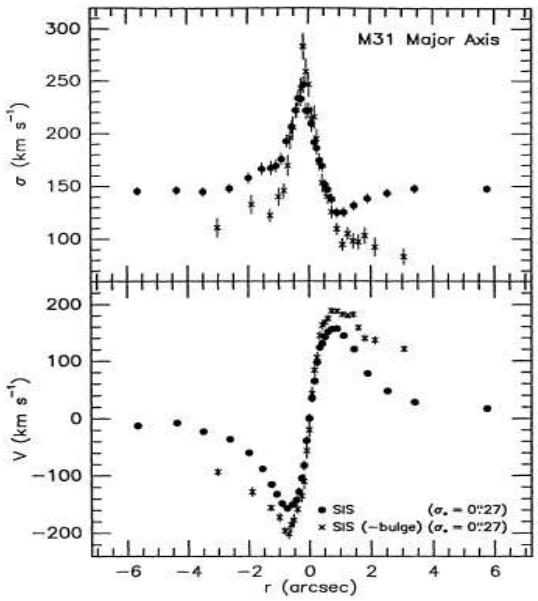

FIGURE 1.10. $V(r)$ and $\sigma(r)$ along the nucleus mjor axis of M31. Filled circles show the kinematics of the nucleus plus bulge as observed; crosses show the nuclear kinematics after the bulge spectrum is subtracted. (from Kormendy & Richstone 1995).

nucleus of the active galaxy NGC 4258 observations reveal the existence of a slightly warped, thin, edge–on accretion disk (Miyoshi et al. 1995).
The rotation curve of the masers, located at disk radii between 0.14 and 0.28 pc is Keplerian (Fig.1.11); the inferred binding mass is $3.9 \times 10^7\ M_\odot$, for a calculated distance of 7.2 Mpc (Bragg et al. 2000 and reference therein).

The center of our Galaxy itself has drawn much attention for the possible presence of a supermassive black hole.
Indirect support for a central black hole in our own Milky Way arose from the discovery of the unusual radio source Sgr A*; its nonthermal spectrum (see, e.g., Serabyn et al. 1997; Beckert et al. 1996), compact size (Rogers et al. 1994), and lack of detected motion (Backer 1994) led researchers to associate it with the putative black hole.
Definitive proof regarding the existence of a massive central black hole and its association with Sgr A* lies in the assessment of the distribution of mass in the central few parsecs of the Galaxy: the peaks of both the stellar surface density and the velocity dispersion are consistent with the position of the radio source and black hole candidate Sgr A*, which suggests that Sgr A* is coincident ($\pm 0''.1$) with the

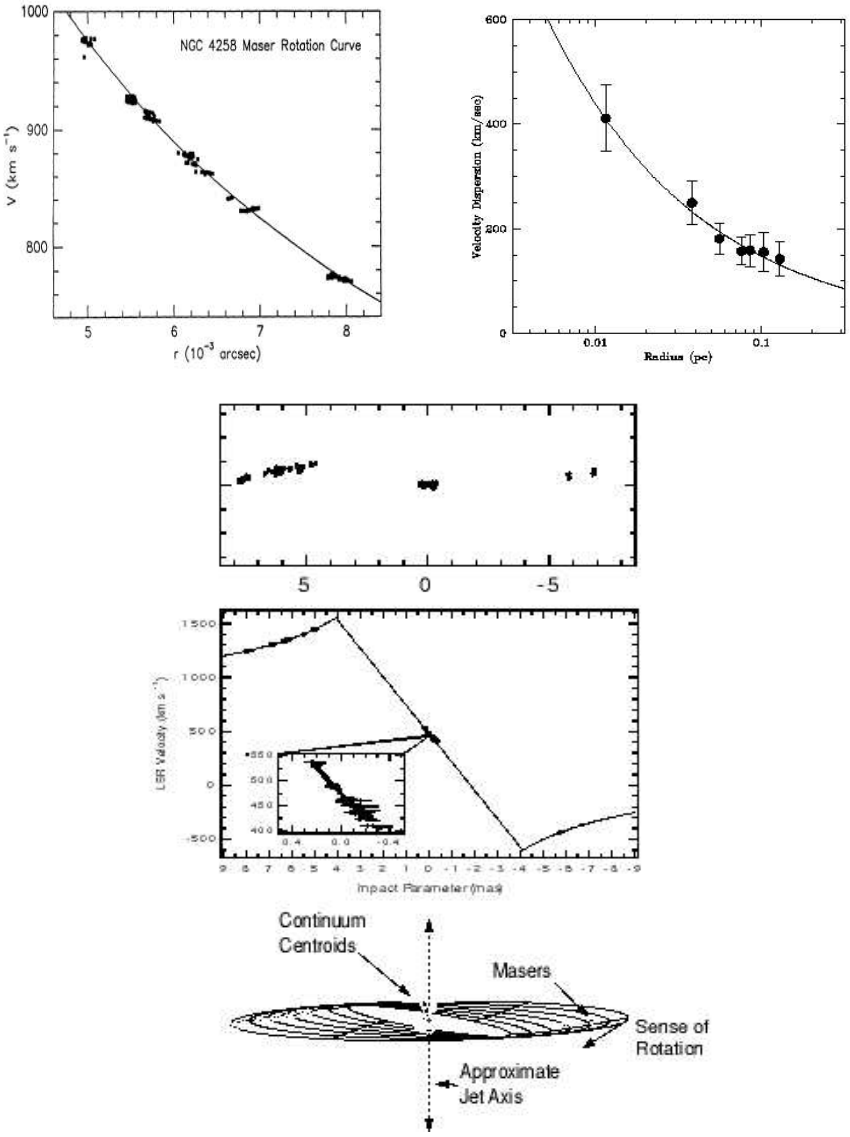

FIGURE 1.11. Upper–Left – Rotation curve for maser sources in NGC 4258 (Miyoshi et al. 1995). The line is the Keplerian $V(r)$.Rigth Projected stellar velocity dispersion as a function of projected distance from Sgr A* is consistent with Keplerian motion, which implies the gravitational field is dominated by mass within 0.1 pc. (Ghez et al. 2000).

Bottom – Overview of the NGC 4258 system.(a) VLBA map (scale marked in milliarcseconds) of the disk on 1995 January 8 including redshifted high-velocity features (left), systemic velocity features (center), and blueshifted high-velocity features (right). (b) Velocity vs. impact parameter for the masers with Keplerian rotation curve fit plotted (adapted from Miyoshi et al. 1995). (c) Schematic of warped disk with maser locations (points) overlaid (Herrnstein et al. 1996).

dynamical center of the Galaxy.
As a function of distance from Sgr A*, the velocity dispersion displays a fall–off well–fitted by Keplerian motion (Fig. 1.11) about a central dark mass of $2.6 \pm 0.2 \times 10^6$ $M_\odot$ confined to a volume of at most 10^{-6} pc^3.
Thus, independent of the presence of Sgr A*, the large inferred central density of at least 10^{12} $M_\odot$ pc^{-3}, which exceeds the volume-averaged mass densities found at the center of any other galaxy, leads to the conclusion that Galaxy harbors a massive central black hole (Ghez et al. 1998; Genzel et al. 2000).
Detailed X–ray images and spectra of the galactic center regions, up to 10 keV, were obtained to find direct evidence for high energy activities such as those observed in AGNs.
Observations resolved several faint discrete sources within $10'$ of the galactic centre; one of the ROSAT sources, RXJ 1745.6 − 2900 (Predehl and Truemper 1994), is within $10''$ coincident with Sgr A*; also they revealed a large amount of hot plasma which is strongly concentrated towards the galactic centre (Koyama et al. 1996; Yamauchi et al. 1990).
A large energy generation rate of 10^{41-42} erg/s is required to produce the observed plasma: the results indicate that the galactic centre has exhibited intermittent activities with an energy generation rate comparable to that of active nuclei, and that it had been luminous in X–rays until the recent past (Koyama et al. 1996).

Further evidence for the presence of black holes in AGNs comes from the detection of the asymmetric broad Fe fluorescence line features.
The Advanced Satellite for Cosmology and Astrophysics (ASCA) has provided data from over a dozen Seyfert 1 galaxies to reveal the presence of iron emission lines that are broadened by a considerable fraction of the speed of light, greater than 0.2 c in some cases (Mushotzky et al. 1995; Tanaka et al. 1995; Nandra et al. 1997).
The observed line profiles are the most direct evidence for the presence of supermassive ($\sim 10^8$ $M_\odot$) black holes in the centers of these galaxies: the spectra have distinctive skewed, double–peaked profiles that reflect the Doppler and gravitational shifts associated with emitting material in a strongly curved spacetime.
The data strongly support a model wherein the emission lines are produced by iron $K\alpha$ fluorescence at 6.4 keV when optically thick, "cold" regions of an accretion disk are externally illuminated by hard X-rays (cfr. sect.1.1).
In one bright, well–studied source, $MCG - 6 - 30 - 15$, the high signal–to–noise ratio has enabled parameters of a simple geometrically thin, relativistic model to be estimated (Fig. 1.12) (Tanaka et al. 1995; Pariev et al. 2001 and reference therein).

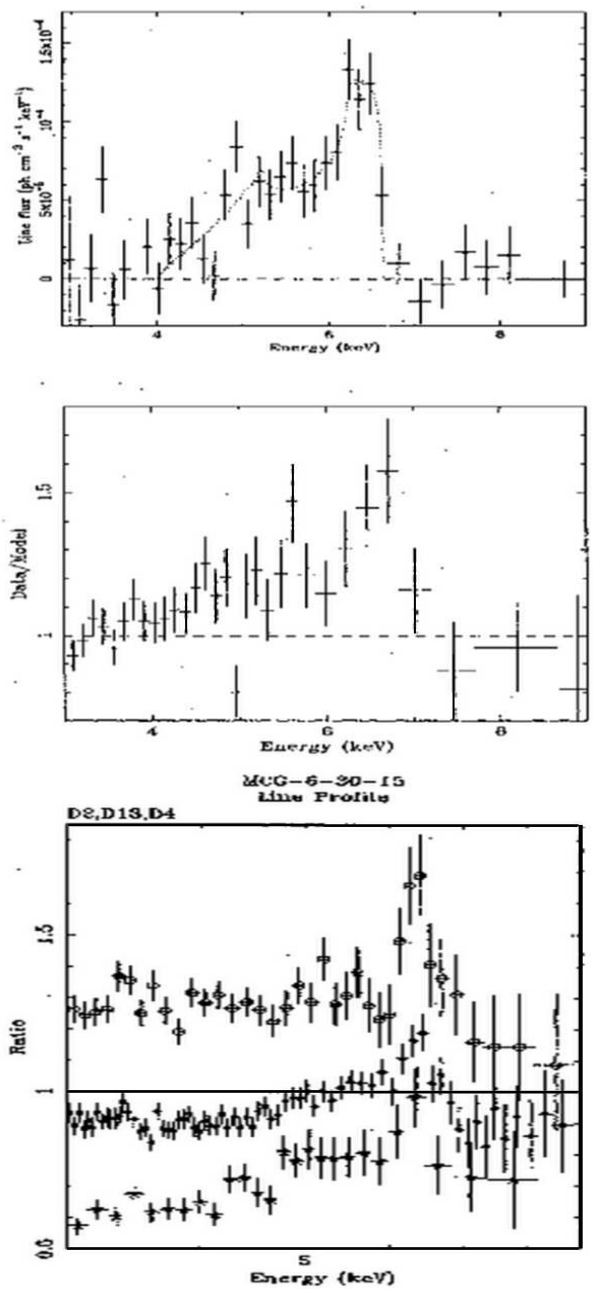

FIGURE 1.12. On the left: the broad lines in MGC-6-30-15 (top, Tanaka et al. 1995) and IRAS18325 (bottom, Iwasawa et al. 1996). The bottom figure shows the ratio of the data to a broken power-law continuum fit: an excess of counts, which can be modeled as a broad iron K-shell line, is observed between 4 and 7 keV, while a sharp drop is observed in the data at $\sim 7.5\ keV$. On the rigth: the variable broad line in $MGC-6-30-15$, shown in terms of the ratio of data to mean, best fitting continuum interpolated under the line. The upper points are from a bright phase, the middle ones from intermediate levels and the lower ones from a dim phase (Fabian 1996). Recent studies revealed that the spectrum of the broad iron line have to be seen as a composition of an approximately constant component, containing a strong iron emission line, and a variable power law component (Details in Fabian and Vaughan 2003).

Relativistically broadened iron lines from AGN provide a powerful tool to study properties of the accretion disk, in particular the orientation, extent and emissivity gradient radially outward from the central engine; furthermore they can help to explore and understand dynamical processes in the accretion of gas onto supermassive black holes: recent studies highlight that accretion events are responsible for changes in the line profile.
Accretion events and accretion disk dynamics, on the other hand, are thought to provide the "fuel" for the relativistic jets production in radio–loud AGNs. AGNs (Fig. 1.13; 1.14).
Several models have been proposed for the formation and stability of jets (Blandford and Begelman 1999; Livio et al. 2003) and a direct correlation between line variability and the ejection of new components into the jets, seen in radio, is expected. The detection of a relativistic, broad iron line in NGC1052, a strong radio source with a prominent compact jet-structure allowed, for the first time, to study the interrelation between the accretion process and jet dynamics on sub-parsec scales. Very Long Baseline Interferometry (VLBI) observations of NGC1052 probed regions as small as light days in the black hole vicinity and have been performed regularly at a wavelength of 2cm within the scope of the VLBA 2cm Survey since 1995. The most violent ejection of a new, bright jet component into the jet of NGC1052 during this monitoring campaign occured in 2000.
Kadler et al. 2005 report significant variability of the relativistic iron line between two X-ray observations (performed with the BeppoSax and the XMM-Newton telescopes) before and after this ejection event. Such an observational signature suggests that a part of the disk was fed into the black hole and a fraction of the material was ejected into the jet.

1.1.2 Unified Models

The axisymmetric model[d] of AGN depicted in Fig. 1.9 implies a radically different AGN appearence at different aspect angles Fig. 1.9 (Unification Model; Antonucci 1993).
Depending on the orientation of the torus with respect to the observer's line of sight, the central object is seen or hidden.
When it is hidden, we see only the Narrow Line Region and in the spectra we see only narrow emission lines; the AGN is a Type 2.

[d]The figure shows a model that, as regard many physical aspects, is an over-simplification of the real structure.

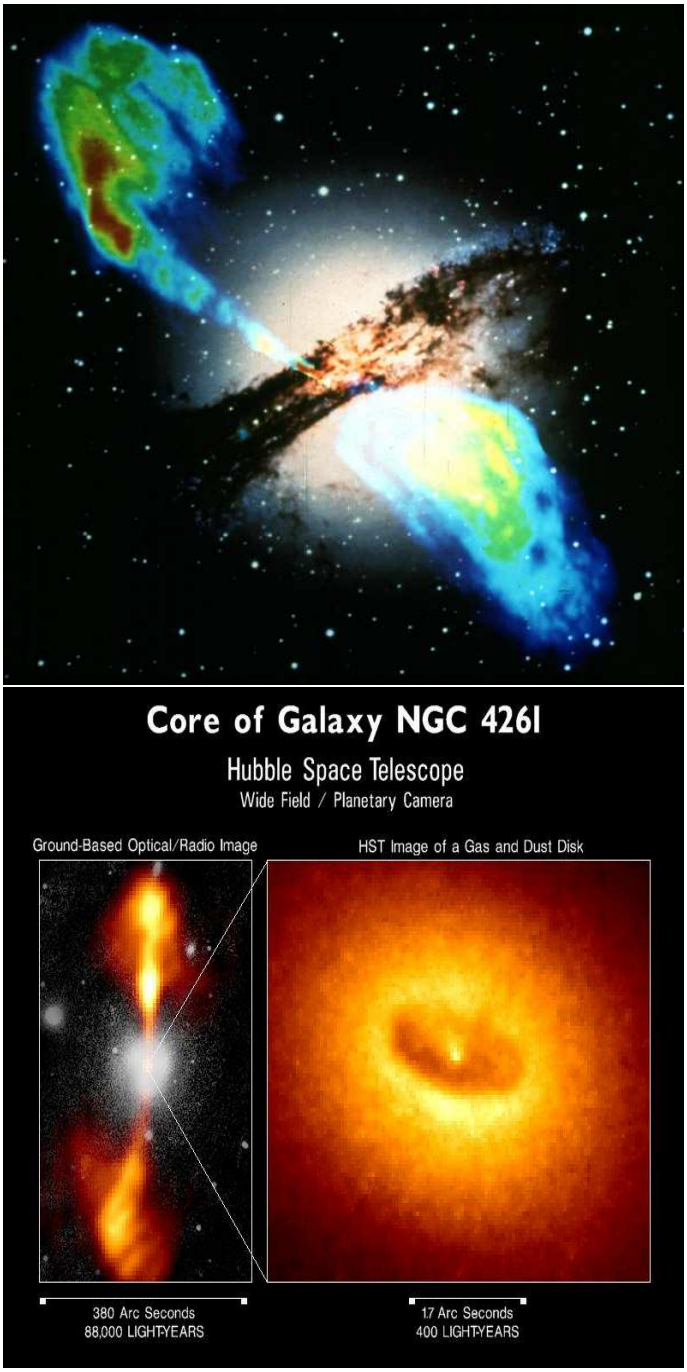

FIGURE 1.13. upper: VLA 6cm (Radio) 1988 VLA 6cm (Radio), VLA and Optical The Hubble wide–field camera visible image of the merged Centaurus A galaxy, also called NGC 5128.
bottom: The image on the left is a ground-based composite optical/radio view of NGC4261. In visible light (white), the galaxy appears as a fuzzy disk. A radio image (orange) shows a pair of opposed jets emanating from the nucleus and spanning a distance of 88,000 light–years. The NASA Hubble Space Telescope image (right) shows the giant disk of cold gas and dust fueling a possible black hole at the core of galaxy NGC4261. The dark, dusty disk feeds matter into the black hole, where gravity compresses and heats the material. Some hot gas squirts out from the black hole's near–vicinity to create the radio jets. The jets are aligned perpendicular to the disk, like an axle through a wheel. This provides strong circumstantial evidence for the existence of a black hole "central engine" in NGC4261.

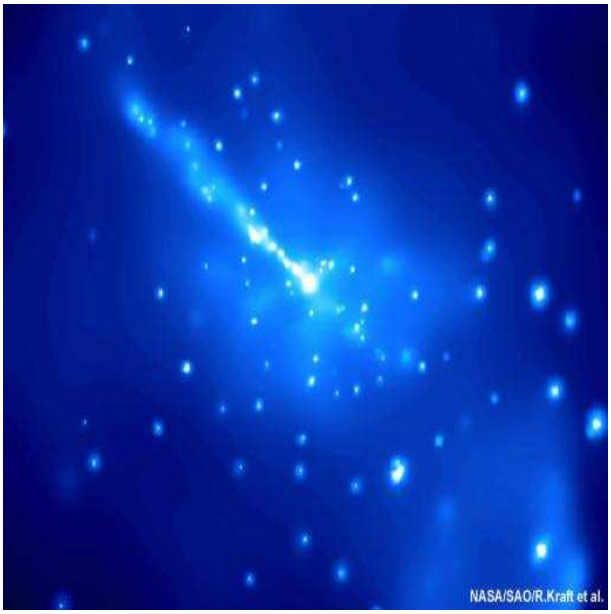

FIGURE 1.14. Chandra X-ray Observatory view of Centaurus A. The image provides a detailed X-ray view of a tremendous jet of energy emanating from the galaxy's center.

When it is seen, we see both Broad and Narrow Line Region and in the spectra we see both the components in the emission lines; the AGN is a Type 1.
In the presence of jets when the angle between the jet axis and the line of sight is small the object appears as a Blazar.

Optical spectropolarimetry measurements of scattered broad permitted lines provide strong evidence in favour of the unified model (Antonucci 1993).
Seyfert 2 galaxies have broad emission lines seen in polarized light (Tran 2001; Moran et al. 2000), therefore Seyfert 2 galaxies seem to host a hidden Seyfert 1 nucleus.
More evidence in favour of the unified model comes from the X–ray spectra: the column density of neutral hydrogen in type 2 Seyferts is significantly higher than in type 1 objects as would be expected if, for the type 2 sources, the nucleus is observed through the torus (Turner et al. 1997; Smith & Done 1996). Observed column densities range from $10^{22}\,cm^{-2}$ to higher than $10^{24}\,cm^{-2}$ (Risaliti et al. 1999; Bassani et al. 1999).

However, not all Seyfert 2 galaxies show a Broad Line Region in polarized light and not all Seyfert 2 galaxies have column densities higher than $10^{22}\,cm^{-2}$ (Panessa and Bassani 2002).

Polarimetric surveys of complete samples of Seyfert 2s indicate that a large fraction of these objects (up to 50%) do not show a hidden BLR typical of an obscured Seyfert 1 nucleus. Furthermore there have been some recent examples of Seyfert 2 galaxies, such as NGC 3147 (Ptak et al. 1996), NGC 4698 (Pappa et al. 2001) and NGC 7590 (Bassani et al. 1999), which have no or low absorption measured from the X-ray spectrum.
The exact nature of these peculiar Seyfert 2s is still unclear, as it is not obvious what obscures their Broad Line Region: they may be intrinsically different objects than those explained by the unified theory or in other words they may be the "true" Seyfert 2 galaxies which are sometimes discussed in the literature (Tran 2001 and reference therein).
There appears to be two types of Seyfert 2 galaxies, one containing an energetic AGN with a BLR and the other possessing a less energetic AGN with a weak or absent BLR, whose energy output may be dominated by other nuclear and circumnuclear processes such as starbursts: the latter is the "pure" Seyfert 2 galaxy model. Also a dust-to-gas ratio or a dust composition strongly different from the Galactic one could be a possible solution to the problem, i.e. a strong dust contribution obscures the BLR and it is not detectable in X–rays (Maiolino et al. 2001).

On the other hand, examples of Xray absorbed, optical broad line AGNs (both Seyfert and QSOs) have been discovered at relatively low redshifts among AGN selected from nearinfrared surveys (2MASS AGN survey, Wilkes et al. 2002) and at brighter Xray fluxes in the ASCA and BeppoSAX surveys (Akiyama et al. 2000; Fiore et al. 2001a,b; Brusa et al. 2003; Perola et al. 2004).

Multiwavelength analysis then highlight that there are cases where the optical spectroscopic classification turns out the opposite of the X–ray classification. These results emphasize that classifications may not apply beyond the wave band in which they were made and the necessity for substantial revision of the AGN unification models.

1.2 AGN - Galaxy connection : SMBHs masses vs. host galaxy properties

Spectroscopic and photometric studies of the stellar and gas dynamics in the very central regions of local spheroidal galaxies and prominent bulges established that

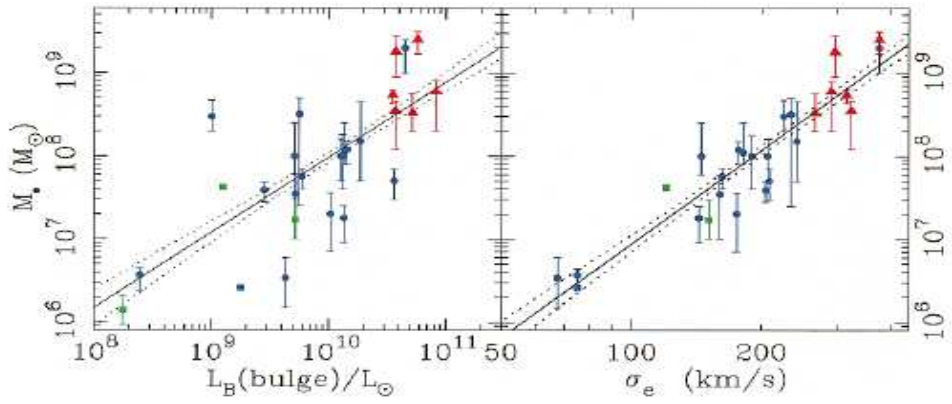

FIGURE 1.15. Black hole mass versus bulge luminosity (left) and the luminosity–weighted aperture dispersion within the effective radius (right). There are 26 points in the dispersion plot; 13 are detections from stellar kinematics (K. Gebhardt et al. 2000; G. Bower et al. 2000). Green squares denote galaxies with maser detections, red triangles are from gas kinematics, and blue circles are from stellar kinematics. Solid and dotted lines are the best–fit correlations and their 68% confidence bands. Gebhardt et al. 2000.

in most, if not all, galaxies observed with high enough sensitivity a central SMBH ($10^6 \div 3 \times 10^9\ M_\odot$) is present with a well–defined relationship between the black hole mass and the properties of its host.
Indeed the following relationship exist: the tight correlation between the BH mass and the velocity dispersion of stars in the host galaxy (Magorrian et al. 1998; Ferrarese and Merritt 2000; Gebhardt et al. 2000; Tremaine et al. 2002), the bulge luminosity (Gebhardt et al. 2000; Ferrarese and Merritt 2000; Ferrarese 2002), the mass of the spheroidal component (McLure and Dunlop 2002; Dunlop et al. 2003; Marconi and Hunt 2003), and the mass of the dark halo (Ferrarese 2002).

Gebhardt et al. 2000 describe a correlation between the mass M_{bh} of a galaxy's central black hole and the luminosity–weighted line–of–sight velocity dispersion σ within the half–light radius. The best–fit correlation is $M_{bh} = 1.2(\pm 0.2) \times 10^8 M_\odot (\sigma/200\, km\, s^{-1})^{3.75(\pm 0.3)}$ over almost 3 orders of magnitude in M_{bh}; the scatter in M_{bh} at fixed σ is only 0.30 dex (Fig. 1.15).
Ferrarese 2002 finds an analogous correlation though with a steeper slope, $\alpha = 4.8 \pm 0.5$.
The $M_{bh} - \sigma$ relation is of interest not only for its strong predictive power but also because it implies that central black hole mass is constrained by and closely related

to properties of the host galaxy's bulge.
The tight correlation between black hole mass and velocity dispersion strongly suggests a causal connection between the formation and evolution of the black hole and the bulge.
However, the nature of this connection remains obscure (Haehnelt & Rees 1993; Haiman & Loeb 1998; Silk & Rees 1998; Kauffman & Haehnelt 2000).
It is natural to assume that bulges, black holes, and quasars formed, grew, or turned on as parts of the same process, in part because the collapse or merger of bulges might provide a rich fuel supply to a centrally located black hole.

The correlation of the mass of the central black hole with the spheroid velocity dispersion σ links phenomena at widely different scales (from the parsecs of the BH sphere of influence to the kiloparsecs of the bulge).
This demonstrates that galaxy formation and active galactic nuclei (AGN) activity are tightly connected.

It is not yet understood if this relations were set in primordial structures, and consequently how they are maintained throughout cosmic time with such a small dispersion, or indeed which physical processes established such correlations in the first place; i.e. suggestions for the $M_{BH} - \sigma$ dependence have appealed to strong feedback due to quasar outflows on the protogalactic gas reservoir (e.g., Silk & Rees 1998), to cap- ture of stars following protogalactic collapse (Adams, Graff, & Richstone 2001), and to star formationregulated black hole growth (Burkert & Silk 2001).
Recently Shields et al. 2003 have found that the correlation between MBH and the stellar velocity dispersion is already present at redshift up to $z = 3$.

Further indications highlighting the galaxy–AGN connection come from the correspondence between the luminosity function of active star-forming galaxies at $z \sim 3$, the B-band luminosity function of quasars and the mass function of dark halos at the same redshift (Haehnelt et al. 1998, Monaco et al. 2000); the similarity between the evolutionary histories of the luminosity densities of galaxies and quasars (e.g. Cavaliere and Vittorini 2000; Franceschini et al. 1999).

In addition, studies of active galactic nuclei (AGN) hosts in the local universe with the Sloan Digital Sky Survey (SDSS) have also shown that AGN activity is closely related to star formation in local galaxies: the AGN itself could regulate the amount of the star formation that occurs at the center of galaxies.
Quite apart from any specific scenario, principal results from this studies have an

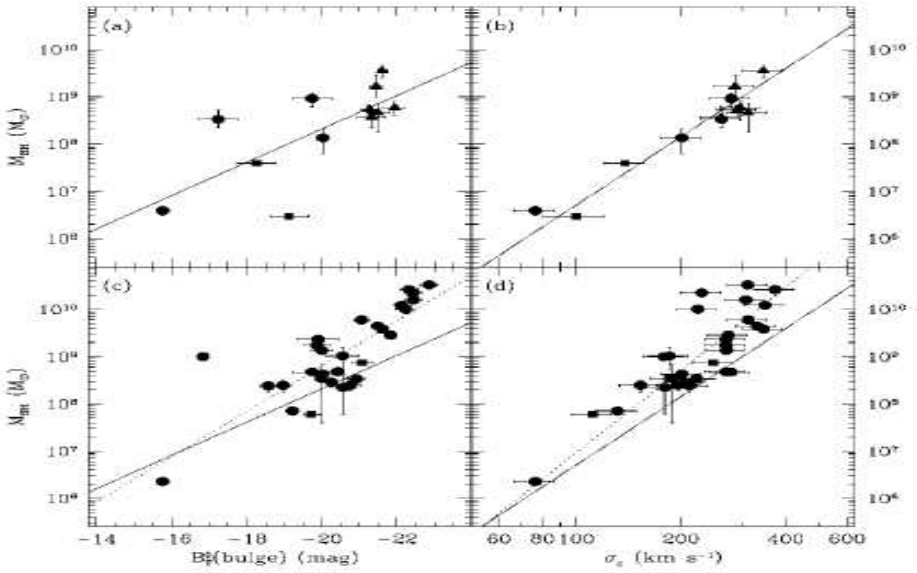

FIGURE 1.16. (a) BH mass vs. absolute blue luminosity of the host elliptical galaxy or bulge for the galaxies that the authors deem to have reliable BH mass estimates. The solid line is the best linear fit. Circles and triangles represent mass measurements from stellar and dust/gas disk kinematics, respectively. The squares are the Milky Way (Mbh determined from stellar proper motions) and NGC 4258 (Mbh based on water maser kinematics), the only two spiral galaxies in the sample. (b) Again BH mass vs. the central velocity dispersion of the host elliptical galaxy or bulge, corrected for the effect of varying aperture size. Symbols are as in (a). (c) Same (a), but for the sample of galaxies with less secure BH mass detections. Circles are elliptical galaxies; squares are spiral galaxies. The solid line is the same least– squares fit shown in (a); the dashed line is the fit to sample B. All BH mass estimates in this sample are based on stellar kinematics. (d) Same as (b), but for sample B. Symbols are as in (c). Ferrarese & Merritt 2002.

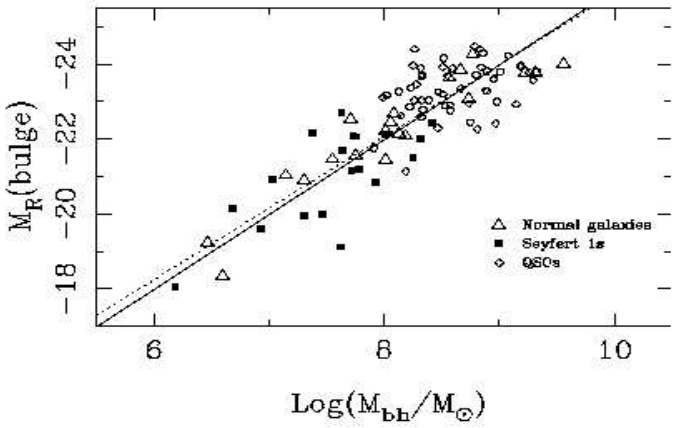

FIGURE 1.17. Absolute R–band bulge magnitude versus black hole mass for the full 90–object sample. The black hole masses for the 72 AGNs are derived from their $H\beta$ line widths under the disc–like BLR model. The black hole masses of the inactive galaxies (triangles) are dynamical estimates as compiled by Kormendy & Gebhardt 2002. Also shown is the formal best fit (solid line) and the best–fitting linear relation (dotted line). Mclure & Dunlop 2002.

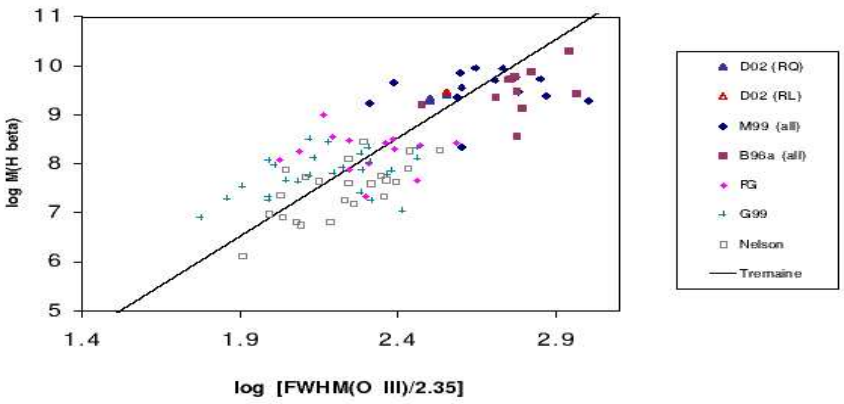

FIGURE 1.18. Black hole mass derived from $H\beta$ line width and continuum luminosity versus width of the [O III] line for radio quiet AGN. Line is the $M_{BH} - \sigma$ relation from Tremaine et al. 2002; it is not a fit to the QSO data. Shields et al. 2003 and reference therein.

appealingly simple interpretation.
The two necessary ingredients for a powerful AGN are massive BH and an abundant fuel supply. Only massive early–type galaxies contain massive BHs, and only galaxies with significant amounts of recent/on-going star formation have the requisite fuel supply. This combination is rare today, but evidentely was not so at high redshift (Kauffmann et al. 2003; Heckman et al. 2004).
All these observational evidences suggest that the process that leads to the formation of galactic spheroids must be intimately linked to the growth of the central SMBH.

1.3 Joint evolution: spheroids - disks - agns

Although the traditional approach to galaxy formation and evolution regards nuclear activity as an incidental diversion, it is becoming clear, beyond any reasonable doubt, that the formation of super-massive black holes powering nuclear activity is intimately linked to the formation of its host galaxy and plays a key role in shaping its evolution.
However, there is not, as yet, a clear understanding of the physical mechanisms governing the interactions among the active nucleus and the host galaxy.
From a theoretical perspective, several groups have attempted to investigate the link between the cosmological evolution of AGNs and formation history of galaxies within the context of semi-analytic and numerical models of galaxy formation and evolution.
The basic ingredients of some of these models are:

- major mergers: supermassive black holes are formed and fuelled during major mergers. If two galaxies of comparable mass merge, their central black holes coalesce and a few per cent of the gas in the merger remnant is accreted by the new black hole. (Kauffmann & Haehnelt 2000)

- characteristic of dark matter haloes, such as their spin, and major mergers: since the BH vs. host characteristic seem to suggest that AGNs prefer early-type morphologies, is assumed that the same physical variable that determines galaxy morphology is able to modulate the mass of the black hole responsible for activity.
  Both halo spin and the occurrence of a major merger are considered as candidates for this role. (Monaco et al. 2000).

- self-regulated growth of SMBHs: the growth of a supermassive BH is expected to be accelerated during a galaxy merger, when cold gas is driven to the center

of the merger remnant.
It is natural to expect that a quasar shining at its limiting Eddington luminosity could generate a powerful galactic wind and eventually terminate the accretion process that feeds it.
Indeed, Silk and Rees 1998 pointed out that winds from quasars could generate self-regulating outflows in the surrounding gas if the energy in the outflow liberates as much as the binding energy of the gas in a dynamical time. (Wyithe and Loeb 2003).

- joint evolution of star formation and BH growth: the black hole growth and activity at the centers of galaxies are primarily regulated by the evolution of the total baryonic gas mass content of galaxies.
  The total amount of gas in galaxies may saturate simply in response to star formation and, in particular, to supernova feedback and galactic winds. In the same way, black hole growth saturates because of the competition with star formation and feedback. Di Matteo et al. 2003 in their work did not assume that activity is triggered by galaxy mergers but simply that it is possible in all galaxies that are star-forming.

- gravity and supernova feedback: within dark matter halos, forming at the rate predicted by the canonical hierarchical clustering scenario, the gas evolution is controlled by gravity, radiative cooling, and heating by feedback from supernovae and from the growing active nucleus.
  The diffuse gas within the DM halo fall down into the star-forming regions at a rate ruled by the dynamic and cooling times. Part of this gas condenses into stars, at a rate again controlled by the local dynamic and cooling times. However, the gas also feels the feedback from supernovae and from active nuclei, heating it and possibly expelling it from the potential well. In addition, the radiation drag on the cold gas decreases its angular momentum, causing an inflow into a reservoir around the central BH. Viscous drag then causes the gas to flow from the reservoir into the BH, increasing its mass and powering the nuclear activity.
  In turn, the kinetic energy carried by outflows driven by active nuclei can inject in the ISM a sufficient amount of energy to unbind it, thus halting both the star formation and the BH growth. (Granato et al. 2004)

Some of these models have been applied only to the bright AGN population or fail to account for some of the observed relationships between the black hole and the host properties or to describe the statistical distribution of AGNs properties, suc as

their luminosity functions.
Furthermore, such models generally follow the AGNs evolution at high-intermediate z but do not match the observed steep decline of the their density at redshifts of $z \leq 1$, a range of cosmic time of key interest for the activity of AGNs observed in X-rays.
Recently Menci et al. 2004 have incorporated the description of the X-ray properties of active galactic nuclei (AGNs) into a semianalytic model of galaxy formation in the context of hierarchical scenarios.
The accretion is triggered by galaxy encounters, not necessarily leading to bound merging, in common host structures such as clusters and especially groups; these events destabilize part of the galactic cold gas and hence feed the central BH, following the physical modeling developed by Cavaliere & Vittorini 2000.
As a result, at high z the protogalaxies grow rapidly by hierarchical merging; meanwhile, much fresh gas is imported and also destabilized, so the BHs are fueled at their full Eddington rates. At lower z, the dominant dynamical events are galaxy encounters in hierarchically growing groups; now refueling peters out, as the residual gas is exhausted while the destabilizing encounters dwindle. With no parameter tuning other than that needed for star formation in canonical SAMs, the model naturally produces in the bright QSO population a rise for $z > 3$, and for $z \leq 2.5$ a drop as steep as observed.
In addition, the results closely reproduce the observed luminosity functions of the optically selected QSOs, their space density at different magnitudes from $z \sim 5$ to $z \sim 0$, and the local $m_{BH} - \sigma$ relation.

Some other groups made phenomenological investigations, specifically comparing the redshift evolution of the star-formation rate in galaxies with the evolution of AGN emissivity per comoving volume (i.e., Franceschini et al. 1999), or the evolution of the black hole mass density, ρ_{BH}, to that of the observed mass density of stars in galaxies, $\rho_\star$ (i.e., Merloni et al. 2004).

Franceschini et al. 1999 found a close match between the evolution rates of the star-formation in galaxies and of the volume emissivity in AGNs. This similarity seems to hold not only for high luminosity AGNs ($L_x > 10^{44.25}\ erg/s$) compared with the SF in massive spheroidal galaxies, but also when comparing the average properties of the global populations, including low mass/luminosity systems.
On the other hand Merloni et al. 2004 have shown that BH accretion does not exactly track either the spheroid nor the total star assembly.

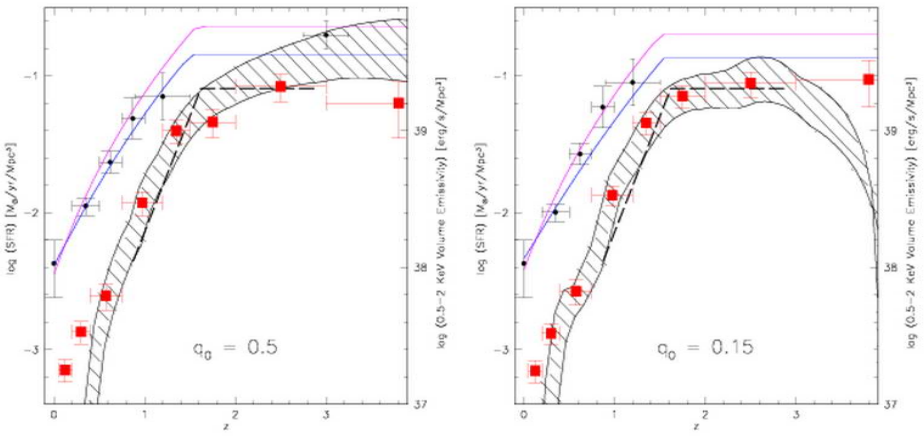

FIGURE 1.19. On the left: comparison of the redshift evolution of AGN emissivity per comoving volume (to be read on the right-hand axis) with the evolution of the star-formation rate in galaxies (left-hand axis), for q0 = 0.5. Small filled circles are the evolutionary SFR of field galaxies estimated from conversion of the rest-frame optical-UV flux to SFR. The shaded region describes the evolution of the SFR in field galaxies morphologically classified as ellipticals and S0s by Franceschini et al. 1998. The filled squares are the 0.5 to 2 keV comoving volume emissivities (in $erg/s/Mpc^3$) of high-luminosity AGNs ($L_{0.5-2keV} > 10^{44.25}\ erg/s$). The top two lines are the 0.5-2 keV volume emissivities of the total AGN population (normalized by the same factor), based on the LDDE1 and LDDE2 models producing 60% and 90% of the XBR at 1 keV, respectively. The thick dashed line is the volume emissivity of optical quasars from Schmidt, Schneider & Gunn (1995). The scales of the two vertical axes are chosen in such a way that AGN volume emissivity and SFR density overplot each other. On the right: same as left, for $q0 = 0.15$ (SFR densities to be red on the left y-axis, AGN volume emissivities on the right y-axis). Small filled circles at $z \leq 1.2$ are the galaxy SFR transformed from $q_0 = 0.5$ to $q_0 = 0.15$ by correcting luminosities and volumes within each redshift interval (correction factors being 1, 0.9, 1.15, 1.21 and 1.27 for data bins ranging from $z = 0$ to $z = 1.2$).

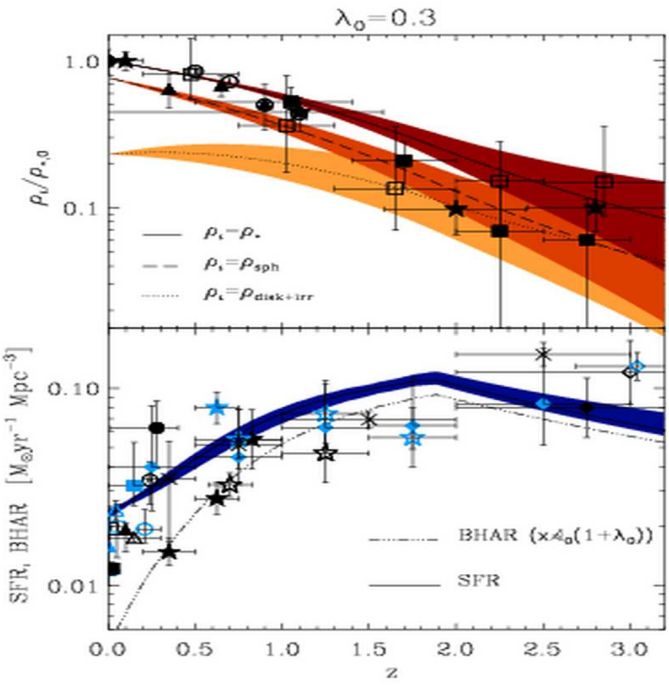

FIGURE 1.20. The top panel shows the evolution in the best fit stellar mass density (solid line) as a function of redshift, where the density is given as a ratio to the local value, $\rho_{\star,0} = 5.610^8\ M_\odot Mpc^{-3}$ (Cole et al. 2001). A value of $\lambda_0 = 0.3$ and $\rho_{BH,0} = 4.2 \times 10_5\ M_\odot Mpc^{-3}$ (Marconi et al. 2004) are adopted here. The darker shaded area represents the 1-sigma confidence interval for . Also shown are the relative decomposition of the total stellar mass density into sph (dashed line, grey shaded area) and disk+irr (dotted line, light grey shaded area), with their corresponding 1-sigma confidence interval. Please note that the absolute normalization - and to a lesser degree the shape - of these two curves depends on the specific value of 0 adopted (see text for details). The data points correspond to measurements from the 2dFGRS+2MASS (Cole et al. 2001 filled circle), the Canada France Redshift Survey (Brinchmann & Ellis 2000 filled triangles), the MUNICS survey (Drory et al. 2004 open circles), the Hubble Deep Field North (HDF-N; Dickinson et al. 2003 filled squares), and the HDF-S (Fontana et al. 2003 open squares; Rudnick et al. 2003 filled stars). The lower panel shows the evolution in the best fit SFR (solid line and dark red shaded area) and the corresponding black hole accretion rate density (rescaled by a factor A0(1 + 0)). The data points correspond to the measurements from Haarsma et al. (2000) filled black circles; Condon et al. 2002 filled grey circles; Pascual et al. 2001 open black circles; Tresse and Maddox (1998) open grey circles; Gallego et al. (1995), updated following Glazebrook (1999) filled black squares; Sullivan et al. (2000) filled grey squares; Serjeant et al. (2002) open black squares; Glazebrook et al. (2003) open grey squares; Brinchmann et al. (2004) filled black triangles; Gallego et al. (1995) filled grey triangles; Treyer et al. (1998) open black triangles; Gronwall (1998) open grey triangles; Lilly et al. (1996) filled black stars; Flores et al. (1999) filled grey stars; Cowie et al. (1996) open black stars; Connolly et al. (1997) open grey stars; Madau, Pozzetti and Dickinson (1998) filled black diamonds; Pascarelle, Lanzetta & Fernandez-Soto (1998) filled grey diamonds; Hughues et al. (1998) open black diamonds; Steidel et al. (1999) open grey diamonds; Sawicki et al. (1997) black crosses.

This is the most important result of their study: irrespective of the exact mass budget in spheroids and disks+irregulars, the ratio of the total or spheroid stellar to black hole mass density was lower at higher redshift. Their results indicate that the black hole growth rate is suppressed with respect to the total SFR at $z < 2$, as it can be seen in Fig. 1.20 (as also shown in the cosmological simulations of Di Matteo et al. 2003). Merloni et al. conclusions have a direct observable consequences for the expected redshift evolution of the $M_{BH} - M_{sph}$ relationship: they predict a larger black hole mass for a given host spheroid mass at higher redshift.
Consequently, it is clear that studying the evolution of accretion along with morphologies and structural parameters of the host galaxies with cosmic time will provide crucial informations and will help us to better understand how the simultaneous evolution of black holes, spheroids, and disks in galaxies proceeded.

1.4 Tracing the accretion history in the Universe

Quasars and AGNs have been studied in all accessible wavebands, in all of them showing evidence for strong cosmological evolution.
The most efficient AGN selection comes from X-ray surveys: a purely flux-limited sample at X-ray energies, in particular hard X-ray enegies less affected than other bands by obscuration, contains a vast majority of AGNs with no particular bias as a function of redshift.
The same is not true for optical searches, suffering incompleteness at both low-luminosities (because of the contribution of the host galaxy reddening the colours) and at the high redshifts (because of the effect of dust and intergalactic opacity), and for surveys of radio sources, since only a minority of AGNs emit in the radio.
The Chandra (Weisskopf et al. 2002) and XMM-Newton (Jansen et al. 2001) X-ray Observatories have revolutionized AGNs studies revealing that previous optically-selected and soft X-ray-selected samples substantially undercount the AGN population, at least at low and intermediate X-ray luminosities ($L_{2-8keV} < 10^{44}\ erg\, s^{-1}$; Cowie et al. 2003; Hasinger 2003; Fiore et al. 2003; Ueda et al. 2003). Moreover, many X-ray sources show no signs of AGN activity at all in their optical spectra (Barger et al. 2001; Tozzi et al. 2001; Hornschemeier et al. 2001).
A further crucial advantage of the X-ray selection is provided by the XRB, which sets an integral constraint on AGN emissivity at fluxes much fainter than observable with the present facilities.

- The cosmic X–Ray Background

  The cosmic Xray background (XRB) was discovered at the dawn of the Xray

astronomy: during the first successful rocket flight launched to study the Xray emission from the Moon, the presence of a residual diffuse emission was also "serendipitously" revealed (Giacconi et al. 1962). The lack of any correlation with the galactic latitude, and a dipole anisotropy consistent with that of the dipole component of the Cosmic Microwave Background (CMB; Shafer and Fabian 1983) strongly argued from the beginning in favour of a cosmological origin of this extragalactic background radiation.

The first broadband measurements of the XRB spectrum was obtained at the end of the 70's with the HEAO1 satellite. Marshall et al. 1980 showed that the HEAO-1 data were very well fitted by a 40 keV thin thermal bremsstrahlung model, approximated below 15 keV with a simple powerlaw spectral function ($F(E) \propto E^{\Gamma}$) with photon index $\Gamma \sim 1.4$. It was therefore quite natural to hypothesize the presence of a truly diffuse hot Inter Galactic Medium (IGM) with a characteristic temperature of $kT = 40(1+z)$ keV, as originally proposed by Field and Perrenod 1977. However, a reasonable extrapolation of the X-ray properties and optical counts of extragalactic sources led to the conclusion that discrete sources could contribute significantly to the XRB (Schmidt and Green 1986). Moreover, Giacconi and Zamorani 1987 have subsequently shown that, once the contribution estimated from known AGN is removed, the residual background spectrum is too flat to be interpreted in terms of an optically thin bremsstrahlung from a diffuse IGM. This hypothesis has been then entirely discarded with the results from the COBE satellite (Mather et al. 1990). A diffuse, hot ($T \geq 10^8$ K) IGM should give rise to evident high–frequency distortions in the CMB spectrum through inverse–Compton scattering, which have not been observed by COBE; this implies that the contribution of hot gas to the XRB is lower than 0.01% (Wright et al. 1994).

As a consequence, the only viable alternative for the XRB origin remained the superposition of discrete sources, and the most likely candidates appeared immediately to be AGN. The most serious problem with the discrete source origin for the XRB remained the so–called "spectral paradox" (Boldt and Leiter 1987): at that time there were already stringent evidences that the AGN X-ray continuum in the 2-10 keV band is well described by a power-law with index $\Gamma \approx 1.7 - 1.9$ (Mushotzky et al. 1984; Turner & Pounds 1989), too soft to fit the value observed for the hard XRB in the same energy band ($\Gamma \sim 1.4$). Setti & Woltjer 1989 showed that, on the basis of Unification Schemes of AGN,

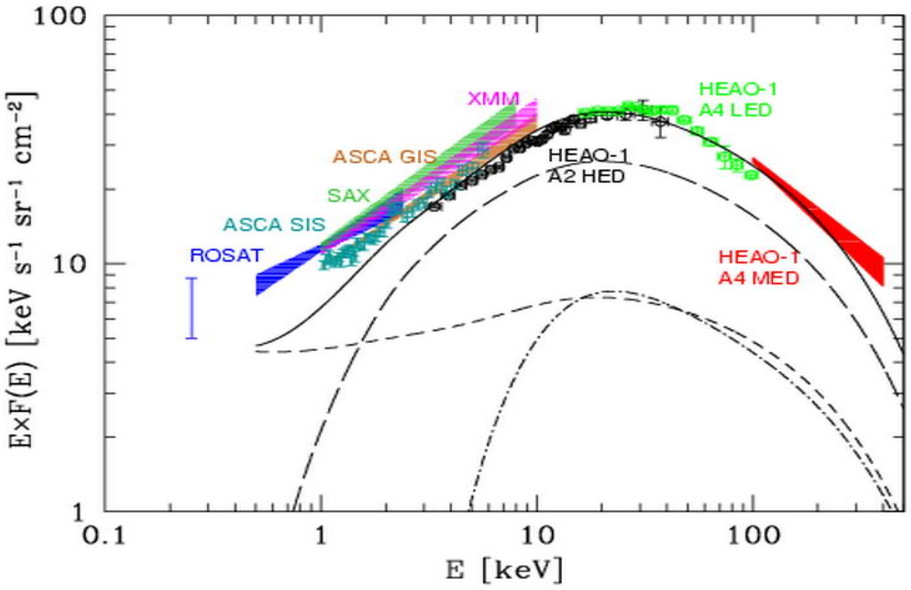

FIGURE 1.21. The AGN contribution (solid line) to the XRB spectral energy density as measured by different instruments (labeled). The contribution of unobscured ($N_H < 10^{21}\ cm^{-2}$, dashed line), Compton thin ($N_H = 10^{21} - -10^{24}\ cm^{-2}$, long–dashed line) and Compton thick ($N_H > 10^{24}\ cm^{-2}$, dot–dashed line) AGN is also shown. (Comastri et al. 2004).

strong X-ray absorption is naturally predicted for the sources optically classified as narrow line, Type 2 objects, and that the amount of obscuring matter along the line of sight, measured in equivalent neutral hydrogen column (N_H), can be even in excess than $10^{24}\ cm^{-2}$. As a consequence, the resulting X-ray spectra will peak at high energies (from a few keV up to $> 10\ keV$, depending from the N_H) and the net result is a flatter power-law spectral index. The "spectral paradox" could be therefore theoretically solved by assuming that the XRB is due to the superposition of absorbed and unabsorbed objects, with the same intrinsic steep ($\Gamma \sim 1.8$) power-law continuum. Following these indications, several authors have refined and developed populationsynthesis models able to reproduce the XRB spectral shape and intensity (e.g. Madau, Ghisellini & Fabian 1994; Comastri et al. 1995, 2001; Gilli, Salvati & Hasinger 2001), assuming a wide range of redshifts (i.e. evolution) and column densities of the absorbing matter in the range In Fig. 1.21 a compilation of XRB measurements in different energy bands is shown along with the best-fit model from Comastri et al. 2001. The contribution of unobscured (dashed line), mildly obscured ($N_H = 10^{21} - 10^{24} cm^{-2}$, Compton Thin) and heavily

obscured ($N_H > 10^{24}\ cm^{-2}$, Compton Thick) sources is also reported.
The combined fit of other observational constraints in addition to the XRB spectral shape (in primis the number counts, and the redshift and absorption distributions in different energy ranges) is needed to build a self-consistent model and discriminate among the assumptions adopted for the cosmological evolution of the discrete sources. In particular, the key parameter turned out to be the evolution of obscured (Type 2) sources. As an example, the baseline AGN synthesis model adopt a simple Pure Luminosity Evolution (PLE) and is based on the zero-th order AGN Unification Schemes (Antonucci 1993); this implies that 1) the evolution of obscured AGN is assumed to follow that of unobscured AGN, and 2) the existence of a population of high-luminosity, highly obscured quasars (the so-called QSO2) is naturally postulated (Comastri et al. 1995). Indeed, it has been subsequently shown that QSO2 are necessary in reproducing the 2-10 keV source counts at relatively bright fluxes ($\sim 10^{-13}$ $erg\,cm^{-2}\,s^{-1}$; Gilli et al. 2001; Comastri et al. 2001); however, despite intensive optical searches, these narrow-line high-redshift objects appear to be elusive, suggesting a space density and evolution different from that expected from unified schemes and calling for substantial revisions of the main assumptions of XRB baseline models.

Thanks to the ultra-deep X-ray surveys carried out in the Chandra Deep Field North (1Msec, CDFN, Brandt et al. 2001a, Alexander et al. 2003), Chandra Deep Field South (CDFS, Giacconi et al. 2001) and the Lockman Hole (Hasinger et al. 2001) the X-ray sky is now probed down to a $2-10keV$ flux limit of about $2 \times 10^{-16} erg\,cm^{-2}\,s^{-1}$ and a fraction as large as $80-90\%$ of the diffuse XRB is resolved into discrete sources (Mushotzky et al. 2000; Hasinger et al. 2001; Rosati et al. 2002; Alexander et al. 2003).
All the same, the ultra-deep Chandra and XMM-Newton surveys of the Chandra Deep Field North, Chandra Deep Field South and Lockman Hole cover each about $0.05-0.1$ square degrees and, as the slope of the AGN luminosity function at high luminosities is very steep, the number of high luminosity sources in these surveys is small. As an example, in the CDFN there are only 6 AGN with $logL_{2-10keV} > 10^{44}$ at $z > 3$ and 20 at $z > 2$ (Cowie et al. 2003).

To accurately trace the accretion history in the Universe, to compute luminosity functions on wide luminosity and redshift intervals, and to find sizeable samples of "rare" objects, such as high luminosity, highly obscured type 2 QSO (and also of

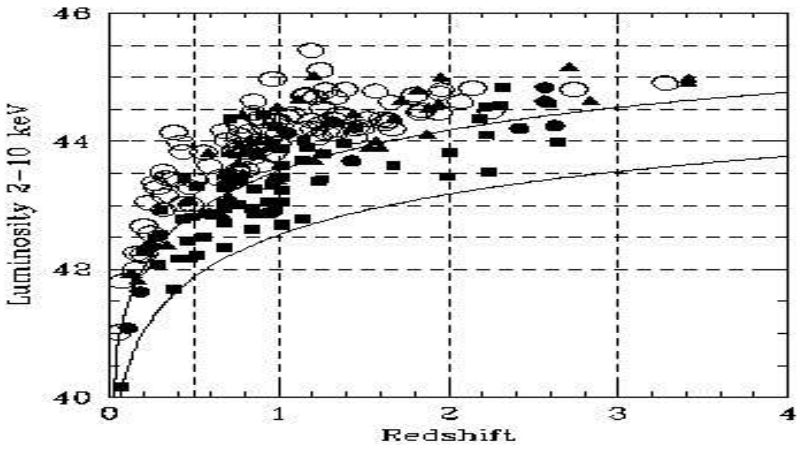

FIGURE 1.22. The 210 keV luminosity as a function of the redshift for different hard X–ray samples.
HELLAS2XMM = open circles; CDFN = filled squares; LH = filled triangles; SSA13 = filled circles.
The lower and upper solid lines represent the flux limits of $10^{-15}\ erg\,cm^{-2}\,s^{-1}$ (i.e. Chandra deep surveys) and $10^{-15}\ erg\,cm^{-2}\,s^{-1}$ (HELLAS2XMM survey) respectively.

other rare sources like the X-ray bright, optically normal galaxies, XBONGs, Fiore et al. 2000, Comastri et al. 2002) a much wider area needs to be covered, of the order of a few square degrees.
Shallower, but larger area surveys are fundamental to complement the deeper pencil-beam surveys in obtaining a more complete coverage of the L – z plane, to find QSOs with luminosity close to L_*, the break in the AGN luminosity function, in a large z range and to obtain reliable spectroscopic redshifts of the source population with high X-ray-to-optical (X/O[e]) flux ratio.
Indeed, one of the most interesting results of deep and shallow hard X-ray surveys has been the discovery of a population of sources with X/O much higher, 10 times or more, than that of typical broad line AGN ($X/O \sim 1$). Almost by definition these high X/O objects are amongst the faintest optical sources and, at the 10-100 times fainter fluxes reached by the CDFN, CDFS and LH surveys, most sources with high X/O have optical counterparts too faint for even 8 10 m class telescopes.

In summary:

[e]The X–ray (2-10 keV) to optical (R band) flux ratio. The R band flux is computed by converting R magnitudes in specific fluxes and then multiplying by the width of the R filter.
We used $f_R(0) = 1.74 \times 10^9\ erg\,cm^{-2}\,s^{-1}\,\dot{A}^{-1}$ and $\Delta\lambda_R = 2200\ \dot{A}$. Zombeck 1990.

- Hard X–ray survey are the most efficient way to discriminate accretion-powered sources, such as AGN, from starlight and optically thin hot plasma emission. Hard X–ray surveys are the most direct probe of super-massive black hole accretion activity, which is recorded in the cosmic X-ray background (CXB) spectral intensity.

- Hard X–rays are less affected than other bands by obscuration. This is a key feature because it allow to trace accretion in obscured surces and its evoution. Type 2 sources are a fundamental ingredient to test the main assumptions of XRB synthesis models (see subs.) and Unified Schemes (see subsec.).

- X–ray come from the innermost region of AGNs, and are the best way to study and understand directly the processes occuring close to the central black hole, apart from any subsequent reprocessing of radiaton.

- Wide area X–ray probe the accretion on wide luminosity and redshift intervals, and are fundamental in complementing deep pencil beam observations in detailed study of the nature and evolution of the AGNs.

In the context of the wide area surveys, the HELLAS2XMM survey provides a sample of $\sim$ 200 sources detected in $\sim$ 2 square deegre at fluxes in the range of $\sim 10^{-14} \div 10^{-12}\ erg\,cm^{-2}\,s^{-1}$.
The large area covered, the brigth X-ray fluxes and the hard X-ray (2–10 KeV) selection allowed us to obtain a statistically significant sample of obscured sources detected at fluxes where a significant fraction of the X-ray background (XRB) is resolved ($\sim$ 50%; see Comastri 2001 for a review) and at the same time optical spectroscopy is feasible with ground–based telescopes of the 4-8m classes.
The goals of the survey are the following:

- to derive, over a wide range of redshifts and luminosities, the luminosity function of obscured AGNs with a level of statistical accuracy adequate for a meaningful comparison with that of the unobscured AGNs.

- to study the evolution of the luminosity functions with cosmic time and to compare the results with models predictions (SAM).

To compare observational results and models predictions is not so straightforward.
Models are degenerate as regards BH masses and their accretion rates: AGNs with low BH masses but high accretion rates can produce the same luminosity of AGNs

with high BH masses and low accretion rates.

We try to disentangle degeneration problems through a characterization of our sources that allow us to study AGNs evolution in different ranges of BH masses and accretion rates.
The BH masses and accretion rates estimates have been derived through a detailed spectral and morphological study of the sources:

- Unobscured sources: we perferomed a detailed analysis of the optical Broad Emission Lines that allowed us to make use of the correlation between the FWHM of these lines and BH masses.
- Obscured sources: we perferomed a detailed morphological analysis of our sources. Quantitative morphology analyses allow us to study possible evolution of the galaxy structural parameters such as bulge/disk ratio, size, etc. Furthermore, using the well known relationships between black hole masses and properties of the bulges of the host galaxies, we can evaluate the black hole mass of our sources, and so their luminosity in terms of the Eddington one.

The thesis is organized as follow:

- Chapter 2 I will introduce the HELLAS2XMM survey, its strategy and the latest photometric and spectroscopic results.
- Chapter 3 I will introduce the study of luminosity function computed with HELLAS2XMM along with data from other deep surveys. I will describe the different approaches that our collaboration undertook and our results.
- Chapter 4 I will describe the morphological analysis mentioned above.
- Chapter 5 I will describe the spectral analysis of the type 1 AGNs
- Chapetr 6 I will report our first results

Chapter 2

The HELLAS2XMM survey

In this chapter I will delineate the strategy and the final aim of the HELLAS2XMM survey; I will describe the multiwavelength observations carried on the selected hard X–ray sources and our last results.

2.1 HELLAS2XMM

The XMM-Newton High Energy Large Area Survey (hereafter HELLAS2XMM) has been originally conceived as the natural extension of the BeppoSAX (HELLAS, Fiore et al. 2000) to the XMM-Newton capabilities, in order to fully exploit the larger throughput, effective area and better angular resolution of the new generation ESA satellite.

HELLAS2XMM is a serendipitous survey that uses suitable XMM-Newton archive observations (Baldi et al. 2002) with the goal of covering ~ 2 square degrees, using ten XMM-Newton fields.
To date the survey consists of a sample of 232 sources, selected in 10 XMM-Newton fields in the $2--10$ keV band at fluxes in the range 6×10^{-15}–4×10^{-13} $erg\,cm^{-2}\,s^{-1}$ (where a significant fraction, $\sim 50\%$, of the X-ray background is resolved; see Comastri 2001 for a review), with complete medium-deep optical photometry ($R = 24-25$), along with high signal-to-noise ratio optical spectra and broad-band (e.g. radio and near infrared) multiwavelength coverage for a large fraction of the objects.

The final aim of these project is to trace the accretion history in the Universe and to derive, over a wide range of redshifts and luminosities, the luminosity function of obscured AGNs with a level of statistical accuracy adequate for a meaningful comparison with that of the unobscured AGNs.

The large area covered allows the search for rare objects, which requires sufficiently wide areas to be discovered, and a more uniform coverage of the Hubble diagram; moreover the brigth X-ray fluxes and the hard X-ray (2-10 KeV) selection is essential to obtain a statistically significant sample of obscured sources.
The flux limit of the HELLAS2XMM survey is a key ingredient of our strategy because it allows the optical photometric and spectroscopic identification of highly obscured sources (sources with high X-ray to optical flux ratio $X/O \sim 10$, Fig. 2.1) with ground-based telescopes of the 4-8m classes, arduous task for the flux limit of the ultradeep Chandra and XMM-Newton surveys (e.g. CDFN, Barger et al. 2003; CDFS, Szokoly et al. 2004; Lockman Hole, Mainieri et al. 2002).

Multiwavelength data have been fully exploited for a sample of 232 sources detected in the following XMM-Newton fields ($\sim$ 1.4 square deegre; Cocchia et al. in preparation):

- PKS 0537–286
- PKS 0312–770
- G158–100
- A2690
- Mrk 509
- A1835
- IRAS 13349+2438
- Mrk 421
- GD 153
- BPM 16274

The PKS 0537 and Mrk 421 fields were obtained with the MOS in large window-mode imaging configuration and for the A1835 field the central cluster was masked

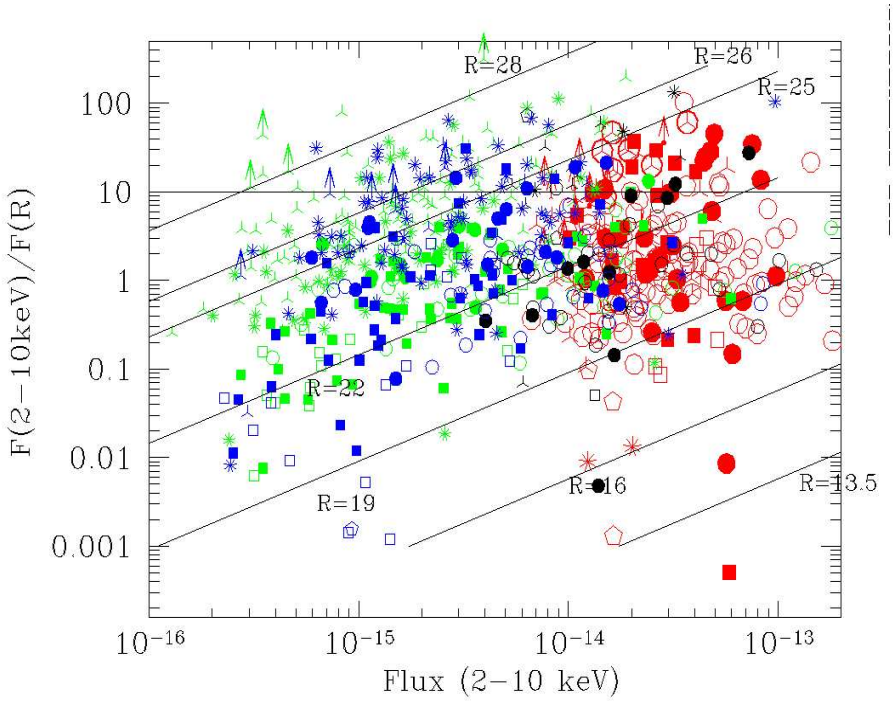

FIGURE 2.1. The X–ray (2-10 keV) to optical (R band) flux ratio X/O as a function of the X–ray flux for medium–deep and ultra–deep samples: HELLAS2XMM = open circles; CDFN = filled squares; LH = filled triangles; SSA13 = filled circles; skeleton triangles are sources without a measured redshift.
Solid lines mark loci of constant R band magnitude. The part of the diagram below the R = 25 line is accessible to optical spectroscopy with 10m class telescopes. HELLAS2XMM sources with $X/O > 10$ have R= 24–25, and their redshifts can be measured through optical spectroscopy.

(Fig. 2.2).
In the A1835, IRAS 13349+2438, Mrk 421, GD 153 and BPM 16274 small regions for which we don't possess deep optical photometry were excluded from the subsequent analysis.

The sky coverage and the Log(N)-Log(S) of the present sample are reported in Fig.2.3 and Table 2.1.

TABLE 2.1. **The Log(N)-Log(S) and the Sky-coverage of the HELLAS2XMM 2dF sample**

F_{2-10} keV	Integral Log(N)	$Err_{Log(N)}$	Sky-Coverage
cgs			deg^2
3.007e-13	0.7174	0.7174	1.393
1.843e-13	1.435	1.605	1.392
1.13e-13	5.753	2.845	1.387
6.928e-14	15.91	5.117	1.376
4.247e-14	37.89	8.7	1.254
2.604e-14	79.42	14.59	0.9882
1.596e-14	169.7	25.61	0.641
9.787e-15	353.0	52.95	0.09493
6e-15	698.7	208.5	0.01521

The XMM-Newton archival fields PKS 0312–770 and PKS 0537–28 share a Chandra coverage which, thanks to the higher angular resolution, helps in the process of optical identification (i.e., see Brusa et al. 2003).

2.2 X–ray detections

The XMM-Newton observations of the ten fields of the HELLAS2XMM 2dF sample have been obtained with the European Photon Imaging Camera (EPIC, Jansen et al.2001), equipped with both the MOS and the pn instruments.
The data were processed using version 5.0 of the Science Analysis System[a] (SAS). The event files were cleaned up from hot pixels and soft proton flares.

[a] *http : //xmm.vilspa.esa.es/external/xmm_sw_cal/sas_frame.shtml*

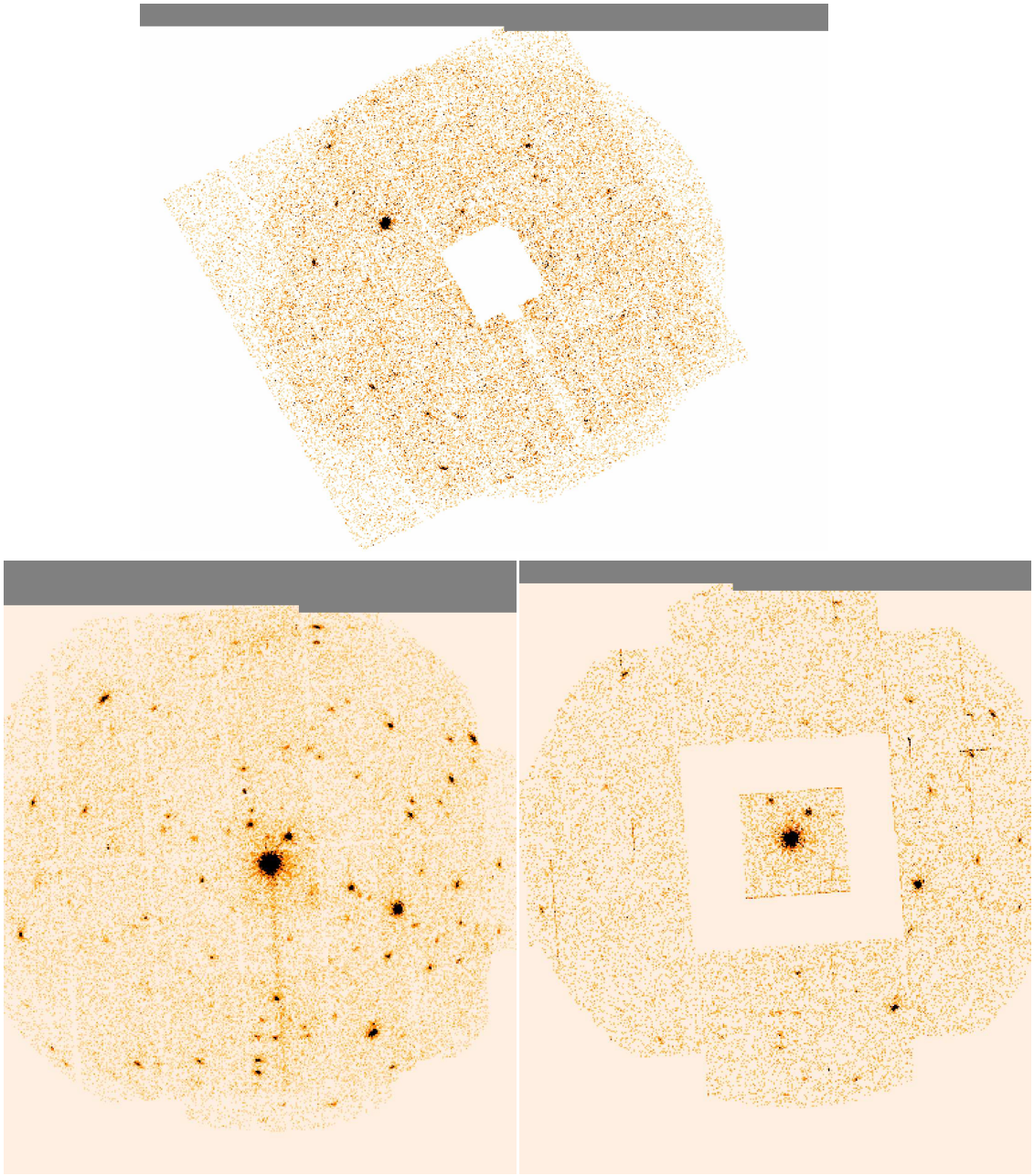

FIGURE 2.2. Examples of X-ray images. Top: the pn+MOS image of the A1835 field; bottom: the pn+MOS (left) and the MOS (large window-mode; right) images of the PKS 0537 field.

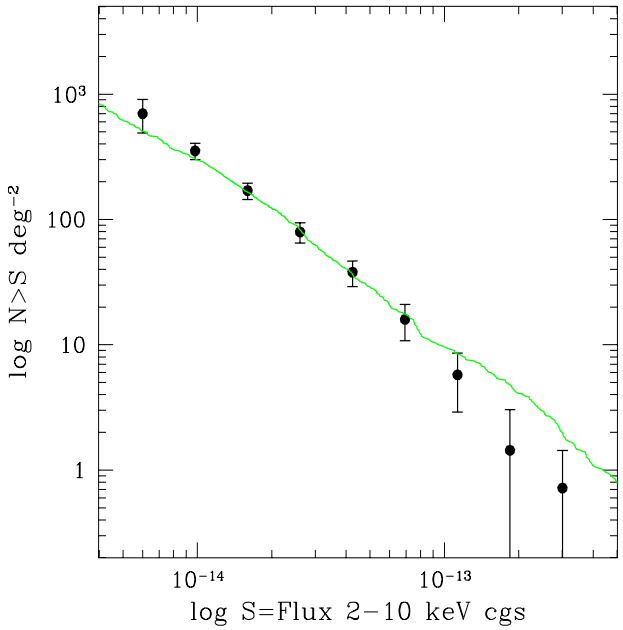

FIGURE 2.3. The Log(N)-Log(S) of the present sample. The green solid curve is from Moretti et al. 2003 compilation..

The hot pixels were removed using both the XMM-SAS and the IRAF[b] task *cosmicrays*; the soft proton flares were removed appling a count rate treshold eliminating all the time intervals with a count rate greater than of 0.15 c/s in the $10-12.4$ keV energy range for the two MOS and greater than 0.35 c/s in the $10-13$ keV energy range for the pn unit (Baldi et al. 2002).
The excellent relative astrometry among the three cameras (within 1", below their FWHM of $\sim 6''$) allows us to merge the MOS and pn images in order to increase the signal–to–noise ratio and to reach fainter X–ray fluxes.
An accurate detection algorithm developed by the HELLAS2XMM collaboration (Baldi et al. 2002) was run on the 2–10 keV cleaned events in order to create a list of candidate sources: 232 sources were detected above a probability treshold of $p = 2 \times 10^{-5}$ corrisponding to 1 spurious source per field.
The count rate to flux conversion factor was derived assuming a power law with photon index $\Gamma = 1.8$, absorbed by the Galactic column density toward the XMM fields (Dickey and Lockman 1990), and weighted by the effective exposure time of

[b]IRAF is distributed by the National Optical Astronomy Observatories, which is operated by the Association of Universities for Research in Astronomy, Inc, under the cooperative agreement with the National Science foundation.

the different EPIC cameras.
The uncertainty in the derived fluxes is $< 15\%$ for $\Delta\Gamma = \pm 0.5$.
The 2-10 keV fluxes range from $\sim 6 \times 10^{-15}$ to $\sim 4 \times 10^{-13}$ $erg\ cm^{-2}\ s^{-1}$.
In Table 2.3 Xid (col. 1); X-ray position (h:m:s, deg:m:s; col. 2-3) and the 2-10 keV flux (col. 7) are reported.
The same detection algorithm was run on the 0.5–2 keV energy range in order to characterize the average spectral properties of the sources in our sample using the hardness ratio technique.

For the majority of our sources we extracted and analysed the X–ray spectra. For the sources in the sample with at least 40 counts in the combined MOS+pn dataset (all but three) the source spectrum and the associate background and response files have been extracted from the original event files, in each of the XMM–Newton detector, using the standard SAS procedures (Puccetti Phd thesis). In the majority of the cases the spectral counts were fitted using the X–ray spectral fitting package XSPEC[c] (version 11.2.0) and the χ^2 statistic with a simple absorbed power–law model in order to derive the intrinsic N_H. When the spectral counts were lower than 120, the C-statistic (Cash 1979) was used instead.
The sources with spectroscopic redshifts and those without were treated separately. A detailed description of the spectral fitting procedure and results is reported in Perola et al. 2004 and Puccetti Phd thesis.

2.3 Additional X-ray observations: Chandra data

The XMM-Newton fields of PKS $0312-77$ and PKS $0537-28$ were also observed by Chandra, the first as part of the Performance and Verification phase of the satellite, the second in the framework of the HELLAS2XMM project.
The data were analyzed using version 2.2 and 3.0 of the Chandra Interactive Analysis of Observations (CIAO) software[d].
The high–background intervals were filtered out leaving about 24.7 and 20 ksec of useful data, respectively.
The WAVEDETECT algorithm (Freeman et al. 2002) was run on the cleaned full band ($0.5-8$ keV) images setting a false–positive threshold of 10^{-7}, which led to highly reliable detections, as shown in the CDFN field (e.g. Brandt et al. 2001a).

[c] *http://heasarc.gsfc.nasa.gov/docs/xanadu/xspec/*
[d] *http://cxc.harvard.edu/ciao/*

2.4 Optical counterparts

2.4.1 Optical imaging and source identifications

We have obtained relatively deep (R= 24–25) optical images for almost all the hard X-ray sources in the HELLAS2XMM sample using EFOSC at the ESO 3.6m telescope, DOLORES at the TNG telescope and FORS1 at the ESO VLT 8m telescope. Exposure range typically between 180 and 900 s per image.
The images were reduced using standard IRAF routines.
For each observing run, we obtained the proper bias by combining several bias frames with a median filter. The images were then corrected for pixel to pixel response variations using the median of several flat–field frames obtained during the night. Cosmic rays and bad pixel corrections were applied to each frame. The photometric calibration was performed for each night using the zero-point derived from the measured instrumental magnitudes of standard stars and assuming the average extinction reported in the Observatories web pages.
Each R–band frame was cross–matched to the USNO catalog (Monet et al. 1998) and astrometrically calibrated using GAIA[e] and IRAF packages. We obtained good astrometric solution for each frame with r.m.s. in each coordinate of about 0.1–0.2 arcsec.
Object detection was performed using SExtractor (Bertin and Arnouts 1996).
Since the images were obtained under different seeing conditions (from 1.″1 to 2.″1), we used different threshold values from image to image so that the faintest detectable sources in all frames have a minimum signal–to–noise ratio of $2 \div 3$ over the seeing disk.
As a measure of the total source magnitude we adopted the mag–best magnitude calculated by SExtractor.

Optical and X-ray images were brought to a common astrometry: we have accounted for the astrometric calibration of the X-ray images by looking for average displacement of bright Type 1 AGN (from 5 up to 15 sources) in the fields.
Typical systematic shifts were of the order of 1"; the maximum shift was of $\sim 2''$.

The uncertainties in the determination of the X-ray positions are mainly ascribed to the XMM-Newton point spread function (PSF) in particular at fainter fluxes where the statistical error in RA and DEC determination are expected to be in the range $1'' - 2''$ (Sect. 6.3 in the first XMM-Newton Serendipitous Source

[e]version 2.6.12 driven P.W. Draper from the Skycat software developed by ESO

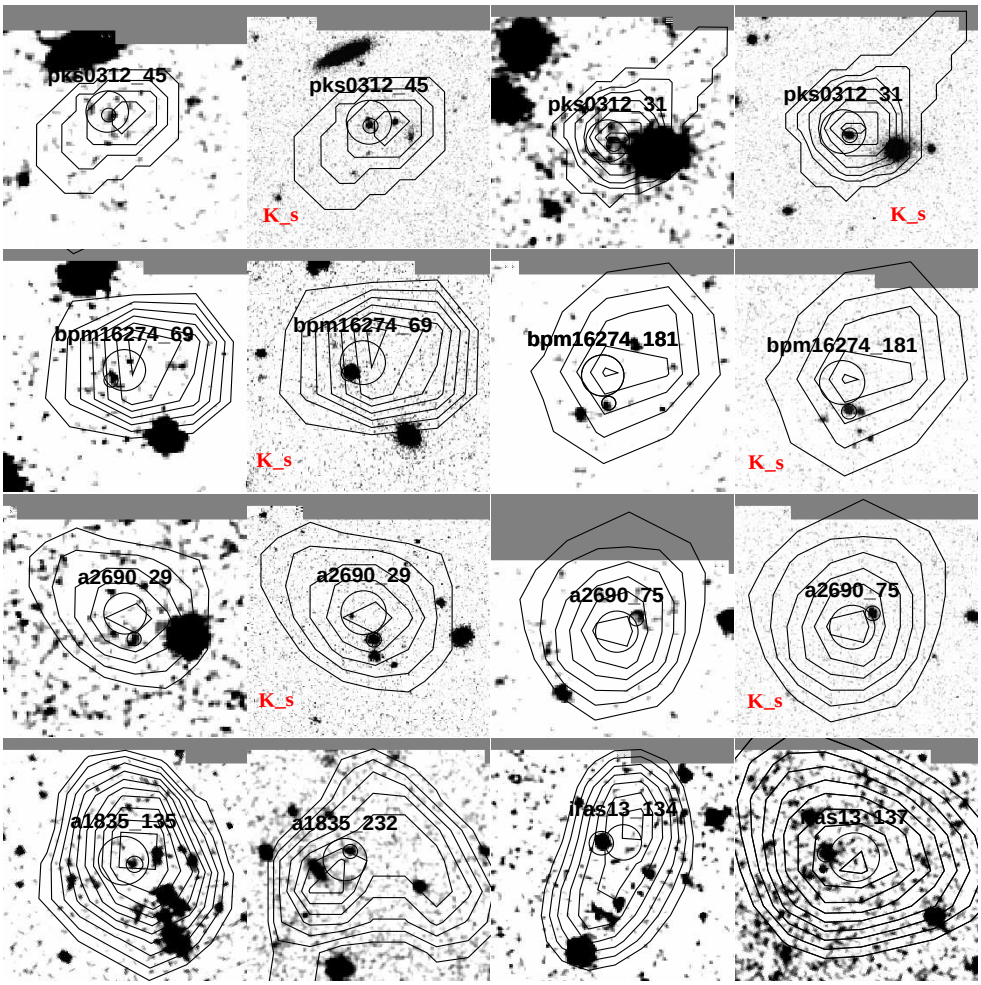

FIGURE 2.4. R and K_S (see sect. 2.5) images: circles represent the XMM–detection error–box (3″) and the optical counterpart (1″); superimposed the X–ray contours.

Catalogue: 1XMM, User Guide to the Catalogue).
In order to accomadate any residual systematics in the astrometric calibration of the EPIC images (see Barcons et al. 2002) and to fully account for th PSF broadening in faint sources (e.g. sources with < 100 cts), we have searched for optical counterparts for all the X–ray sources within a conservative matching radius of 6″ from the astrometrically corrected X–ray centroid.

Each optical image has been carefully inspected to securely identify the optical counterparts responsible for the X–ray emission: the region within the error–box of each X–ray detected source has been visually looked over and checked with the

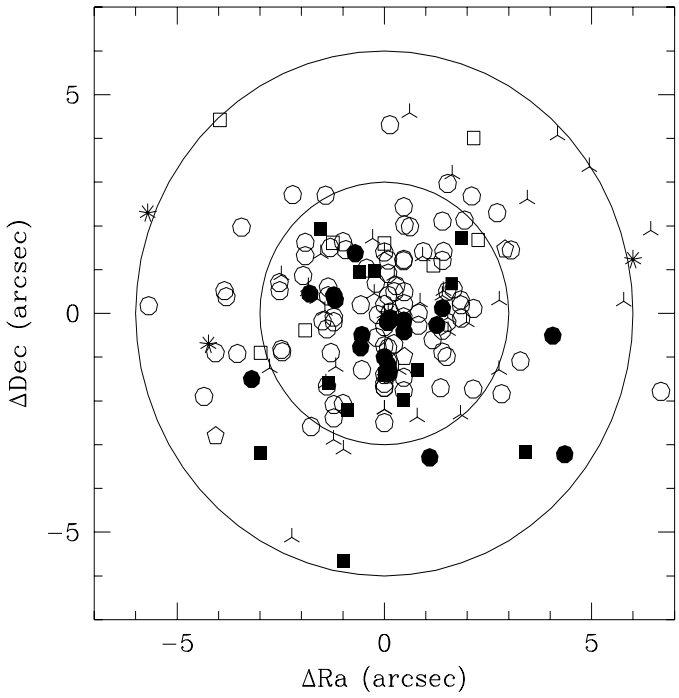

FIGURE 2.5. The displacement between the X–ray position and the position of the nearest optical counterpart for the HELLAS2XMM sample sources.
Open circles = broad line AGN; filled circles = narrow line AGN; filled squares = emission line galaxies; open squares = normal galaxies; stars = stars; pentagons = clusters of galaxies; skeleton triangles = unidentified objects.
The two circles have radii of 3 and 6 arcsec.

X–ray contours (Fig. 2.4).

We found optical counterparts brighter than $R \sim 25$ within $6''$ from the X–ray positions in 211 cases (actually within $3''$ for $\sim 76\%$ of the cases, see Fig. 2.5). The average displacement between the X–ray and optical positions is consistent with the results from other XMM–Newton surveys: $2.2'' \pm 1.5''$ (Barcons et al. 2002; Hasinger et al. 2001).

In Table 2.3 the optical position (h:m:s, deg:m:s; col. 4–5); the X-optical displacement (col. 6); the R magnitude (col. 8); the redshift and optical classification (col. 9-10) are reported.

2.4.2 Optical spectroscopy

The spectroscopic follow–up observations of the optically bright population ($R < 22$) have been performed with the ESO 3.6m (EFOSC2) and TNG telescopes (DOLORES) during four different observing runs (Jan 2001 Mar 2002).

At the ESO 3.6m telescope we used mostly the EFOSC2 #13 grism with a 1.5 arcsec slit which yields a dispersion of about 2.8 $\dot{A}$ per pixel; at the TNG telescope we used the DOLORES LR–B Grm1 for a dispersion of about 2.8 $\dot{A}$ per pixel with a 1.5 arcsec slit. For both instrumental setup we obtained a good spectral coverage in the range of $\sim 3800 \div 9000$ $\dot{A}$.
The exposure times vary between 600 and 2400 s, depending on the target magnitude.

The spectroscopic follow-up of the remaining sources with $R = 22 \div 24$ has been performed in service and visitor mode with the ESO VLT (UT1-UT2) telescope equipped with FORS1 during periods 69 and 72. A total of 40 hours of VLT has been devoted to this program.
We used the 150I grism with 1.2-1.3 arcsec slits providing a dispersion of 5.5 $\dot{A}$ per pixel and a wide spectral coverage $\sim 3500 \div 10000$ $\dot{A}$. The exposure times range from 480 up to ~ 7000 s; dithering of the targets along the slits was applied for the faintest objects in order to optimally remove the fringing at wavelengths longer than 7500 $\dot{A}$.

All the spectroscopic data have been reduced using standard IRAF packages.
Bias exposures taken on each night were stacked and subtracted out.
The bias-subtracted frames were flat–fielded in a standard manner using internal lamp flats obtained during the same night.
The sky background was removed by fitting a third–order polynomial along the spatial direction in source free region.
In all the observing runs the wavelength calibratin was made using arc lamps (He-Ar for the EFOSC2 data; He-Ar-HG for the FORS1 data; He for the TNG data).
The flux calibration of the spectra was obtained using observations of spectrophotometric standard stars performed within a few hours from the spectroscopy of the targets.

We have obtained optical spectra with good S/N ratio of 157 out of the 209 sources with optical counterparts brighter than $R = 24$.
10 sources have counterparts with $24 < R < 25$ still accessible to VLT spectroscopy

but demanding exposure times too long for the time allocated to our VLT spectroscopic runs; for these counterparts, exploiting our optical and near–infrared imaging (see Sect. 2.5), we estimated photometric redshifts through their $R-K$ colors (full details in Mignoli et al. 2004); recently we obtained near–infrared (H and K bands[f]) spectroscopic identifications of 3 out of these sources confirming our previous estimates for 2 sources (Fig. 2.6)

The distributions of the X-ray and optical flux of the remaining 50 sources with optical counterparts brighter than $R = 24$ but without optical spectroscopy is consistent with that of the sources with optical spettroscopy therefore the optical spectroscopic identifications can be considered representative of the HELLAS2XMM sample sources with counterparts brighter than $R = 24$.

For 150 sources the optical spectroscopy produced reliable redshifts; in the remaining 7 cases the redshift determination is tentative, based on one faint, single line.

The spectroscopic completeness of the HELLAS2XMM sample is $\sim 70\%$, one of the highest completeness for surveys at the same limiting flux of HELLAS2XMM.

In Table 2.3 I report the redshift and optical classification (col. 9-10).

2.5 Near-Infrared observations

An interesting new population of X-ray sources is present in both the deep and shallow surveys. These objects are characterized by values of their X–ray–to–optical flux ratio $X/O = f_{X-ray}/f_{opt} > 10$ which are significantly larger than those observed for soft X–ray selected AGN in the ROSAT surveys ($0.1 < X/O < 10$; Lehmann et al. 2001; Zamorani et al. 1999). Almost by definition, sources with $X/O > 10$ have faint optical magnitudes.

Such extreme sources are present in the HELLAS2XMM survey.

These objects are again very challenging to be followed–up with the optical spectrographs attached to $8-10$m class telescopes, as they are both very faint ($R > 25$) and spread over a large area of sky, making unfeasible any deep exposures with multi–object instruments.

An alternative approach is to make use of the observed property that the optically fainter X–ray selected sources have, on average, redder colours (Giacconi et al. 2001;

[f]Observations where obtained with ISAAC at ESO-VLT during period 73. We used the low resolution mode with 1" slit (R$\sim$ 500) in the J (1.16-1.34 μm), H (1.48-1.76 μm) and K (1.97-2.5 μm) bands.

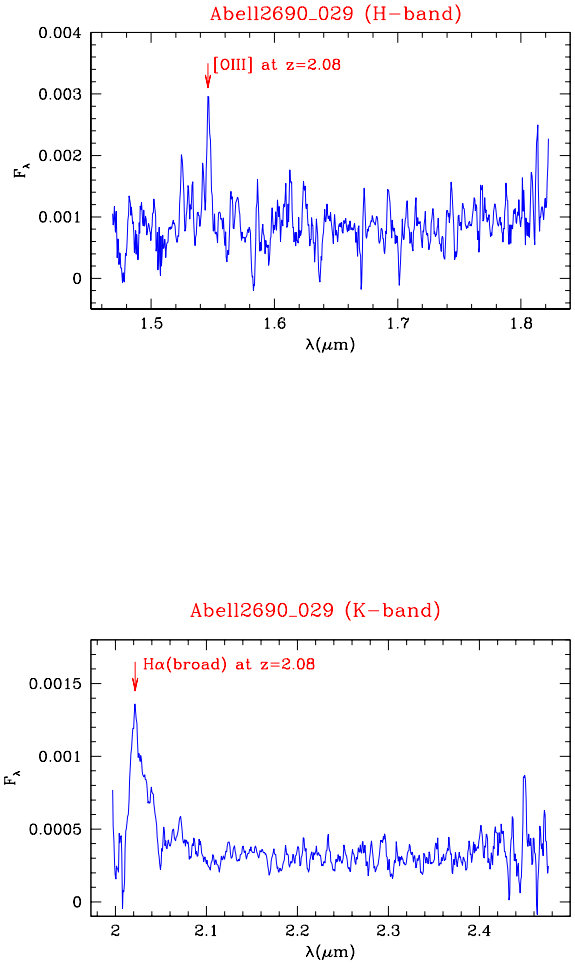

FIGURE 2.6. Near–infrared spectra of *A*2690_29: H and K band spectra, top and bottom respectively. The flux is in arbitrary units. (courtesy of R. Maiolino).

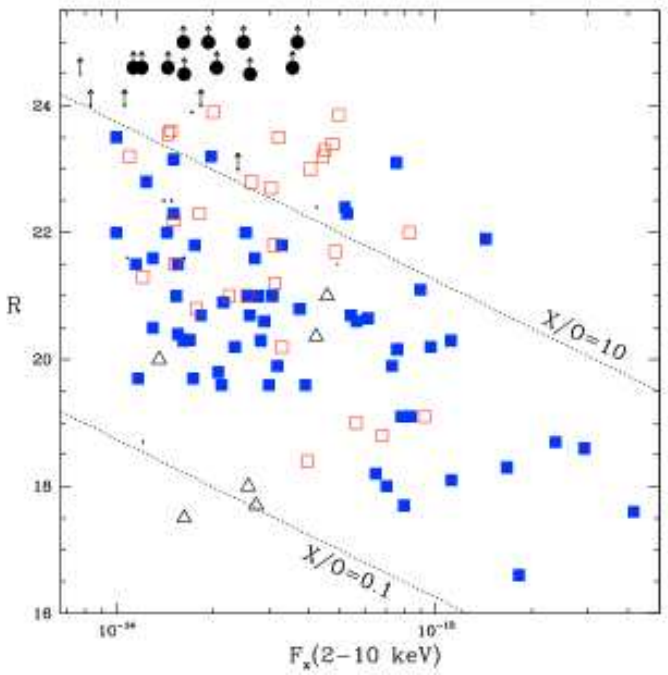

FIGURE 2.7. The optical (R band) magnitude versus the X-ray (210 keV) flux for the Hellas2XMM 1dF sample.
Different symbols identify different source classes: filled squares = broad line AGN; empty squares = narrow line AGN; triangles = early–type galaxies; small dot = spectroscopically unidentified sources. The selected sources observed with ISAAC are marked with large dots. The dotted lines indicate the loci of constant X–ray–to–optical flux ratio, delimiting the region of "conventional" AGN.

Lehmann et al. 2001; Alexander et al. 2002). This motivates the choice of the near infrared as the natural band to carry out a follow–up study of high X/O sources. On the basis of these considerations, we started a pilot study in the K_s[g] band, selecting a restricted (11 sources) but meaningful sample of HELLAS2XMM[h] sources that satisfy a well defined selection criterion: bright X–ray fluxes ($F_{2-10keV} > 10^{-14}$ $erg\,cm^{-2}\,s^{-1}$), high X–ray–to–optical flux ratios ($X/O > 10$) and no detection in the R band (see Fig. 2.7).

Deep K_s observations have been obtained with the infrared Spectometer And Array Camera (ISAAC, Moorwood et al. 1999) mounted on the ESO/VLT telescope. The observations have ben collected in service mode over several nigths in September

[g]The K_s short filter is centered at shorter wavelength than the standard K filter in order to reduce thermal background

[h]This pilot study started on a subsample of the HELLAS2XMM 1dF sources

2002 under good seeing conditions ($< 0.8''$), with net exposure time of 36 min for each field.
The data reduction has been performed in two steps: individual raw frames have been first corrected for bias and dark current, and flat fielded using standard IRAF routines. For the sky subtraction and image co–adding we then used DIMSUM[i] a contributed package of IRAF. The final co-added images show flat, zero leveled background and stable PSF over the field of view. A detailed discussion on data reduction and analysis tecniques is reported in Mignoli et al. 2004.
Object detection has been performed running SExtractor on the final images.
On the basis of the optical identification of the whole HELLAS2XMM survey, we know that all of the counterparts of our X–ray sources are within 6" from the XMM–Newton position (actually within 3 for $\sim 70\%$ of the cases). We therefore searched in the K_s catalog for objects closer than 6" to the X–ray position: in 10 out of 11 cases we found a relatively bright ($K_s < 19$) near–infrared source well within the error circle (see Fig. 2.8); we find one only exception, PKS0537–28 #037, in which no object is detected within the error box, but several relatively bright galaxies are present at distances less than 10" from the nominal X–ray position: in this case the X-ray flux is probably due to thermal emission from the hot intragroup gas.
Nevertheless, we cannot exclude the possibility that the true counterpart of this X–ray source might be either heavily reddened (e.g. similar to some AGN–hosting SCUBA galaxies, Ivison et al. 2000) or at very high redshift (Koekemoer et al. 2004).

Some of the most important results obtained from the analysis of high quality near-infrared images of hard X-ray sources with $X/O > 10$ are reported in Chapter 4 (all the details can be found in Mignoli et al. 2004).

2.6 Radio observations

Radio (5 GHz) observations of the field of PKS 0312-77 were performed with the Australian Telescope Compact Array (ATCA).
The data were analyzed with the software package MIRIAD and, at the end of the reduction phase, two individual images were combined together into a single mosaic. The accuracy on the radio position is of the order of $\sim 2''$ for the faintest objects.

[i]Deep Infrared Mosaicing Software, developed by P. Eisenhardt, M. Dickinson, A. Stanford and J. Ward, and available at $ftp://iraf.noao.edu/contrib/dimsumV2$

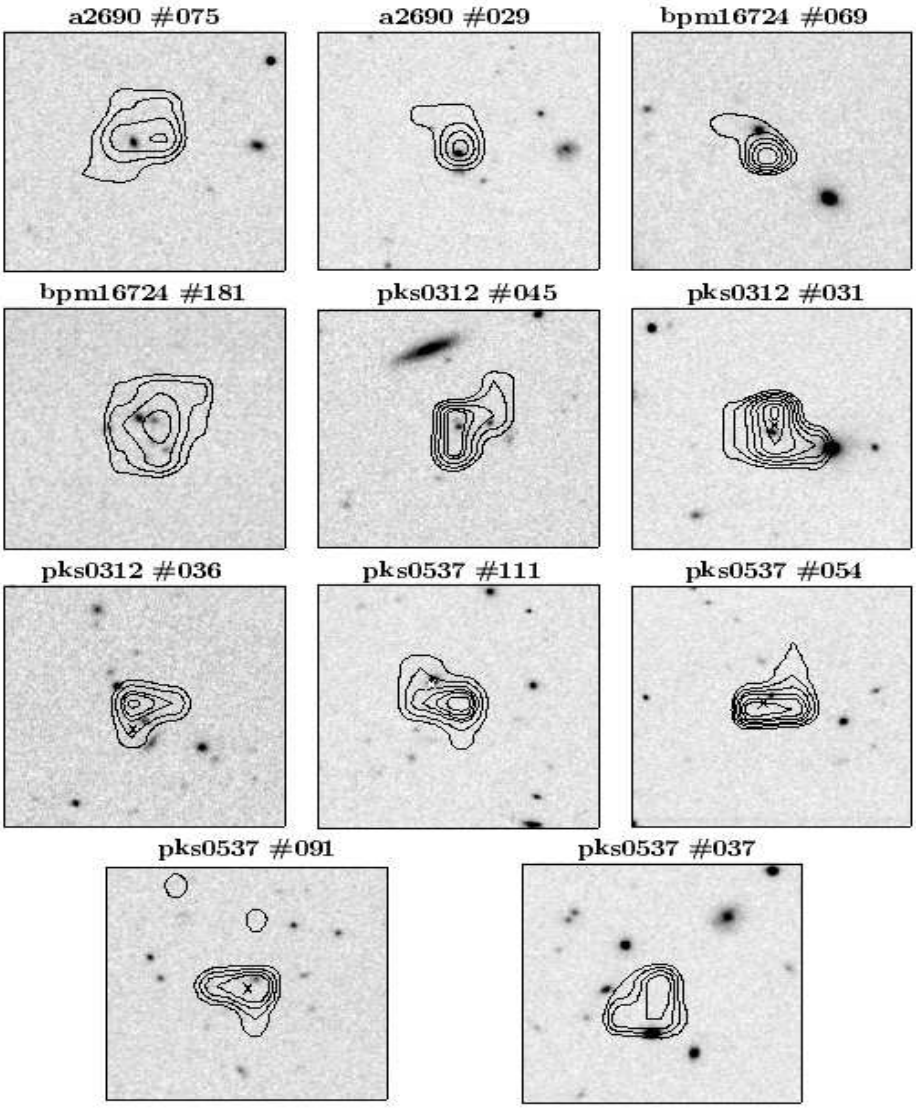

FIGURE 2.8. ISAAC K_s images, centered on the X–ray source centroid and 30" wide. North is to the top and east to the left. The X–ray contours are overlaid on each image. For 5 objects in the PKS 0312–77 and PKS 0537–28 fields we also show as a small cross the position of the source detected by Chandra.

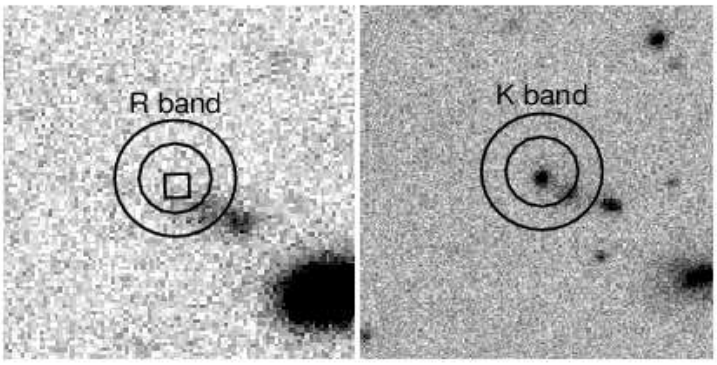

FIGURE 2.9. (left panel) R–band image of the source PKS0312–35. The small 1".5 width box represents the radio position detection; the 3" and 5" large circles are centered on the XMM–Newton position; (right panel) K–band image for the same source. Brusa et al. 2003.

Observations of the A2690 and G158 fields have been obtained with the Very Large Array (VLA) Telescope.
All the data were analyzed using the NRAO AIPS reduction package.
The accuracy on the radio position is of the order of $\sim 2''$ for the faintest objects.

Finally the source list in the PKS 0537 and MKN509 fields have been cross-correlated, using a conservative searching radius of 15", with the public NRAO/VLA Sky Survey radio catalog (NVSS, Condon et al. 1998; version 2.17).

Given the difference in the limiting fluxes in the different fields, the full radio database is not homogeneous and could not be used for statistical purposes. However, the radio informations, such as positional accuracy and radio flux, when available, has been extensively used in the identification of the X–ray counterparts and in the study of peculiar objects, respectively (see Fig. 2.9).
Full details about radio observations can be found in Ciliegi et al. 2003.

2.7 Source breakdown

In the majority of the cases optical spectra have sufficiently good quality to allow a reliable classification of the optical counterparts.
We divide our sources in the following category:

- **Broad Line AGN (AGN1):** sources with spectra with permitted broad emission lines with $FWHM > 2000\ km/s$;

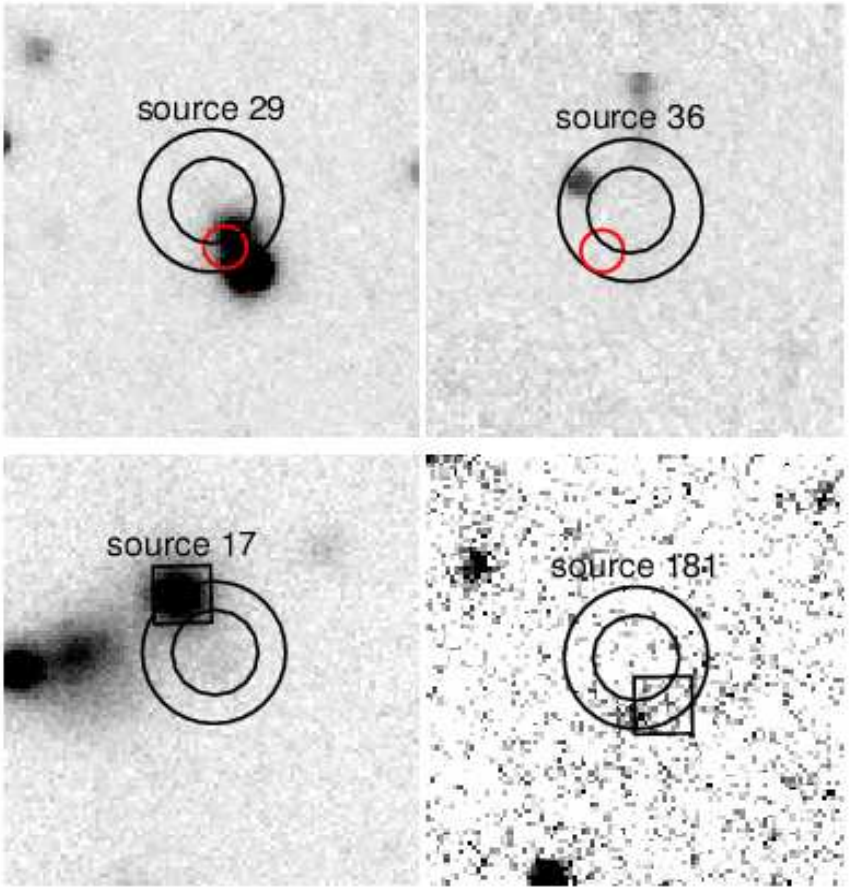

FIGURE 2.10. EFOSC2 R–band images of 4 sources in the field PKS0312 at a distance $> 3''$ from the XMM–Newton centroid. The 3"–5" circles are centered on the XMM–Newton detection. (top panels) sources 29 and 36: the small circles refer to the Chandra centroid and indicate a radius of 1."5; (bottom panel) sources 17 and 181: the squares refer to the radio centroids (4" width). Brusa et al. 2003.

- **Narrow Emission Line (AGN2):** soucers with spectra with permitted narrow emission lines with $FWHM < 2000\ km/s$;

- **Emission Line Galaxies (ELG):** extragalactic sources with spectra without obvious AGN features but with the presence of at least one, strong emission feature (e.g. strong [OII] or $H\alpha$ emission lines).

- **X-ray Bright Optically Normal Galaxies (XBONG) and Early type Galaxies (ETG):** objects with spctra without strong emission lines (equivalent width $EW > 5 - 8\ \dot{A}$) but with stellar absorption lines and a red continuum.

The source breakdown includes: 100 Type 1 AGNs; 26 Type 2 AGNs; 19 ELGs; 8 ETGs with $41.9 < logL_{2-10keV} < 44$ suggesting that they are all hosting an AGN (XBONGs); 3 ETGs associated with groups or clusters of galaxies; 4 stars.

In summary, 153 out of 160 sources with optical spectroscopy are associated with AGN, and the 66% are type 1 AGN.
The optical spectra of all the sources are available at the following link:
http : *//www.bo.astro.it/hellas/sample.html*.

In Table 2.3: Xid (col. 1); X-ray position (h:m:s, deg:m:s; col. 2-3); optical position (col. 4-5); X-optical displacement (col. 6); the 2-10 keV flux (col. 7); R magnitude (col. 8); redshift and optical classification (col. 9-10).

2.7.1 Broad Emission Line AGNs

The 100 objects with broad emission lines in the optical spectra have an average X-ray-to-optical flux ratio $< log(F_X/F_R) >= 0.12$ with a dispersion of 0.5 which is typical of soft X–ray selected Type 1 AGNs (Lehmann et al. 2001).

While a population of BL AGNs with unobscured X–ray spectrum is present at all redshifts and spans a wide range in luminosities, some examples of X–ray obscured BL AGNs are present at high redshifts and X–ray luminosities: in the HELLAS2XMM sample we find,from X–ray spectral analysis[j], 6 out of 100 optically

[j]The X–ray spectral analysis have been carried out for the 1dF HELLAS2XMM sample, full details in Perola et al. 2004

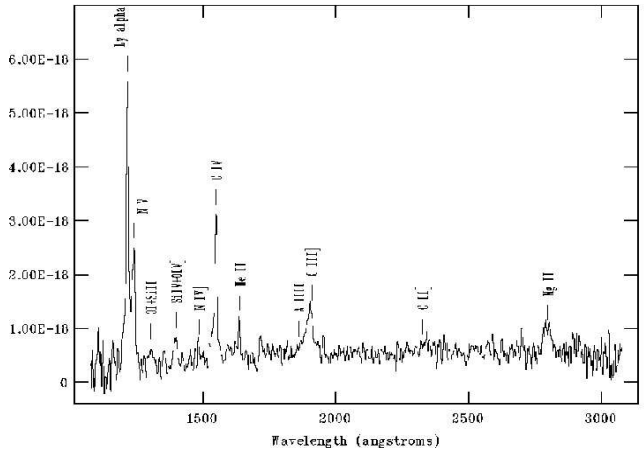

FIGURE 2.11. Optical spectrum of a X–ray absorbed, BL AGN at z=2.251 (PKS0312 #127).

classified BL AGNs whose $logN_H$ is greater than 22; for two objects the absorbing column is greater than 10^{23} at the 90% confidence level.

In these cases the spectroscopic classification turns out opposite to the X–ray classification, when the latter is based on the X–ray obscuration.
The $\sim$ 10% fraction (6/101) is in agreement with the finding by Page et al. 2003.
It is worth stressing that the 6 X-ray absorbed BL AGNs have $L_{2-10keV} > 10^{44}$ $erg\,s^{-1}$, while all the BL AGN with $L_{2-10keV} < 10^{44}$, i.e. the Seyfert 1 objects, have $log(N_H) < 22$.

A very interesting object is the highly absorbed ($N_H \sim 10^{23}$ cm^{-2}) source PKS03120–127 identified with broad line quasar at $z = 2.251$ on the basis of the MgII and CIII] lines (Fig. 2.11).

The other emission lines are narrow (FWHM < 2000 kms^{-1}) and the underlying continuum is very red if compared to that of optically selected BL AGNs (e.g. Brotherton et al. 2001).
For this source additional K band imaging is available: the optical counterpart is associated with a bright near–infrared source ($K = 18.4$) and have $R - K = 5.1$, considerably redder than that of high redshift quasars $R - K \sim 2$, suggesting a dominant contribution from the host galaxy.

As far as the multiwavelength properties (continuum shape, luminosity, hard X–ray spectrum, and upper limit on the radio emission) are concerned, this object is very similar to source N2_25 in the ELAIS survey (Willott et al. 2003) which is indeed classified as a reddened quasar at high redshift.

Some examples of broad emission line optical spectra are shown in Fig. 2.12.

2.7.2 Narrow Emission Line AGNs

Forty-five objects with narrow emission lines have been found.
On the basis of their optical lines ratios and intensities 26 are classified as Type 2 AGNs while the remaining 19 are Emission Line Galxies (cfr. Sect. 2.7).
All of these sources span the same redshift and luminsities ranges of AGN 1. Moreover, about half of the objects lie above the threshold of X–ray luminosity $> 10^{44}\ erg\,s^{-1}$ and can be therefore classified as QSO2.
It is also worth noticing that all but 3 of the ELGs have X-ray luminosities larger than $10^{43}\ erg\,s^{-1}$, typical of Seyfert 2 galaxies, strongly suggesting the presence of an active nucleus.

In the context of AGN unified schemes, Type 2 AGNs are expected to be intrinsically absorbed sources.
The average X–ray–to–optical flux ratio of AGN 2 and ELG in the present sample is $< log(F_X/F_R) >= 0.38$ with a dispersion of 0.95 which is larger than the average value observed for AGN 1. This is a first indication that the active nucleus is obscured at the optical frequencies.
The absorbing column densities estimated from the X-ray spectral analysis are generally as expected (larger than $10^{22}\ cm^{-2}$ at the 90% confidence level) confirming that the majority of the sources are X–ray obscured too.
However, one also finds 4 objects classified as AGN 2 with $N_H < 10^{22}\ cm^{-2}$. Here the most probably origin of the discrepancy is the complexity of the X-ray spectra, which is found in detailed studies of bright sources (Turner et al. 2000).
Similar examples of "unabsorbed Type 2" AGNs have been reported by Panessa and Bassani 2002 and Pappa et al. 2001.

Some examples of narrow lines optical spectra are shown in Fig. 2.13, 2.14

2.7.3 X–ray Bright Optically Normal Galaxies (XBONGs)

Among the 157 optically classified sources in the HELLAS2XMM sample 8 objects have been optically identified as early type galaxies.

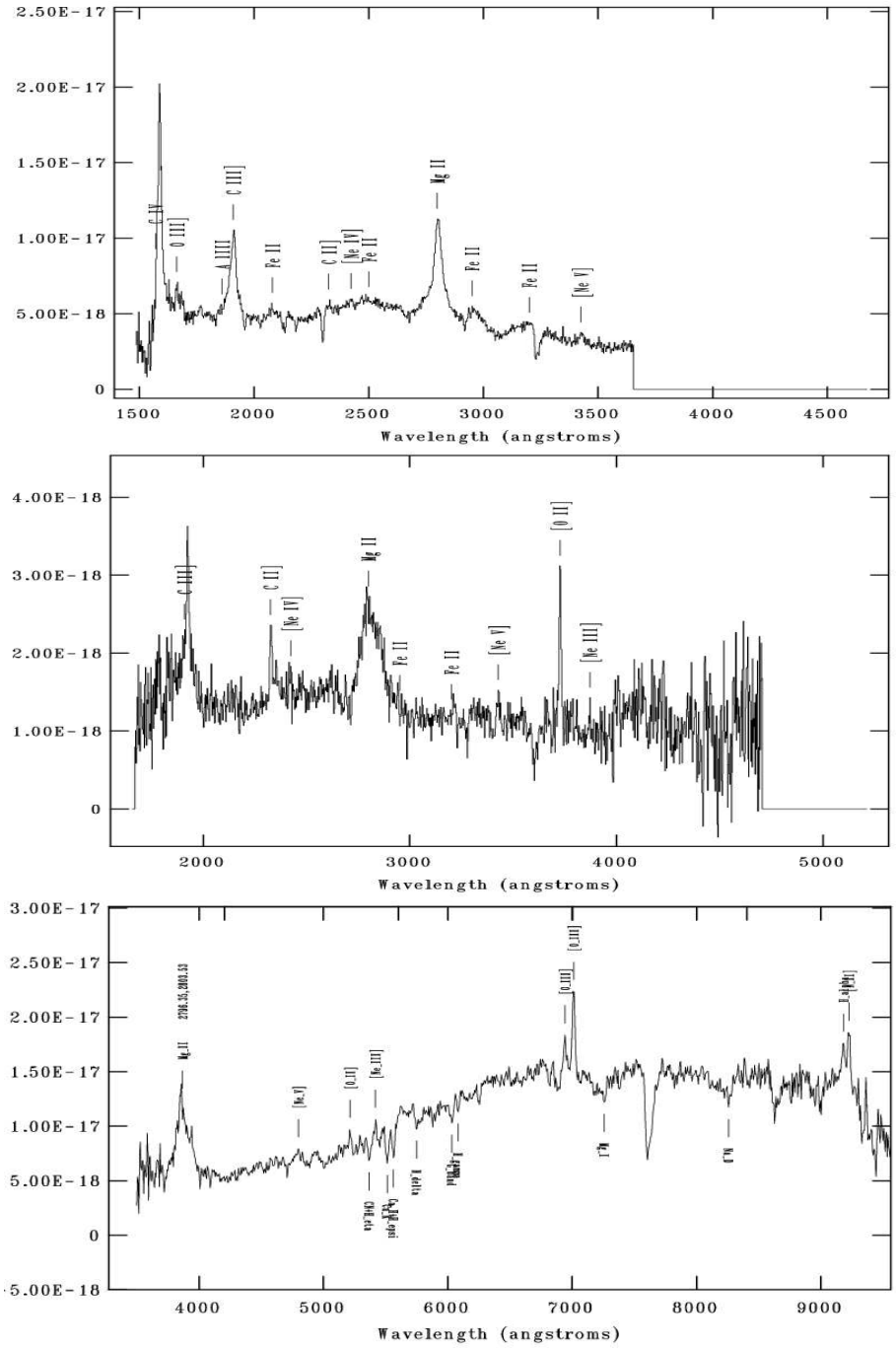

FIGURE 2.12. Optical spectra of broad emission lines sources. Top: A1835_281 ($z = 1.355$). Middle: A1835_80 ($z = 1.111$). Bottom: GD153_216 ($z = 0.401$); in this spectrum it is evident a strong contribution from the host galaxy ligth.

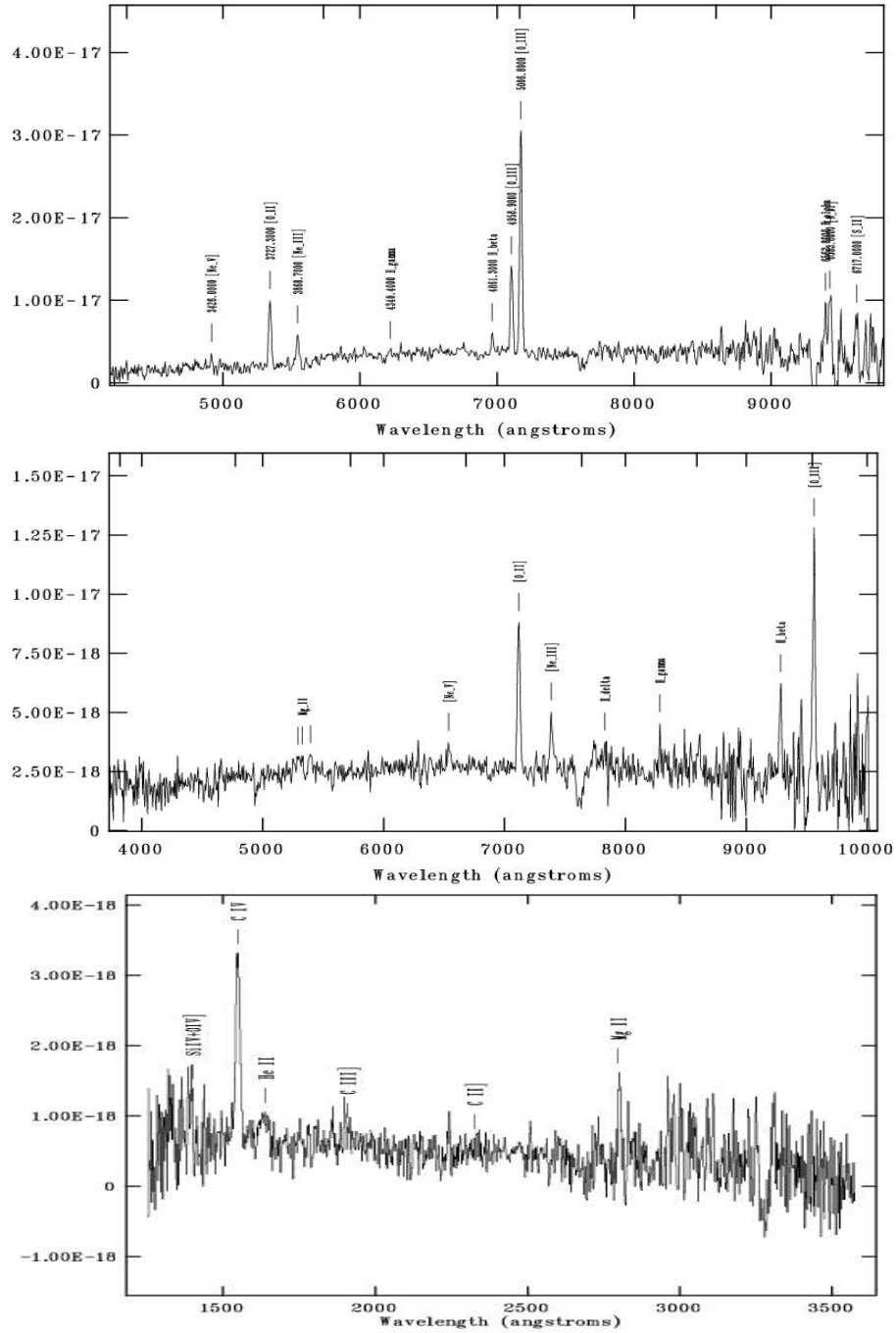

FIGURE 2.13. Optical spectra of narrow emission lines sources classified as AGN2. Top: A1835_256 ($z = 0.433$). Middle: GD153_236 ($z = 0.909$). Bottom: PKS0537_43 ($z = 1.797$).

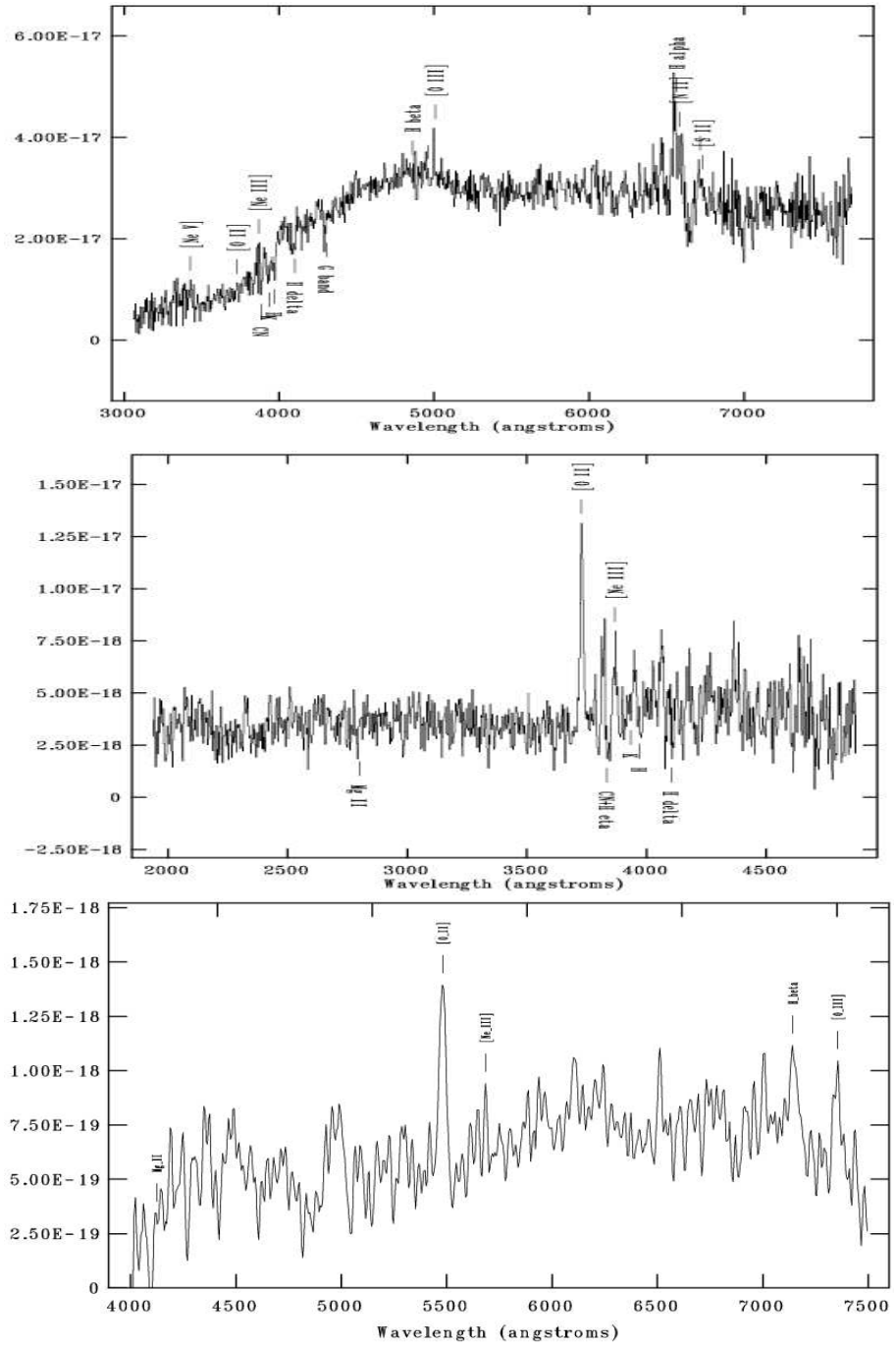

FIGURE 2.14. Optical spectra of narrow emission lines sources classified as ELGs. Top: PKS0312_14 ($z = 0.206$). Middle: A2690_38 ($z = 0.904$). Bottom: GD153_193 ($z = 0.470$).

These findings are in agreement with the results from both Chandra and XMM–Newton surveys that have revealed a population of X–ray emitting sources associated with the nuclei of galaxies without any obvious signature of AGN activity in their optical spectra (Mushotzky et al. 2000, Fiore et al. 2000, Barger et al. 2001, Giacconi et al. 2001, Hornschmeier et al. 2001, Comastri et al. 2001a,b, Severgnini et al. 2003, Georgakakis et al. 2004).
The unprecedent arcsec Chandra spatial resolution has unambiguously demonstrated that such a population of X–ray Bright Optcally Normal Galaxies (XBONGs, Comastri et al. 2002) is associated to luminous X–ray sources, confirming previous claims at bright X-ray fluxes based on lower spatial resolution Einstein nd ROSAT observations (Elvis et al. 1981, Griffiths et al. 1995).
The XBONGs X–ray luminosities span the range $10^{41} \div \sim 10^{43}\ erg\, s^{-1}$ and are therefore in between those of AGNs ($> 10^{43}\ erg\ s^{-1}$) and those expected for normal galaxies on the basis of the $L_X - L_B$ correlation of early type galaxies Fabbiano et al. 1992.
This can be seen in terms of X/O flux ratio: the average value of the XBONGs is $< log(F_X/F_R) > \sim -1$, while the typical value for AGN is ~ 0 and normal galaxies generally show $< log(F_X/F_R) > < -2$.
Although a few XBONGs could be luminous examples of otherwise normal elliptical galaxies whose X–ray emission arise from the integrated contribution of stellar sources, such a possibility, on the basis of X/O values, is clearly inconsistent with the majority of the objects.

The first object optically identified with a normal, early type galaxy for which a detailed multiwavelength study has been performed is the source 03120018.
This object was originally discovered by Chandra (CXOUJ 031238.9–765134, Fiore et al. 2000) and it is usually known as P3, being the third source catalogued in the field containing the quasar PKS $0312 - 77$.
A detailed description of the data reduction and analysis procedures is extensively reported in Comastri et al. 2002b.

Examples of optical spectra of XBONGs are shown in Fig. 2.15

2.8 Obscuration in the HELLAS2XMM 2dF sample

According to the so–called unified model (Antonucci 1993), the same engine is at work in all active galactic nuclei (AGNs). The differences between type 1 and type 2 AGNs are ascribed solely to orientation effects: our line of sight to the nucleus

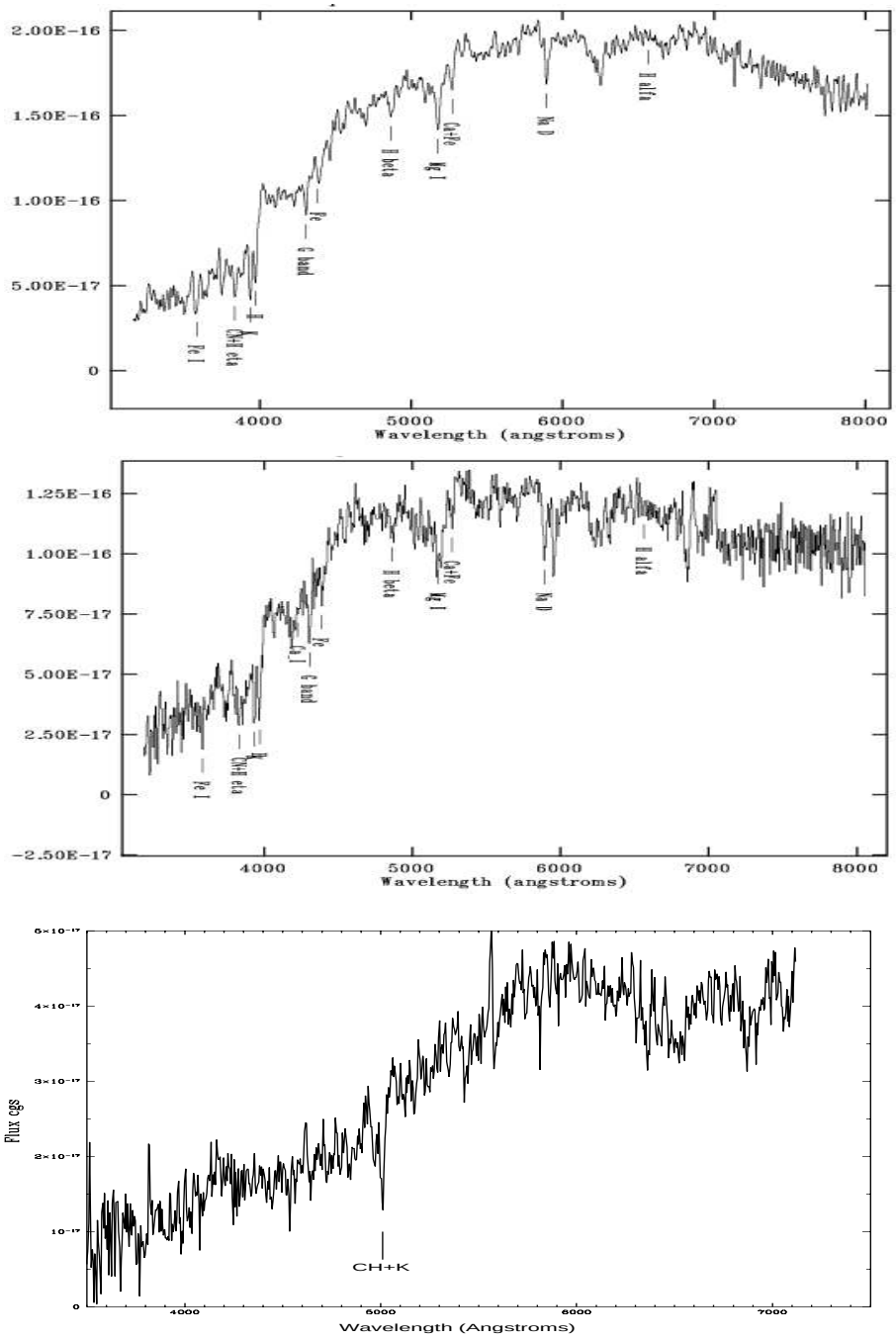

FIGURE 2.15. Optical spectra of X–ray Bright Optcally Normal Galaxies. Top: PKS0312_18 (P3; $z = 0.159$). Middle: A2690_13 ($z = 0.154$). Bottom: A1835_33 ($z = 0.265$).

may (type 2) or may not (type 1) be obstructed by optically thick material, perhaps distributed in a toroidal geometry.
Knowing the amount of obscuring gas in AGNs is important to understanding the physical properties and the nature of the putative torus, but is also relevant to other AGN–related issues, such as the cosmic X–ray background. Indeed, the distribution of the absorbing N_H is a key ingredient in background–synthesis models (Comastri et al. 1995; Gilli et al. 1999).
The intrinsic absorption also defines the source characteristics: for $N_H < 10^{24}\ cm^{-2}$, X–rays above a few keV can penetrate the torus, making the source nucleus visible to the observer and the column density measurable; in this case, the source is called " Compton thin". For values of N_H around a few $10^{24}\ cm^{-2}$, only X-rays in the $10 - 100$ keV range pass through the torus, so only data in this band allow an estimate of the source column density. For values of N_H higher than $10^{25}\ cm^{-2}$, X-rays above a few tens of keV are also absorbed (as photons, after a few scatterings, are redshifted down to the photoabsorption regime), and the nucleus is totally hidden from view; in these sources, only emission reflected by the torus (the cold reflected component) or scattered by warm material near the nucleus (the warm scattered component) is observed.
These so–called " Compton-thick" sources are extremely faint in X–rays, and therefore until recently only a few were known (Matt 1997).
Measuring the X–ray luminosity against an isotropic indicator of the intrinsic brightness of the source offers a method for evaluating N_H : assuming that the unifying theory is correct, the X–ray flux is depressed respect to this isotropic indicator by an amount related to the absorbing column density.
A good indicator of the intrinsic AGN flux is the intensity of the [O III] 5007 $\dot{A}$ emission line that is produced in the narrow–line region (NLR) on the 100 pc scale, and therefore is little affected by the nuclear obscuration on the parsec scale[k].
Therefore, if the [OIII] luminosity is proportional to the intrinsic luminosity, then an estimate of N_H is provided by the ratio between the observed X–ray flux and the [O III] flux.

We analysed our optical spectra and measured the [O III] flux, if present, and the

[k]Maiolino and Rieke 1995 showed that the host galaxy gaseous disk might obscure part of the NLR and it is important to correct the [O III] flux for large–scale absorption. The magnitude of the correction can be derived from the (narrow-line) Balmer decrement.

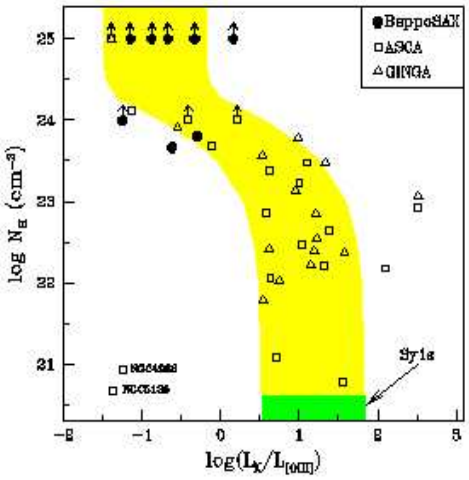

FIGURE 2.16. Distribution of the absorbing column density N_H as a function of ratio between the observed 2-10 keV luminosity and the (reddening corrected) [OIII] luminosity. Filled circles are Sy2s (Maiolino et al. 1998 and references therein). The shaded region indicates the expected correlation by assuming that L_X (2-10 keV) is absorbed by the N_H reported on the Y–axis, starting from the average $L_X/L[OIII]$ ratio observed in Sy1s (the width of the shaded region reflects the $\pm 1\sigma$ dispersion of the $L_X/L[OIII]$ distribution in Sy1s) and by assuming a 1% reflected component. Maiolino et al. 1998.

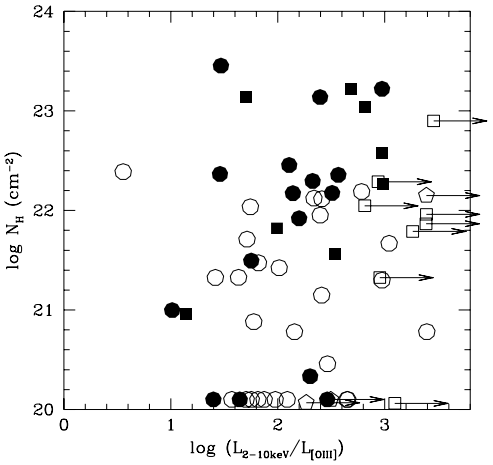

FIGURE 2.17. Distribution of the absorbing column density N_H as a function of ratio between the observed 2-10 keV and [OIII] luminosities.
Empty circles = Type 1, filled circles = Type 2, empty squares = ETGs, filled squares = ELGs, pentagons = clusters. Arrows indicate 3σ upper limits.

3σ[1] upper limits for XBONGs sources in order to compare our results to diagnostic diagrams, such as that in Fig. 2.16, and/or to obtain a clearer picture of the nature and distribution of the absorbing material in our sample.
Our results are reported in the last column of Table 2.3 and in Fig. 2.17.
We highlight that our [O III] flux measures are not corrected for large–scale absorption as the wavelenght range of our spectra doesn't allow the Balmer decrement estimates.

As we can clearly see from Fig. 2.17–Fig. 2.16 as our sample is X–ray flux limited selected we have no extreme sources, such as "Compton-thick" ones, and the range of $L_X/L[OIII]$ ratio is, on average, higher than optically (on the basis of $[OIII]$ flux) selected samples such as those reported in Fig. 2.16.
Furthermore, we note that the XBONGs subsample has the higher values of $L_X/L[OIII]$ ratio. The XBONGs subsample shares the same L_X distribution of the other sources so such $L_X/L[OIII]$ ratio values indicate, on average, lower $[OIII]$ fluxes (Fig. 2.18).
As already mentioned, [O III] 5007 $\dot{A}$ emission line is produced in the narrow–line region (NLR) on the 100 pc scale, and therefore should be little affected by the nuclear obscuration on the parsec scale unless in our sources:

- the obscuring torus or clouds covering factor is higher than normally assumed
- dust lane and gaseous disk obscure part of the NLR and extinguish the [O III] emission (Maiolino et al. 1998, Risaliti et al. 1999)

The analisys of the optical images of the XBONGs sample (Fig. 2.19) suggests that our sources are viewed mostly face–on so we favour the first hypothesis.

2.9 High X/O sources in the HELLAS2XMM survey

An interesting new population of X-ray sources is present both in deep and shallow surveys. These objects are characterized by values of their X-ray-to-optical flux ratio (f_X/f_{opt}) ten or more times larger than those typical of Broad Line AGNs and

[1]We estimated the upper limits through:

$$F_{[O\ III]\ up} = 3 \times rms \times \Delta\lambda$$

where $\Delta\lambda$ is the resolution element ($\dot{A}$/pixel) and the rms is evaluated on a wavelenght range centered on $5007(1+z)\ \dot{A}$

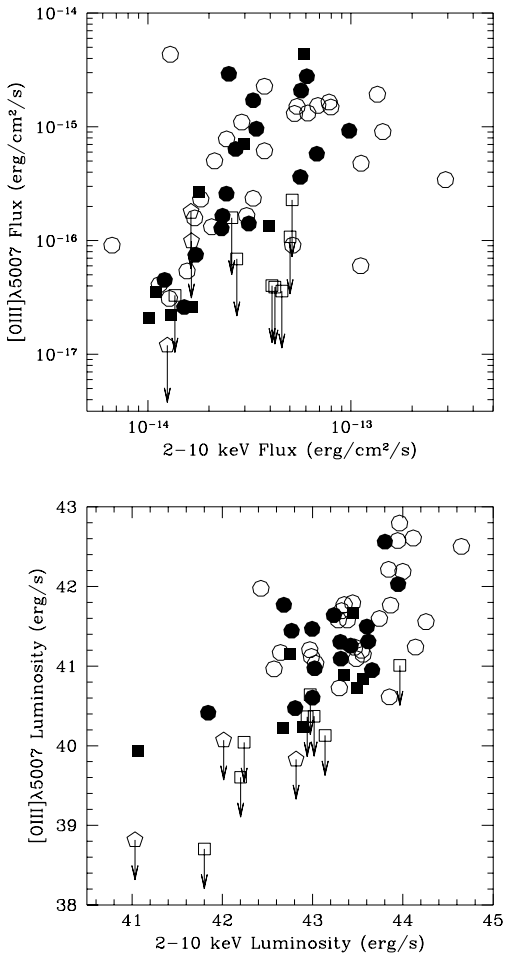

FIGURE 2.18. $[OIII]_{5007}$ flux and luminosity vs. $2-10\ keV$ flux and luminosity for the HELLAS2XMM 2dF sample.

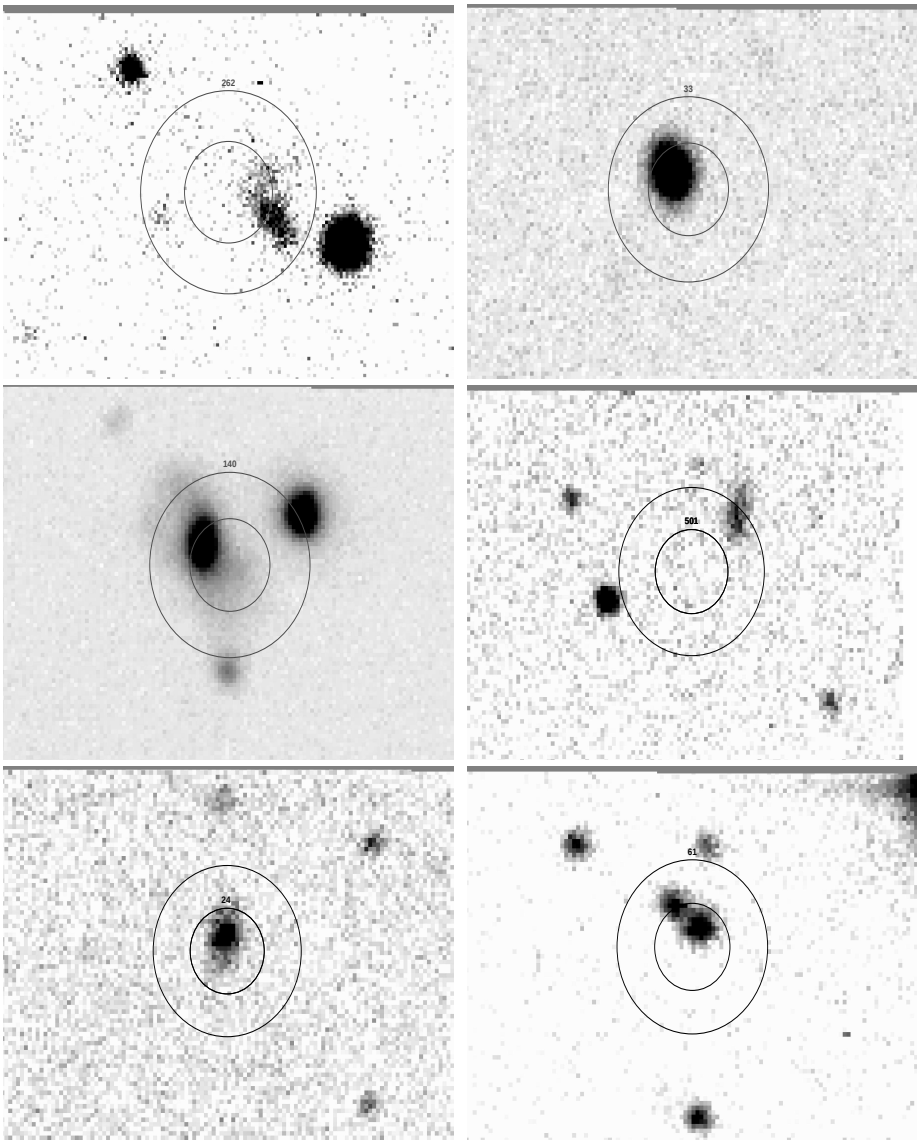

FIGURE 2.19. R band images of some XBONGs sources. From the top: A1835_262, A1835_33, A1835_140, PKS0312_501, PKS0537_24, Mrk509_61.

soft X-ray selected sources in the ROSAT survey ($0.1 < X/O < 10$; Lehmann et al. 2001; Zamorani et al. 1999; Alexander et al. 2001).
Almost by definition, sources with $X/O > 10$ have faint optical magnitudes.

It is reasonable to argue that most of the sources characterized by a high value of X/O are high redshift, obscured AGN.
Indeed, when an absorbing screen is present, the ratio between the optical to X-ray optical depth, in the observer frame, scales roughly as $(1+z)^{3.6}$, because dust extinction increases in the UV while X-ray absorption strongly decreases going toward the high energies.
The net result is that the observed optical flux of high-z QSOs can be strongly reduced and the observed magnitudes can be mainly due to the host galaxies starlight; conversely, the $2-10$ keV flux can be much less reduced.
The shape of the hard X-ray spectrum is responsible of a strong positive K-correction which "boosts" the X-ray flux and favours the detection of high redshift sources.
The hypothesis of high obscuration is supported by analysis of their X-ray spectral properties, as determined from X-ray colours which are harder than the average spectrum of objects with lower X/O (see Alexander et al. 2001; Mainieri et al. 2002).

The redshift and luminosity distribution of these sources are key parameters to test the Unified Schemes and the prediction of XRB synthesis models.
Indeed, if sources with large X/O were obscured AGN at $z > 1$, a natural consequence would be that a significant fraction of them (i.e. those detected at the brightest X-ray fluxes, $> 10^{-14}$ $erg\ cm^{-2}\ s^{-1}$) could belong to the population of high luminosity, highly obscured Quasar (QSO2) postulated in the simplest version of XRB models based on AGN unification schemes (i.e. Comastri et al. 1995), which so far have only scarcely been detected.
Moreover, they could contribute to reduce the disagreement between the redshift distribution predicted by XRB synthesis models and that observed in deep Chandra and XMM-Newton fields (Hasinger 2003; Gilli 2003), and provide an important contribution to the total energy density of the background light.

On the other hand, if they were at lower redshifts, they could belong to the population of rapidly evolving AGN postulated by Franceschini et al. 2002 and closely linked to starburst galaxies discovered in the infrared band with ISO, calling for substantial revision of the models (Gilli et al. 2001).

Since high luminosity, obscured quasars may also provide a relevant fraction of the black hole mass density due to growth by accretion, a much better knowledge of their space density and evolutive properties is needed to understand and quantify the evolution of the accretion with cosmic time.

It is interesting to note that the fraction of high X/O in hard X-ray samples is almost constant ($\sim$ 20%) down to $\sim 10^{-16}$ $erg\ cm^{-2}\ s^{-1}$ in the 2 Ms CDFN observations and over the entire range of X-ray fluxes sampled by deep and shallow surveys.
Spectroscopic redshifts for the sources detected at the brighter X-ray fluxes (as in the HELLAS2XMM) can be obtained with 10m class telescopes. Conversely, most of the $X/O > 10$ objects from ultra-deep Chandra and XMM-Newton surveys (e.g. CDFN, CDFS) have $R > 25$ and therefore are not accessible to optical spectroscopy (Fig. 2.1).
The redshift of the objects with $25 < R < 27$ could be determined through photometric redshifts technique, on the basis of good quality optical and near-infrared data and the comparison of the observed SED to galaxies and AGNs templates. This is also feasible with 10m class telescopes.
Spectroscopic and photometric redshifts of fainter sources must await next generation facilities like the $30 - 50m$ ground based telescopes and JWST.
In the meantime redshift esimates based on alternative approaches are needed, in particular the best hope to obtain information on luminosities and redshifts of this intriguing X-ray source population is to make use of the information gained at higher fluxes.

2.9.1 Spectroscopic classification of high X/O in the HELLAS2XMM sample

For all the sources in the HELLAS2XMM sample we have computed the X-ray to optical flux ratio.
The X-ray flux and the R magnitude are reported in Table 2.3; the R band flux is computed converting R magnitudes into specific fluxes and then multiplying by the width of the R filter. We used $f_R(0) = 1.74 \times 10^{-9}\ erg\ cm^{-2}\ s^{-1}\ \dot{A}^{-1}$ and $\Delta\lambda_R = 2200\ \dot{A}$ (Zombeck 1990).
32 objects in the HELLAS2XMM sample satisfy the selection criterion $log(X/O) > 1$. The high level of X-ray flux coupled with the large area surveyed allowed us to select a sizable subsample (17 objects) of objects with optical counterparts between $R = 22$ and $R \sim 25$, bright enough for reliable (optical or near–infrared) spec-

troscopic redshfits and classifications to be obtained with ground-based telescopes (see 2.4.2).
The identification breakdown of these sources is quite varied : 4 Type 1 AGN, 7 Type 2 AGN, 5 Emission Line galaxies (Table 2.2).
For the majority of these sources rest-frame column densities and unabsorbed 2-10 keV luminosity have been derived Perola et al. 2004.

TABLE 2.2. **High X/O sources with $22 < R <\sim 25$**

Id	$F_{2-10keV}$	R	Log(X/O)	Class	z	$LogL_{2-10keV}$	N_H
05370021	3.22e-14	23.5	1.325	43	1.192	44.34	21.2
0537011a	4.76e-14	23.4	1.455	93	0.981	44.29	22.12
05370164	1.49e-14	23.6	1.031	93	1.824	44.47	-
05370123	7.53e-14	23.1	1.534	93	1.153	44.32	22.82
03120006	8.28e-14	22	1.136	93	0.68	44.24	20
03120116	2.01e-14	23.9	1.281	43	0.814	43.74	-
26900075	2.06e-14	24.6	1.571	43	0.91	45.05	23.52
26900029	3.56e-14	25.1	2.009	90	2.08	45.11	22.31
26900072	4.05e-14	23	1.225	43	1.389	45.16	23.77
26900002	1.43e-13	21.9	1.333	90	0.8504	44.62	21.73
15800062	4.49e-14	23.3	1.39	93	1.568	44.69	23.42
50900001	4.97e-14	23.85	1.654	93	1.049	44.06	20
50900067	5.29e-14	22.3	1.061	90	1.076	44.3	20
50900013	4.42e-14	23.2	1.343	93	1.261	44.42	22.4
50900039	5.19e-14	22.4	1.093	90	0.818	43.62	20
42100066	3.66e-14	22.71	1.065	90	1.245	44.45	20.88
16274069	2.62e-14	24.08	1.468	43	1.35	44.38	22.5

All but 2 the sources have intrinsic hard X-ray luminosity $L_{2-10} > 10^{44}\ erg\ s^{-1}$, i.e. in the quasar regime.
Combining the luminosity and X-ray informations, one third of the identified sources (4 AGN2, 3 ELG) can be classified as "classic" Type 2 quasar, based on the absence of broad optical lines and X-ray obscuration in excess than $10^{22}\ cm^{-2}$.
Also present in this sample is an absorbed BL AGN that we can refer to as "X-ray Type 2 QSO".
These results strongly confirm that spectroscopic follow-up of high X/O selected in

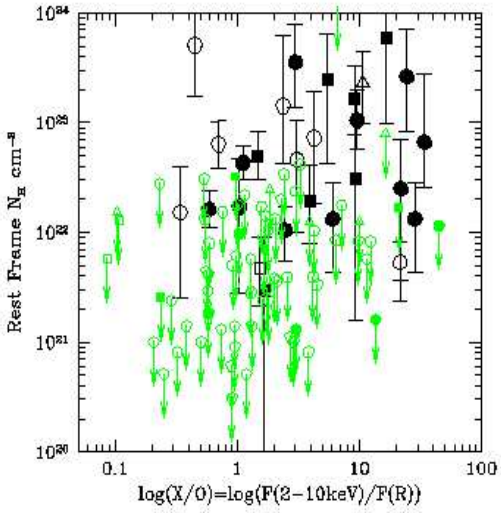

FIGURE 2.20. The best fit rest-frame absorbing columns from Perola et al. 2004 as a funtion of X/O for the HELLAS2XMM sample. Different symbols identify different classification of the optical spectra: open circles = type 1 AGN; filled circles = type 2 AGN; filled squares = emission line galaxies; open squares = earlytype galaxies. Open trianges refer to sources without optical spectroscopic identification. For these sources z=1 was assumed in the X-ray spectral fitting. Comastri & Fiore 2004

large area survey provide an efficient method to find high luminosity, narrow line objects: the paucity of Type 2 QSO among the identified sources in deep X-ray surveys might therefore be partly due to a selection effect since their flux limits allow to pick up, for the most of the cases, only sources too faint for optical follow–up (see Fig. 2.1).

The redshift distribution of the identified HELLAS2XMM high X/O spans the range $z \sim 1 \div 2$.

These results constitute the first spectroscopic proof over a statistically significant sample that high X/O sources (that constitute a significant fraction of the optically faint population) lie at $z > 1$.

2.9.2 Optical vs X-ray obscuration

Perola et al. 2004 found that most type 2 AGN in the HELLAS2XMM sample have significant obscuration (rest frame absorbing column $N_H > 10^{22}\ cm^{-2}$) also in the X-rays.

Perola et al. 2004 and A. and F. 2004 also found a good correlation between X/O and N_H, Fig. 2.20.

Both facts suggest that X-ray sources with $\log N_H > 22$ are likely to be also optically obscured AGN. However, for many weak sources in the samples N_H proper spectral fits are unfeasible and a rough spectral information can be derived from their softness ratio[m] only.
The correlation between the softness ratio and N_H is reasonably good (Perola et al. 2004) and therefore using the former to select X-ray obscured AGN, and in particular high X/O sources (Fig. 2.20), is not a bad approximation.
The relationship between X-ray obscured AGN and optically obscured AGN is, however, not one to one: $\sim$ 90% of type 1 AGN have $(S-H)/(S+H) > -0.5$ (i.e. most of them have a soft spectrum) and 70% of optically obscured AGN have $(S-H)/(S+H) < -0.5$ (i.e. the majority have a hard, likely obscured spectrum, but $\sim$ 30% have a soft spectrum).
This means that using a single $(S-H)/(S+H)$ threshold to decide whether an X-ray source with a faint optical counterpart is an optically obscured AGN has an intrinsically large uncertainty. For this reason, we instead compute for each source a "figure of merit" (FoM, Fiore et al. 2005 in prep.), using:

1) the X/O ratio and the fraction of obscured/unobscured sources as a function of X/O (see Fiore et al. 2003);

2) the morphology of the optical counterpart, i.e point-like sources are likely to be optically unobscured sources;

3) the probability distribution of the softness ratio for obscured and unobscured AGN, as estimated for the sources with spectroscopic redshift and classification in Table 3.3.

If a source has a FoM qualifying it as optically obscured we use the correlation we found between L_X and X/O for obscured sources, shown in Fig. 3.4, to estimate its redshift; if a source qualifies as an optically unobscured AGN we guess its redshift using the loose relation between X-ray flux and redshift for type 1 AGN.
These estimates should therefore be considered in a statistical sense only (Fiore et al. 2003). At fluxes lower than 10^{-14} $erg\ cm^{-2}\ s^{-1}$ only 30% of the sources qualify as unobscured AGN.

[m] The softness ratio is defined as $(S-H)/(S+H)$, where $S = 0.5-2$ keV flux and $H = 2-10$ keV flux.

In summary, on the basis of the optical identifications carried out in the context of the HELLAS2XMM survey and of the correlations found fully exploiting shallow and ultra-deep data we studied for the first time a population of optically obscured sources with high X/O, finding that most of them are QSO2.
These results allowed us to calibrate and test a new method to evaluate the properties of fainter, optically unidentifid obscured sources, in the ultra-deep surveys such as CDFN and CDFS: we suggest that this source population is dominated by luminous, obscured AGN at moderate and high redshifts (z $>$ 1).

TABLE 2.3. **The HELLAS2XMM 2dF sample**

Hard X–ray and optical properties of the X–ray sources detected in the H2XMM 2dF sample

Id	X−ray Ra	X−ray Dec	Optical RA	Optical Dec	Diff.	R	z	class	$F_{2-10keV}$	OIII
	J2000	J2000	J2000	J2000	arcsec				cgs	$erg\,cm^{-2}\,s^{-1}$
05370037	5 41 0.4	-28 39 5	5 41 0.7	-28 39 1	5.8	21.50	-1.0000	0	4.93e-14	0
05370015	5 40 54.3	-28 43 45	5 40 54.2	-28 43 47	2.4	19.90	0.8800	90	3.19e-14	0
05370022	5 40 51.3	-28 36 42	5 40 51.4	-28 36 46	4.3	-23.00	-1.0000	9	2.40e-14	0
05370175	5 40 45.6	-28 39 7	5 40 45.7	-28 39 8	1.7	19.80	1.2460	90	2.08e-14	0
05370008	5 40 34.2	-28 31 8	5 40 34.2	-28 31 9	1.2	19.00	0.3794	93	5.63e-14	3.62e-16
05370021	5 40 26.1	-28 50 39	5 40 26.3	-28 50 42	4.2	23.50	1.1920	43	3.22e-14	0
05370135	5 40 24.7	-28 46 16	5 40 24.6	-28 46 16	1.3	21.30	0.4844	93	1.21e-14	4.5e-17
05370043	5 40 22.1	-28 31 40	5 40 22.1	-28 31 40	0.2	22.70	1.7970	93	3.06e-14	0
05370091	5 40 21.2	-28 50 38	5 40 21.1	-28 50 38	1.2	23.70	-0.9000	0	2.50e-14	0
05370162	5 40 13.0	-28 44 2	5 40 13.0	-28 44 2	0.0	21.60	-1.0000	0	8.60e-15	0
05370019	5 40 10.6	-28 40 51	5 40 10.5	-28 40 53	2.7	20.30	1.3304	90	1.62e-14	0
05370072	5 40 4.4	-28 38 14	0 0 0.0	-0 0 0		-24.00	-1.0000	0	8.30e-15	0
05370159	5 40 2.7	-28 37 29	0 0 0.0	-0 0 0		-24.00	-1.0000	0	1.06e-14	0
05370031	5 40 0.8	-28 34 56	5 40 0.8	-28 34 56	0.2	20.50	3.2760	90	1.30e-14	0
05370007	5 39 59.0	-28 37 53	5 39 59.0	-28 37 53	0.2	20.60	0.8420	90	2.90e-14	1.1e-15
05370035	5 39 58.7	-28 37 7	5 39 58.7	-28 37 8	1.4	22.80	0.8970	90	1.24e-14	0
05370157	5 39 58.6	-28 41 26	0 0 0.0	-0 0 0		-24.50	-1.0000	0	7.70e-15	0
0537042a	5 39 57.5	-28 49 14	5 39 57.2	-28 49 14	3.8	21.60	1.9450	90	1.39e-14	0
0537042b	5 39 58.8	-28 49 19	5 39 59.0	-28 49 19	2.0	21.50	-1.0000	0	2.10e-14	0
05370013	5 39 57.2	-28 51 9	5 39 57.0	-28 51 8	2.6	22.00	0.9010	90	2.54e-14	0
05370017	5 39 57.0	-28 50 28	5 39 56.7	-28 50 27	3.9	20.70	0.9039	90	2.62e-14	0
05370153	5 39 56.1	-28 46 22	0 0 0.0	-0 0 0		-24.60	-1.0000	0	1.13e-14	0
05370012	5 39 52.7	-28 47 9	5 39 52.8	-28 47 9	1.5	22.50	-1.0000	0	1.49e-14	0
0537052a	5 39 50.4	-28 33 45	5 39 50.4	-28 33 45	0.4	21.50	1.6647	90	1.11e-14	0
0537052b	5 39 51.9	-28 33 45	5 39 51.8	-28 33 45	1.7	23.70	-1.0000	0	1.36e-14	0
05370004	5 39 49.9	-28 38 32	5 39 50.0	-28 38 32	1.5	18.00	0.8944	90	7.02e-14	0
05370054	5 39 45.3	-28 49 10	5 39 45.2	-28 49 10	1.3	25.10	-1.3000	0	1.62e-14	0
05370014	5 39 43.0	-28 27 20	5 39 43.1	-28 27 19	2.0	19.60	1.6591	90	3.00e-14	0
05370041	5 39 39.7	-28 31 43	5 39 39.8	-28 31 42	1.9	20.40	1.6436	90	1.56e-14	0
05370078	5 39 38.7	-28 48 7	5 39 38.7	-28 48 8	1.3	22.00	1.6220	90	1.44e-14	0
05370036	5 39 38.7	-28 52 49	5 39 39.2	-28 52 51	6.9	20.60	1.3290	90	5.65e-14	0
05370006	5 39 34.8	-28 41 16	5 39 34.8	-28 41 16	0.1	16.00	0.0000	10	2.02e-14	0
05370060	5 39 33.6	-28 35 19	5 39 33.7	-28 35 20	2.0	23.90	-1.0000	0	1.72e-14	0
05370003	5 39 29.5	-28 48 60	5 39 29.4	-28 49 0	1.2	18.10	0.3171	90	1.12e-13	4.78e-16
05370024	5 39 25.8	-28 44 56	5 39 25.7	-28 44 54	2.0	21.00	0.0750	40	4.57e-14	-1.2e-18

TABLE 2.2. **The HELLAS2XMM 2dF sample - continued**

Id	X−ray Ra	X−ray Dec	Optical RA	Optical Dec	Diff.	R	z	class	$F_{2-10keV}$	OIII
	J2000	J2000	J2000	J2000	arcsec				cgs	$erg\,cm^{-2}\,s^{-1}$
05370010	5 39 25.3	-28 32 37	5 39 25.4	-28 32 36	1.5	22.40	-1.0000	0	4.24e-14	0
05370002	5 39 23.5	-28 42 24	5 39 23.5	-28 42 23	0.9	16.60	1.2437	90	1.82e-13	0
0537011a	5 39 20.5	-28 37 22	5 39 20.5	-28 37 21	0.9	23.40	0.9810	93	4.76e-14	0
0537011b	5 39 21.6	-28 38 4	5 39 21.6	-28 38 6	2.5	21.70	-1.0000	0	8.80e-15	0
05370040	5 39 20.1	-28 36 37	5 39 20.1	-28 36 38	1.1	21.00	1.4849	90	1.54e-14	0
05370164	5 39 17.2	-28 38 20	5 39 17.1	-28 38 17	3.3	23.60	1.8240	93	1.49e-14	0
05370111	5 39 11.5	-28 37 17	5 39 11.6	-28 37 15	2.4	24.50	-1.4500	0	3.69e-14	0
05370009	5 39 10.7	-28 35 28	5 39 10.8	-28 35 26	2.5	20.80	0.7700	90	3.75e-14	2.27e-15
05370016	5 39 9.3	-28 41 5	5 39 9.4	-28 41 4	1.4	21.70	0.9950	93	4.84e-14	0
05370005	5 39 5.5	-28 33 17	5 39 5.5	-28 33 16	1.2	21.10	1.1580	90	8.94e-14	0
05370123	5 38 51.4	-28 39 49	5 38 51.5	-28 39 49	1.4	23.10	1.1530	93	7.53e-14	0
05370020	5 38 50.9	-28 37 57	5 38 50.9	-28 37 58	0.8	20.70	0.7630	90	5.43e-14	1.51e-15
03120012	3 15 29.4	-76 53 42	3 15 28.8	-76 53 40	2.5	21.00	0.5065	90	2.78e-14	0
0312020a	3 14 16.8	-76 55 60	3 14 16.5	-76 56 2	2.4	21.50	0.9640	43	1.61e-14	0
03120010	3 14 16.4	-76 45 37	3 14 16.5	-76 45 36	0.7	19.60	0.2456	90	2.13e-14	5.02e-16
03120022	3 13 49.0	-76 45 59	3 13 49.3	-76 46 0	1.3	21.60	2.1400	90	2.71e-14	0
03120036	3 13 43.5	-76 54 26	3 13 42.9	-76 54 24	3.2	24.70	-1.0500	0	1.45e-14	0
03120013	3 13 34.3	-76 48 30	3 13 34.5	-76 48 30	0.9	19.70	1.4455	90	1.17e-14	0
03120003	3 13 14.7	-76 55 56	3 13 14.3	-76 55 56	1.2	18.30	0.4200	90	1.67e-13	0
03120005	3 13 12.0	-76 54 30	3 13 11.8	-76 54 31	1.4	19.10	1.2740	90	8.37e-14	0
03120127	3 12 58.0	-76 51 20	3 12 57.9	-76 51 20	0.4	23.50	2.2510	90	1.00e-14	0
03120065	3 12 52.2	-77 0 59	0 0 0.0	-0 0 0		-24.00	-1.0000	9	1.47e-14	0
03120006	3 12 54.0	-76 54 15	3 12 53.8	-76 54 15	0.7	22.00	0.6800	93	8.28e-14	0
03120018	3 12 39.3	-76 51 33	3 12 38.7	-76 51 33	1.9	18.00	0.1590	40	2.59e-14	-5.3e-18
03120008	3 12 31.2	-76 43 24	3 12 31.3	-76 43 25	1.1	13.70	0.0520	50	1.64e-14	-3.3e-18
03120004	3 12 9.2	-76 52 13	3 12 9.2	-76 52 13	0.1	18.20	0.8900	90	6.49e-14	0
03120016	3 12 0.4	-77 0 26	3 12 0.5	-77 0 26	0.6	22.20	0.8410	93	1.51e-14	2.6e-17
0312089a	3 11 45.0	-76 56 45	3 11 44.4	-76 56 46	2.3	23.60	0.8090	43	1.30e-14	2.2e-17
03120181	3 11 36.0	-76 55 56	3 11 36.0	-76 55 60	3.8	23.20	0.7090	43	1.10e-14	3.5e-17
03120035	3 11 31.8	-77 0 36	3 11 31.8	-77 0 32	4.3	22.00	1.2690	90	1.83e-14	0
03120066	3 11 28.2	-76 45 16	3 11 29.2	-76 45 15	3.7	23.15	1.4490	90	1.51e-14	0
03120017	3 11 24.8	-77 1 39	3 11 25.4	-77 1 35	4.6	17.70	0.3199	40	2.74e-14	-2.3e-18
03120031	3 11 13.9	-76 53 59	3 11 13.6	-76 53 60	1.0	23.60	-0.8000	0	1.20e-14	0
03120029	3 11 13.4	-76 54 31	3 11 13.0	-76 54 34	3.1	18.80	-1.0000	0	1.21e-14	0
03120011	3 11 12.8	-76 47 2	3 11 13.3	-76 47 2	1.9	21.50	0.7530	90	1.56e-14	5.4e-17
03120009	3 11 5.6	-76 51 58	3 11 5.3	-76 51 58	0.9	23.20	1.5220	90	1.98e-14	0

TABLE 2.2. **The HELLAS2XMM 2dF sample - continued**

Id	X−ray Ra J2000	X−ray Dec J2000	Optical RA J2000	Optical Dec J2000	Diff. arcsec	R	z	class	$F_{2-10keV}$ cgs	OIII $erg\,cm^{-2}\,s^{-1}$
03120007	3 10 50.0	-76 39 4	3 10 50.2	-76 39 4	0.8	18.60	0.3812	90	2.92e-13	3.43e-16
03120021	3 10 49.8	-76 53 17	3 10 49.7	-76 53 16	0.7	22.30	2.7360	90	1.51e-14	0
03120028	3 10 37.4	-76 47 13	3 10 37.9	-76 47 11	2.5	20.80	0.6410	43	1.78e-14	2.69e-16
03120045	3 10 19.0	-76 59 58	3 10 18.9	-76 59 58	0.5	24.40	-1.6500	0	1.94e-14	0
03120002	3 10 15.8	-76 51 33	3 10 15.9	-76 51 33	0.5	17.60	1.1870	90	4.17e-13	0
03120124	3 10 1.6	-76 51 7	3 10 1.7	-76 51 8	1.3	22.50	-1.0000	0	1.41e-14	0
03120501	3 9 52.2	-76 49 27	3 9 51.0	-76 49 23	5.9	20.00	0.2049	40	1.36e-14	-1.1e-18
03120014	3 9 51.2	-76 58 25	3 9 51.4	-76 58 26	1.5	18.40	0.2060	43	3.97e-14	1.34e-16
03120024	3 9 31.7	-76 48 45	3 9 32.1	-76 48 46	1.8	21.80	1.8380	90	1.76e-14	0
03120116	3 9 18.5	-76 57 59	3 9 18.2	-76 58 0	1.1	23.90	0.8140	43	2.01e-14	0
0312034a	3 9 12.1	-76 58 26	3 9 12.1	-76 58 26	0.2	19.10	0.2651	93	9.80e-14	9.23e-16
26900038	23 59 57.2	-25 5 43	23 59 57.2	-25 5 44	1.4	21.00	0.9040	43	2.25e-14	0
26900075	23 59 56.6	-25 10 20	23 59 56.4	-25 10 18	3.3	24.60	0.9100	43	2.06e-14	0
26900039	23 59 39.8	-25 0 57	23 59 39.8	-25 0 57	0.2	19.60	0.9300	90	3.90e-14	0
26900028	23 59 33.4	-25 7 58	23 59 33.3	-25 7 57	2.0	21.80	0.7380	90	3.30e-14	2.35e-16
26900006	0 1 22.8	-25 0 19	0 1 22.7	-25 0 19	1.4	18.70	0.9640	90	1.22e-13	0
26900029	0 1 11.6	-25 12 3	0 1 11.5	-25 12 6	3.9	25.10	2.0800	90	3.56e-14	0
26900010	0 1 6.8	-25 8 46	0 1 6.8	-25 8 47	1.4	21.00	1.3547	90	3.08e-14	0
26900003	0 1 2.4	-24 58 47	0 1 2.4	-24 58 49	1.7	20.30	0.4331	90	1.12e-13	6e-17
26900002	0 1 0.2	-25 4 59	0 0 59.9	-25 5 0	4.2	21.90	0.8504	90	1.43e-13	9.07e-16
26900014	0 0 44.3	-25 7 38	0 0 44.3	-25 7 40	2.2	21.60	-1.0000	0	1.63e-14	0
26900022	0 0 36.6	-25 1 5	0 0 36.6	-25 1 6	1.0	21.20	0.5917	93	3.14e-14	1.41e-16
26900007	0 0 34.6	-25 6 19	0 0 34.6	-25 6 21	1.7	20.30	1.2343	90	1.68e-14	0
26900004	0 0 31.7	-24 54 59	0 0 31.9	-24 54 57	3.6	17.70	0.2839	90	7.96e-14	1.49e-15
26900013	0 0 30.1	-25 12 14	0 0 29.8	-25 12 17	4.9	17.50	0.1543	50	1.63e-14	-6e-18
26900001	0 0 27.7	-25 4 41	0 0 27.7	-25 4 43	1.6	19.10	0.3362	90	7.81e-14	1.65e-15
26900012	0 0 26.0	-25 6 48	0 0 26.0	-25 6 51	2.5	20.30	0.4331	90	1.70e-14	1.58e-16
26900015	0 0 22.8	-25 12 20	0 0 22.9	-25 12 22	2.2	19.70	1.6095	90	1.74e-14	0
26900009	0 0 21.2	-25 8 13	0 0 21.2	-25 8 12	1.4	20.90	0.9950	90	2.16e-14	0
26900072	0 0 13.7	-25 20 11	0 0 13.6	-25 20 13	2.1	23.00	1.3890	43	4.05e-14	0
26900016	0 0 2.8	-25 11 38	0 0 2.7	-25 11 37	1.5	21.00	1.3143	90	2.75e-14	0
15800002	0 34 19.1	-11 59 37	0 34 19.0	-11 59 39	2.3	20.20	0.8481	93	9.64e-14	0
15800012	0 34 18.5	-12 8 9	0 34 18.5	-12 8 9	0.5	18.80	0.2327	93	6.79e-14	5.79e-16
15800011	0 34 15.4	-12 8 47	0 34 15.5	-12 8 45	2.9	20.70	2.0690	90	1.84e-14	0
15800062	0 34 13.9	-11 55 60	0 34 13.8	-11 56 0	1.1	23.30	1.5680	93	4.49e-14	0
15800025	0 34 10.0	-12 11 26	0 34 9.9	-12 11 32	5.8	21.00	0.4700	43	2.56e-14	0

TABLE 2.2. **The HELLAS2XMM 2dF sample - continued**

Id	X−ray Ra	X−ray Dec	Optical RA	Optical Dec	Diff.	R	z	class	$F_{2-10keV}$	OIII
	J2000	J2000	J2000	J2000	arcsec				cgs	$erg cm^{-2} s^{-1}$
15800019	0 33 57.3	-12 0 40	0 33 57.2	-12 0 38	1.9	21.80	1.9572	90	3.12e-14	0
15800008	0 33 47.5	-12 3 25	0 33 47.5	-12 3 26	1.5	21.00	1.1509	90	2.58e-14	0
15800092	0 33 42.5	-12 1 34	0 33 42.7	-12 1 37	4.6	22.80	0.9930	43	2.65e-14	0
15800013	0 33 39.6	-12 8 26	0 33 39.6	-12 8 28	2.0	22.30	1.3260	43	1.82e-14	0
15800005	0 33 24.1	-12 6 51	0 33 24.1	-12 6 49	2.5	20.20	1.2070	90	2.35e-14	0
15800017	0 33 20.6	-12 5 39	0 33 20.6	-12 5 38	1.3	20.30	1.9460	90	2.83e-14	0
15800001	0 33 15.7	-12 6 57	0 33 15.7	-12 6 59	1.8	19.90	1.2109	90	7.29e-14	0
50900036	20 44 46.4	-10 38 40	20 44 46.7	-10 38 43	5.4	20.20	0.6941	93	3.30e-14	1.71e-15
50900001	20 44 28.7	-10 56 29	20 44 28.4	-10 56 33	5.6	23.85	1.0490	93	4.97e-14	0
50900061	20 44 20.5	-10 49 4	20 44 20.5	-10 49 3	1.6	20.36	0.3240	40	4.22e-14	-1.3e-18
50900020	20 44 19.4	-10 56 20	20 44 19.5	-10 56 19	1.6	20.16	0.7696	90	7.58e-14	0
50900067	20 44 7.1	-10 56 11	20 44 7.2	-10 56 12	1.5	22.30	1.0760	90	5.29e-14	0
50900013	20 43 49.7	-10 32 44	20 43 49.5	-10 32 40	5.0	23.20	1.2610	93	4.42e-14	0
50900031	20 43 49.2	-10 37 46	20 43 49.1	-10 37 43	3.0	20.65	0.5556	90	6.13e-14	1.32e-15
50900039	20 43 22.8	-10 40 30	20 43 22.5	-10 40 31	4.7	22.40	0.8180	90	5.19e-14	0
18350140	14 1 44.9	2 53 32	14 1 45.0	2 53 34	2.8	18.00	0.2510	40	5.13e-14	-7.6e-18
18350227	14 1 44.8	2 48 45	14 1 44.8	2 48 40	4.8	24.50	-1.0000	0	1.86e-14	0
18350069	14 1 39.6	2 57 22	14 1 39.5	2 57 21	1.5	19.10	0.2490	90	2.44e-14	7.82e-16
18350258	14 1 37.1	2 46 4	14 1 37.3	2 46 6	4.3	20.07	-1.0000	0	2.19e-14	0
18350155	14 1 32.1	2 52 22	0 0 0.0	0 0 0		-23.00	-1.0000	0	1.08e-14	0
18350262	14 1 30.8	2 45 32	14 1 30.6	2 45 31	3.1	20.93	0.7456	40	4.08e-14	-1.34e-18
18350095	14 1 27.7	2 56 7	14 1 27.7	2 56 6	0.7	19.70	0.2650	90	1.29e-14	4.34e-15
18350256	14 1 25.3	2 46 20	14 1 25.2	2 46 21	1.2	20.99	0.4332	93	2.70e-14	6.38e-16
18350279	14 1 17.5	2 43 49	14 1 17.5	2 43 51	2.1	19.60	0.3630	90	5.28e-14	1.31e-15
18350240	14 1 15.0	2 48 21	14 1 15.2	2 48 19	3.4	19.75	1.5200	90	1.52e-14	0
18350281	14 1 9.9	2 43 39	14 1 9.9	2 43 39	0.2	20.75	1.3550	90	3.64e-14	0
18350084	14 1 9.0	2 56 51	14 1 8.8	2 56 50	3.7	22.57	1.8330	90	2.07e-14	0
18350033	14 0 57.3	2 39 42	14 0 57.4	2 39 43	1.6	19.50	0.2650	40	5.01e-14	-3.6e-18
18350232	14 0 53.1	2 41 50	14 0 53.0	2 41 51	1.3	23.61	-1.0000	0	1.41e-14	0
18350034	14 0 53.1	3 1 4	14 0 53.1	3 1 6	1.3	20.18	1.3040	90	1.75e-14	0
18350048	14 0 51.1	2 59 6	14 0 51.4	2 59 5	4.1	18.99	0.2560	93	2.50e-14	2.92e-15
18350052	14 0 49.1	2 58 50	14 0 49.0	2 58 53	3.5	21.23	1.8220	90	2.05e-14	0
18350135	14 0 40.9	2 53 53	14 0 40.8	2 53 53	1.4	24.19	-1.0000	0	2.17e-14	0
18350283	14 0 38.7	2 43 22	14 0 38.6	2 43 23	1.9	20.72	0.6624	93	2.33e-14	1.65e-16
18350057	14 0 33.3	2 58 10	14 0 33.4	2 58 13	3.4	22.87	1.0260	90	2.17e-14	0
18350061	14 0 33.0	2 57 40	14 0 32.6	2 57 43	6.2	16.11	0.0000	10	1.24e-14	0

TABLE 2.2. **The HELLAS2XMM 2dF sample - continued**

Id	X−ray Ra J2000	X−ray Dec J2000	Optical RA J2000	Optical Dec J2000	Diff. arcsec	R	z	class	$F_{2-10keV}$ cgs	OIII $erg\,cm^{-2}\,s^{-1}$
18350080	14 0 19.3	2 56 38	14 0 19.1	2 56 40	4.0	22.52	1.1115	90	1.25e-14	0
13390094	13 38 7.5	24 24 12	13 38 7.5	24 24 11	0.7	18.30	0.6330	90	1.19e-13	0
13390015	13 37 12.7	24 32 51	13 37 12.8	24 32 54	3.6	19.60	-1.0000	0	3.89e-14	0
13390060	13 36 43.1	24 26 46	13 36 43.5	24 26 47	6.1	19.60	0.0000	10	3.46e-14	0
13390064	13 36 30.2	24 26 25	13 36 30.0	24 26 22	4.4	18.60	0.2540	43	2.97e-14	7.12e-16
13390085	13 37 2.2	24 24 34	13 37 2.2	24 24 36	1.7	21.15	-1.0000	0	1.56e-14	0
13390103	13 37 30.6	24 23 6	13 37 30.8	24 23 5	3.5	20.50	1.2760	90	3.19e-14	0
13390112	13 37 17.9	24 21 48	13 37 17.9	24 21 49	1.5	22.07	0.3431	93	1.72e-14	7.5e-17
13390129	13 36 49.4	24 20 4	13 36 49.3	24 20 0	3.3	20.03	-1.0000	0	3.86e-14	0
13390131	13 37 14.0	24 19 60	13 37 14.1	24 20 1	1.7	21.16	1.5510	90	1.61e-14	0
13390133	13 36 37.4	24 19 35	0 0 0.0	0 0 0		-24.20	-1.0000	0	2.85e-14	0
13390134	13 37 49.2	24 19 42	13 37 49.5	24 19 42	4.1	23.05	-1.0000	0	1.68e-14	0
13390137	13 37 24.3	24 19 22	13 37 24.5	24 19 23	2.8	23.29	-1.0000	0	1.48e-14	0
13390140	13 36 59.3	24 19 16	13 36 59.4	24 19 15	1.3	21.75	0.5011	93	2.30e-14	1.28e-16
15300065	12 56 5.6	22 7 19	12 56 5.7	22 7 19	1.8	20.07	1.1450	90	4.74e-14	0
15300067	12 56 25.6	22 7 17	12 56 25.7	22 7 20	3.3	20.55	1.7310	90	2.17e-14	0
15300142	12 57 19.2	22 0 30	12 57 19.4	22 0 32	3.4	21.07	1.5060	90	1.19e-14	0
15300143	12 57 4.3	22 0 37	12 57 4.1	22 0 40	4.3	23.44	-1.0000	0	8.32e-15	0
15300148	12 56 47.4	21 59 46	12 56 47.2	21 59 47	2.6	22.18	-1.0000	0	1.67e-14	0
15300151	12 56 2.8	21 59 52	12 56 2.7	21 59 52	1.4	19.10	-1.0000	0	1.11e-13	0
15300152	12 57 50.6	21 59 36	12 57 50.5	21 59 34	2.2	18.90	0.6150	90	2.55e-14	0
15300153	12 56 32.8	21 59 36	12 56 32.8	21 59 37	1.1	20.10	0.5160	90	3.07e-14	1.66e-16
15300176	12 57 9.0	21 58 0	12 57 8.9	21 57 57	3.1	20.79	0.9112	90	6.66e-15	9.1e-17
15300186	12 56 29.4	21 57 4	12 56 29.3	21 57 6	2.3	22.41	0.6346	90	1.27e-14	3.1e-17
15300189	12 57 32.6	21 57 8	12 57 32.7	21 57 8	0.9	19.40	-1.0000	0	1.39e-14	0
15300193	12 56 38.9	21 56 25	12 56 38.9	21 56 26	1.0	22.64	0.4703	43	1.01e-14	2.1e-17
15300203	12 57 12.2	21 55 23	12 57 12.1	21 55 22	1.6	20.78	0.8000	90	1.14e-14	4.1e-17
15300207	12 56 37.3	21 54 39	12 56 37.0	21 54 36	5.2	23.71	-1.0000	0	1.08e-14	0
15300208	12 56 50.6	21 54 58	12 56 50.6	21 54 59	0.7	20.00	0.6450	90	2.65e-14	0
15300209	12 57 6.3	21 55 6	12 57 6.2	21 55 6	1.4	22.85	1.8750	90	9.92e-15	0
15300216	12 57 15.9	21 54 32	12 57 15.7	21 54 31	2.6	19.32	0.4011	90	1.82e-14	2.31e-16
15300219	12 57 12.2	21 53 58	12 57 12.3	21 53 59	1.8	20.71	0.6854	43	1.66e-14	2.6e-17
15300222	12 56 40.3	21 53 51	12 56 40.4	21 53 51	1.5	22.53	-1.0000	0	1.17e-14	0
15300225	12 56 28.1	21 54 5	12 56 27.9	21 54 6	2.6	19.69	1.8670	90	5.58e-14	0
15300226	12 57 10.6	21 53 53	12 57 10.2	21 53 53	5.7	19.92	0.7977	90	2.06e-14	1.32e-16
15300230	12 56 50.3	21 53 29	12 56 50.5	21 53 30	3.3	18.69	0.3991	50	1.25e-14	-4e-19

TABLE 2.2. **The HELLAS2XMM 2dF sample - continued**

Id	X−ray Ra J2000	X−ray Dec J2000	Optical RA J2000	Optical Dec J2000	Diff. arcsec	R	z	class	$F_{2-10keV}$ cgs	OIII $erg cm^{-2} s^{-1}$
15300231	12 56 59.0	21 53 47	12 56 58.8	21 53 46	3.5	17.42	0.1871	93	6.06e-14	2.78e-15
15300236	12 56 54.1	21 53 18	12 56 54.1	21 53 17	1.0	20.76	0.9093	93	2.44e-14	2.58e-16
15300240	12 56 53.7	21 51 25	12 56 53.6	21 51 26	2.1	20.47	0.8940	90	5.17e-14	9.1e-17
15300253	12 56 33.1	21 51 47	12 56 33.0	21 51 49	2.5	21.36	0.7528	43	2.95e-14	0
42100102	11 5 22.5	38 11 3	11 5 22.6	38 11 5	2.1	19.96	1.2450	90	2.19e-14	0
42100058	11 5 22.0	38 14 1	11 5 22.0	38 14 2	1.1	11.30	0.0280	43	5.86e-14	4.35e-15
42100106	11 5 17.9	38 10 51	11 5 17.8	38 10 51	1.7	22.17	-1.0000	0	2.24e-14	0
42100269	11 5 12.3	38 21 29	11 5 12.8	38 21 29	5.8	19.70	-1.0000	0	4.28e-14	0
42100073	11 5 9.7	38 12 53	11 5 9.6	38 12 55	2.7	23.41	-1.0000	0	1.39e-14	0
42100302	11 4 49.2	38 18 10	11 4 49.2	38 18 11	1.7	18.30	1.9400	90	2.06e-14	0
42100197	11 4 47.6	38 4 7	11 4 47.6	38 4 7	0.6	21.30	2.2630	90	1.59e-14	0
42100039	11 4 44.2	38 14 49	11 4 43.9	38 14 48	4.3	7.60	0.0000	10	3.29e-14	0
42100243	11 4 38.2	38 25 0	11 4 38.1	38 25 1	2.0	22.45	-1.0000	0	1.63e-14	0
42100258	11 4 37.8	38 23 4	11 4 37.6	38 23 2	2.1	22.06	-1.0000	0	1.57e-14	0
42100266	11 4 35.2	38 21 39	0 0 0.0	0 0 0		-23.30	-1.0000	0	1.26e-14	0
42100207	11 4 31.5	38 3 5	0 0 0.0	0 0 0		-23.50	-1.0000	0	1.26e-14	0
42100229	11 4 24.9	38 0 24	0 0 0.0	0 0 0		-23.50	-1.0000	0	1.54e-14	0
42100189	11 4 20.8	38 4 43	11 4 20.9	38 4 37	6.1	23.34	-1.0000	0	1.28e-14	0
42100272	11 4 18.2	38 20 47	11 4 18.3	38 20 47	0.6	22.10	2.0450	90	2.66e-14	0
42100212	11 4 16.2	38 2 41	11 4 16.0	38 2 36	5.6	20.52	-1.0000	0	2.08e-14	0
42100148	11 4 14.7	38 7 14	11 4 14.8	38 7 15	0.9	22.75	-1.0000	0	5.70e-14	0
42100264	11 4 13.2	38 22 3	11 4 13.3	38 22 7	4.6	21.00	-1.0000	0	1.15e-14	0
42100237	11 4 2.8	37 59 50	11 4 3.0	37 59 50	2.2	20.52	0.2870	90	3.75e-14	6.15e-16
42100170	11 3 45.8	38 5 46	11 3 46.3	38 5 49	6.0	22.20	-1.0000	0	2.46e-14	0
42100055	11 3 43.6	38 13 49	11 3 43.6	38 13 49	0.5	22.85	-1.0000	0	2.80e-14	0
42100231	11 3 39.9	38 0 14	11 3 40.0	38 0 11	3.5	19.50	0.3070	93	3.42e-14	9.6e-16
42100011	11 3 30.2	38 16 7	11 3 30.1	38 16 6	1.7	22.75	-1.0000	0	1.35e-14	0
42100088	11 3 25.8	38 12 12	11 3 25.9	38 12 11	1.4	14.40	0.0700	93	5.68e-14	2.08e-15
42100116	11 3 22.6	38 9 45	11 3 22.8	38 9 45	1.6	21.85	-1.0000	0	2.46e-14	0
42100025	11 3 18.6	38 15 45	11 3 18.4	38 15 44	2.6	18.98	0.3140	90	6.87e-14	1.54e-15
42100066	11 3 17.1	38 13 36	11 3 17.3	38 13 34	2.8	22.71	1.2450	90	3.66e-14	0
16274019	0 50 19.4	-51 55 32	0 50 19.5	-51 55 30	1.6	21.60	-1.0000	0	2.50e-14	0
16274055	0 50 26.3	-51 59 29	0 50 26.3	-51 59 30	1.3	22.30	-1.0000	0	1.89e-14	0
16274057	0 50 9.4	-51 59 33	0 50 9.7	-51 59 32	2.8	20.05	-1.0000	0	4.38e-14	0
16274066	0 50 30.6	-52 0 11	0 50 30.8	-52 0 10	1.9	18.78	0.4630	90	1.35e-13	1.93e-15
16274069	0 50 30.7	-52 0 46	0 50 30.9	-52 0 48	2.4	24.08	1.3500	43	2.62e-14	0

TABLE 2.2. **The HELLAS2XMM 2dF sample - continued**

Id	X−ray Ra J2000	X−ray Dec J2000	Optical RA J2000	Optical Dec J2000	Diff. arcsec	R	z	class	$F_{2-10keV}$ cgs	OIII $erg\,cm^{-2}\,s^{-1}$
16274078	0 50 43.4	-52 1 16	0 50 43.7	-52 1 17	3.1	21.18	-1.0000	0	2.02e-14	0
16274097	0 51 26.5	-52 2 20	0 51 26.2	-52 2 21	3.0	20.20	-1.0000	0	4.02e-14	0
16274117	0 50 8.4	-52 3 50	0 0 0.0	0 0 0		-22.50	-1.0000	0	9.56e-15	0
16274158	0 49 53.1	-52 5 25	0 49 52.9	-52 5 24	1.9	21.65	-1.0000	0	9.49e-15	0
16274181	0 50 31.6	-52 6 30	0 50 31.5	-52 6 34	4.1	24.04	-1.0000	0	1.63e-14	0
16274197	0 50 17.1	-52 7 15	0 50 17.4	-52 7 18	4.5	23.40	-1.0000	0	7.07e-15	0
16274212	0 50 44.7	-52 7 35	0 50 44.7	-52 7 36	0.9	19.84	-1.0000	0	1.02e-14	0
16274235	0 50 12.3	-52 8 34	0 50 12.3	-52 8 36	2.2	22.28	-1.0000	0	6.07e-15	0
16274292	0 49 59.0	-52 11 12	0 49 59.0	-52 11 10	1.4	21.26	-1.0000	0	1.05e-14	0
16274307	0 49 55.7	-52 12 31	0 0 0.0	0 0 0		-22.50	-1.0000	0	7.65e-15	0
16274314	0 49 47.6	-52 12 49	0 49 47.8	-52 12 48	1.9	21.04	1.1060	90	2.66e-14	0
16274320	0 49 36.7	-52 13 6	0 49 36.7	-52 13 7	0.3	20.31	0.9290	90	9.63e-15	0
16274339	0 49 50.9	-52 14 10	0 49 51.1	-52 14 13	2.9	22.30	-1.0000	0	2.22e-14	0
16274340	0 49 59.4	-52 14 12	0 49 59.2	-52 14 11	1.9	21.70	-1.0000	0	1.40e-14	0
16274349	0 49 35.2	-52 14 58	0 49 35.9	-52 14 56	6.7	20.42	-1.0000	0	1.11e-14	0
16274351	0 50 7.4	-52 15 8	0 50 7.4	-52 15 8	0.6	19.43	2.4100	90	1.41e-14	0
16274363	0 50 32.1	-52 15 43	0 50 32.2	-52 15 43	0.5	19.77	1.2200	90	6.41e-14	0

Chapter 3

The Luminosity Function

The measure of the evolution of the density of active galactic nuclei (AGN) is a key issue in order to trace the history of the accretion in the Universe and thus to understand the physics of the formation of both massive black holes and of the galaxies which are their hosts.

Until few years ago the best measures of the cosmological evolution of the luminosity function of AGN were essentially limited to optical broad emission line AGN (AGN1) selected in the optical and/or soft X-rays, Fig. 3.1, indicating, for them, strong evolution (see e.g. La Franca and Cristiani 1997, Croom et al. 2004, Miyaji et al. 2000, 2001).

On the contrary, the evolution of the density of the highly obscured AGN was basically unknown, and it was only possible to depict probable scenarios taking into account the evidences that in the local Universe there is a population of X-ray absorbed AGN which are about four times more numerous than unabsorbed ones (e.g. Risaliti et al. 1999 and references therein). Indeed synthesis models of the XRB demand for the existence of an obscured population of AGN evolving with cosmic time like the unobscured one (see e.g. Setti and Woltjer 1989, Comastri et al. 1995, Pompilio et al. 2000).

The difficulty in selecting absorbed AGNs is due to the fact that these AGNs are fainter than unabsorbed one in the optical (because the optical light is dominated by the host galaxy) and in the soft X-ray bands (because of the absorption due to

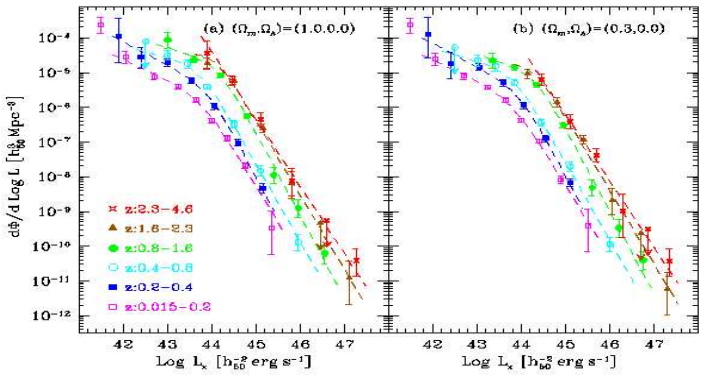

FIGURE 3.1. The binned SXLFs estimated by Miyaji et al. 2001. The symbol attached to a downward arrow indicates the 90% upper limit (corresponding to 2.3 objects) for the bin with no AGN in the sample. The best–fit analytical model for each redshift bin in the luminosity range used for the fit is overplotted in dashed lines.

N_H column densities larger that 10^{21-22} cm^{-2}).

Thanks to the advent of the new generation of hard X-ray (2-10 keV) missions (XMM-*Newton* and Chandra), with their high sensitivity and spatial resolution of the order of few arcsecs, it has become possible to conceive surveys dedicated to the creation of more complete samples of AGN, less biased against X-ray absorbed objects and whose optical identification is less ambiguous.

Unfortunately, however, already at fluxes fainter than $F_{2-10}\sim10^{-14}$ $erg\,cm^{-2}\,s^{-1}$, a significant fraction of the X-ray sources have optical magnitudes fainter than the spectroscopic limit of the existing 8-m class optical telescopes and, thus, the measure of the redshift in many cases relys on photometric redshift tecniques or even be impossible.

To study the evolution of the HXLF of AGN we have utilized two different approaches, reported in Fiore et al. 2003 and La Franca et al. in preparation, fully exploiting HELLAS2XMM sample together with the data from other deep surveys.

3.1 Samples

In order to cover the widest possible range of luminosities and redshifts we combined the data from the full HELLAS2XMM sample with other existing flux limited samples.

The fluxes and area covered by a number of hard X-ray surveys are compared in

Fig. 3.2 and in Fig. 3.3 the samples used in the following.

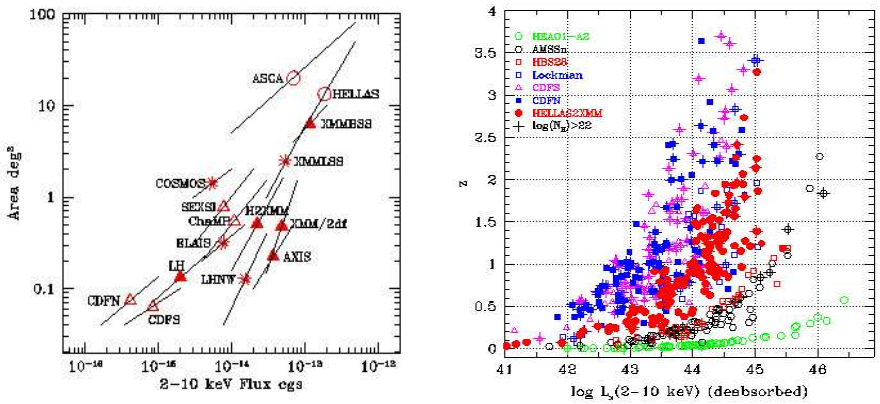

FIGURE 3.2. Left: The flux-area diagram for several 2-10 keV surveys. Right: The 210 keV luminosity as a function of the redshift for the sources in the combined sample.

Sample	Tot. Area deg^2	Flux limit 10^{-15} cgs	# sour.	% z-spec	refs	symbol
HELLAS2XMM	1.6	8.0	231	66%	1,2	open circ.
CDFN faint[a]	0.0369	1.0	88	59%	3,4	filled squar.
CDFN bright[b]	0.0504	3.0	44	65%	3,4	filled squar.
CDFS faint[a]	0.0369	1.0	68	62%	5,6	stars
CDFS bright[b]	0.0504	3.0	55	58%	5,6	stars
Lockman Hole[c]	0.126	4.0	55	75%	7	filled triang.
SSA13[d]	0.0177	3.8	20	65%	8	filled circ.
Total			561	65%		

FIGURE 3.3. Note:(a) Inner 6.5 arcmin radius; (b) outer 6.510 arcmin annulus; (c) inner 12 arcmin radius; (d) inner 4.5 arcmin radius; (1) Fiore et al. 2003; (2) Cocchia et al. in prep.; (3) Alexander et al. 2003; (4) Barger et al. 2003; (5) Giacconi et al. 2002; (6) Szokoly et al. 2004; (7) Mainieri et al. 2002; (8) Barger et al. 2001.

The sample from these additional fields consists of 310 hard X-ray selected sources.

Classification of the optical spectra from the additional samples are adopted from the above publications, when available. Otherwise, we produced a tentative classification by visual inspection of the published optical spectra (Barger et al. 2001, 2002), adopting the criteria in Sect. 2.7.

The combined sample consists of about 500 AGN at fluxes $S_{2--10} >\sim 10^{-16}$.

3.2 The non–parameric approach

We used the classical $1/V_{max}$ (Schmidt 1968; Lilly et al. 1995; Cowie et al. 2003) method to estimate number and luminosity densities of hard X–ray selected sources in the full sample described in the next section.
To use this method we made the following key assumption: we are sampling *all* the sources in the sky at our flux limit.
Making this assumption we, basically, do not take into account two possible causes of incompleteness, such as:

- N_H distribution: strong obscuration, $N_H > 10^{23}$, makes difficult the detection of sources even in the $2 - 10$ keV X–ray band.
- spectroscopic incompleteness: many optical counterparts of hard X–ray sources are too faint for spectroscopy, even for the modern 8–10m ground telescopes.

Thanks to the spectroscopic identifications in the HELLAS2XMM survey we can take into account the latter point, correcting, at least partially, for spectroscopic incompleteness in a statistical way. In the following section I will report the guidelines of the procedure adopted, further details can be found in Fiore et al. 2003.

3.2.1 Statistical predictions for the unidentified sources

As already mentioned, thanks to the optical spectroscopic identification of the HELLAS2XMM sample, we found a striking correlation between X/O and the $2 - 10$ keV luminosity for the sources with the nucleus strongly obscured in the optical band.
Figure 3.4 show the X–ray to optical flux ratio as a function of the X–ray luminosity for broad line AGN (left panel) and non broad line AGN and galaxies (right panel).

The average X/O for the broad line AGN of the combined sample is 1.2 with a standard deviation of 0.3.
The right panel of Fig. 3.4 shows the X–ray to optical flux ratio as a function of the X-ray luminosity for optically obscured AGN. There is here a remarkable correlation between X/O and L_{2-10}: higher luminosity AGN tend to have higher X/O. The solid diagonal line in the panel represents the best linear regression between log (X/O) and log L_{2-10}.

All objects plotted in the right panel do not show broad emission lines, i.e. the nuclear optical–UV light is completely blocked, or strongly reduced in these objects, unlike the X–ray light. Indeed, the optical R band light of these objects is dominated by the host galaxy and therefore, X/O is roughly a ratio between the nuclear

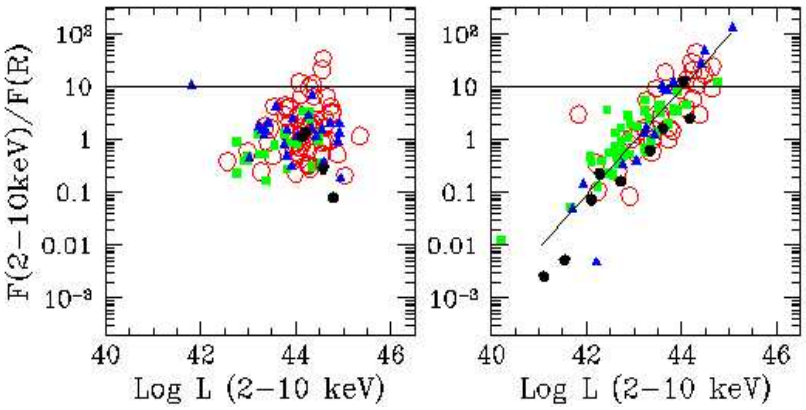

FIGURE 3.4. The X-ray to optical flux ratio as a function of the X-ray luminosity for type 1 AGN, left panel and non type 1 AGN and galaxies (right panels). HELAS2XMM = open circles; CDFN = filled squares; LH = filled triangles; SSA13 = filled circles. The orizontal lines mark the level of $X/O = 10$, 20% of the sources in the combined sample have X/O higher than this value. The diagonal line in the right panel is the best linear regression between log (X/O) and log L_{2-10}. Fiore et al. 2003.

X–ray flux and the host galaxy starlight flux. While the X–ray luminosity of these objects spans about 4 decades, the host galaxy R band luminosity has a moderate scatter, less than one decade, around the mean value of 10^{11} $L_\star$, rather independent of redshift.

We can use the correlation in Fig. 3.4 and the fractions of obscured to unobscured objects in Table 3.2.1 to predict the luminosities, and therefore the redshifts, of the sources in the combined sample without optical spectroscopic identification.

TABLE 3.1. **Number of sources per bins of flux and X/O ratio**

$F_{2-10} < 10^{-14}$ $erg\,cm^{-2}\,s^{-1}$				$F_{2-10} > 10^{-14}$ $erg\,cm^{-2}\,s^{-1}$		
X/O	Tot.	Id.	compl.	Tot.	Id.	compl.
>10	22	1	5%	43	19	44%
3-10	29	7	24%	36	30	83%
0.1-3	72	54	75%	97	94	97%

TABLE 3.2. **Ratio of optically obscured to optically unobscured AGN.**

X/O	$F_{2-10} < 10^{-14}\ erg\,cm^{-2}\,s^{-1}$	$F_{2-10} > 10^{-14}\ erg\,cm^{-2}\,s^{-1}$
>10	-	$3.8^{+3.2}_{-2.0}$
3-10	$2.5^{+3.7}_{-2.0}$	$1.1^{+0.5}_{-0.4}$
0.1-3	$1.21^{+0.36}_{-0.3}$	$0.31^{+0.09}_{-0.07}$

The procedure is as follows: the sources without redshifts are divided in the same bins of X/O and fluxes as in Tables 3.2.1, 3.2.1 (the few lower limits on X/O have been conservatively considered as measurements); next they are picked randomly according to the ratios in Table 3 to belong either to one or the other class.
For the lower flux, $X/O > 10$ bin, for which we do not have information, we use the same ratio as in the $X/O > 10$, higher flux bin. For those falling among the optically obscured AGN we associate to each source a luminosity according to its X/O value and the linear regression drawn in Fig. 3.4 right panel.
For those falling among the optically unobscured sources we associate to each source a luminosity choosen at random from a distribution similar to that of the broad line AGN in Fig. 3.4 left panel.
From the luminosities we derive redshifts, using the same K correction and cosmology as for the sources with spectroscopic (or photometric) redshift identifications.
Because the number of objects with measured redshift in the bins with $X/O > 3$ is relatively small and therefore the errors on the ratio between obscured and unobscured objects are large, we tested several different values within the error interval. The spread introduced in the redshift and luminosity distributions by these uncertainty is smaller than 10%.

The z distribution of the sources in the combined sample and the z distribution of the 132 sources in the combined sample with $F_{2-10} < 10^{-14}\ erg\,cm^{-2}\,s^{-1}$ are plotted in Fig. 3.5.
The histograms of the sources with measured redshift in Fig. 3.5 show a sharp decrease at $z = 1.2$ (similar results are presented also by Franceschini et al. 2002; Hasinger 2003).

When the sources with an estimated redshift are added, the peak of the redshift

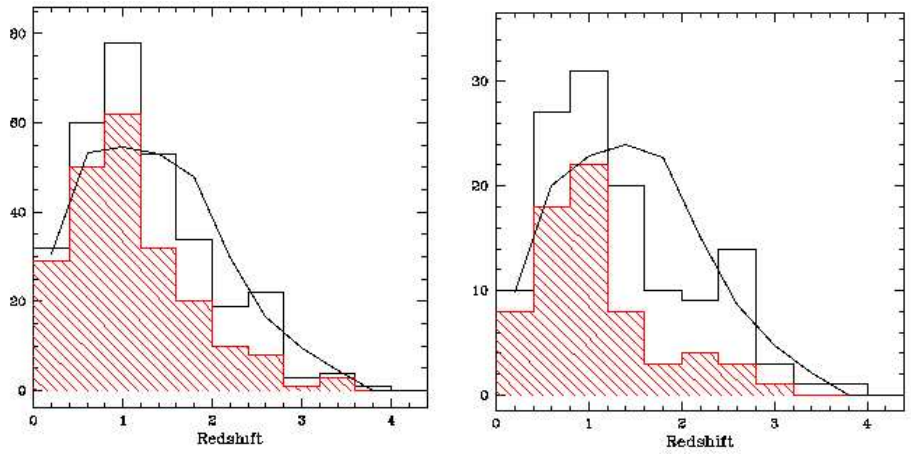

FIGURE 3.5. The z distribution of the sources in the combined sample (left) and of the 132 sources with $F_{2-10} < 10^{-14}\ erg\,cm^{-2}\,s^{-1}$ (right). Shaded histogram = distribution of the spectroscopically identified sources (70% (left) and 53% (right) of the sample). Solid histogram = full sample. The luminosity and the redshift of the sources without a spectroscopic redshift have been estimated using the correlation in Fig. 3.4, The black thick line represents the expectation of the AGN synthesis models of the CXB (Comastri et al. 2001), where unobscured and obscured AGN follow the same pure luminosity evolution. Fiore et al. 2003

distribution at $z \sim 1$ is confirmed, but the decrease above this redshift is less sharp, thus suggesting that this feature in the distribution of the sources with spectroscopic redshift is enhanced by the incompleteness of the optical identification, in particular at high X/O values.

3.2.2 Results

We have used the combined sample of hard X-ray selected sources, plus 66 sources from the HEAO1 A2 all sky survey (Grossan 1992) with $F_{2-10} < 2{\times}10^{-11}\ erg\ cm^{-2}\ s^{-1}$ to compute the evolution of the number density and of the X–ray luminosity density. We have adopted the standard $1/V_{max}$ method (Schmidt 1968; Lilly et al. 1995; Cowie et al. 2003).

We have computed the evolution of both the number density of hard X–ray sources and of the 210 keV luminosity density in three bins of luminosities:
$43 < logL_{(2-10)} < 44$,
$44 < logL_{(2-10)} < 44.5$,
$44.5 < logL_{(2-10)} < 46$.

Figure 3.6 plots the evolution of the number density for these three luminosity

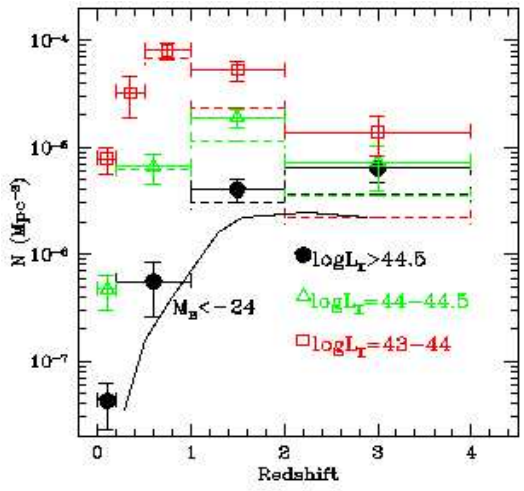

FIGURE 3.6. The evolution of the number density of hard X–ray selected sources in three bins of luminosity: $\log L_{2-10} = 43 - 44\ erg\,s^{-1}$ = empty squares; $\log L_{(2-10)} = 44 - 44.5\ erg\,s^{-1}$= empty triangles; $\log L_{2-10} > 44.5\ erg\,s^{-1}$ = filled circles.
Dashed lines represent lower limits obtained using only the sources with measured redshift. The solid continuous curve represents the evolution of optically selected QSO more luminous than $M_B = -24$. Note as the shape of the solid curve is similar to the evolution of the luminous X-ray selected sources. Fiore et al. 2003

bins.
We emphasize that the value for the z= 2 − 4, log $L_{(2-10)} = 43 - 44$ bin is actually a lower limit, because at our flux limit the objects with log $L_{(2-10)} < 43.5$ are not accessible at z > 2.
In addition, if only the sources with a measured z are considered, we obtain the lower limits plotted as dashed lines.
We see that the number density of lower luminosity AGN increases between z = 0 and z= 0.5 by a factor 13. It stays constant up to z ∼ 2, while at higher z we cannot obtain a reliable estimate of the number density for the reason explained above. Conversely, the number density of luminous AGN increases by a factor 100 up to z= 2 and by a factor 170 up to z ∼ 3. The last behaviour is similar to that of luminous ($M_B < -24$) optically selected AGN (Hartwick and Schade 1990, solid thick line in Fig. 3.6. The different evolution of low and high luminosity sources is confirmed if we consider the sample of the identified sources only.

Figure 3.7 plots the evolution of the hard X–ray luminosity density.
We see that the luminosity density of lower luminosity AGN increases from z= 0 to z ∼ 1.5 by a factor of 18, while that of high luminosity AGN increases up to z = 2

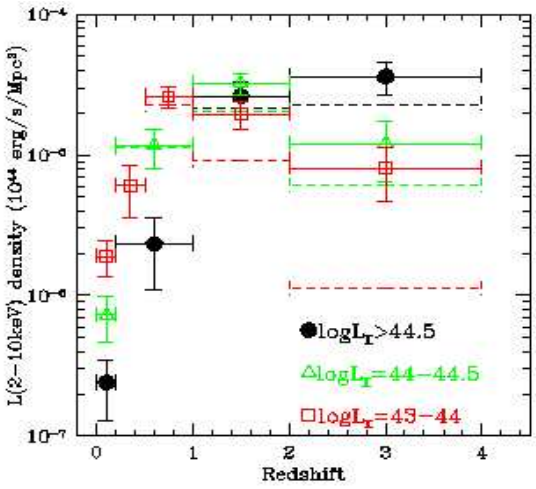

FIGURE 3.7. The evolution of the luminosity density of hard X–ray selected sources in the same bins of luminosity of Fig. 3.6.
Dashed lines represent lower limits obtained using only the sources with measured redshift. Fiore et al. 2003

by a factor 100 and up to z $\sim$ 3 by a factor 170.

The luminosity density at z $<$ 1 is dominated by low luminosity AGN, while (within the large statistical error bars and the uncertainty associated with the assumptions made in assigning a redshift when not directly available) at z $>$ 1 those of low and high luminosity AGN are comparable, and similar to that of low luminosity AGN at z $= 0.5 - 1$.

3.3 The parametric approach

The parametric approach aims to overcome the limits of the non–parametric one and to analitically take into account all the possible incompleteness causes.
In the following I describe the guidelines of the procedure that will be reported in La Franca et al. in preparation.

3.3.1 The shape of the Luminosity Function

We searched for a functional fit to the density of AGN as a function of the unabsorbed 2-10 keV luminosity (L_X), the absorbing column density (N_H), and the redshift (z).
The method is based on the comparison trough χ^2 estimators of the observed and expected number of AGN and N_H distributions, obtained from simulations which

take into account all the observational selection effects of the used samples.

We used standard functional forms, such as the pure luminosity evolution (PLE) model and a luminosity dependent density evolution (LDDE) model, in order to describe the evolution of AGNs. The hard X-ray luminosity function (HXLF), representing the number density per unit comoving volume per Log L_X as a function of L_X and z, is expressed as

$$\frac{\mathrm{d}\Phi(L_\mathrm{X}, z)}{\mathrm{dLog}L_\mathrm{X}}.$$

We adopted a smoothly-connected two power-law form to describe the present-day HXLF,

$$\frac{\mathrm{d}\Phi(L_\mathrm{X}, z=0)}{\mathrm{dLog}L_\mathrm{X}} = A[(L_\mathrm{X}/L_*)^{\gamma 1} + (L_\mathrm{X}/L_*)^{\gamma 2}]^{-1}. \quad (3.1)$$

Once assumed a HXLF evolution model, the number of total expected AGNs in a certain bin of the $L_X - z - N_H$ space is the result of the sum, over the number of samples N_{samp}, of the expected number of AGN in each sample taking into account the area coverage of each ith sample $\Omega_i(L, N_H, z)$, the N_H distribution $f(L_\mathrm{X}, z; N_\mathrm{H})$, and the completeness function $g_i(L_\mathrm{X}, z, N_H)$:

$$E = \sum_{i=1}^{N_\mathrm{samp}} \int\int\int \frac{\mathrm{d}\Phi(L_\mathrm{X}, z)}{\mathrm{dLog}L_\mathrm{X}} f(L_\mathrm{X}, z; N_\mathrm{H}) g_i(L_\mathrm{X}, z, N_H) \times \Omega_i(L, N_H, z) \frac{dV}{dz} \mathrm{dLog}L_\mathrm{X} \mathrm{d}z \mathrm{d}N_H.$$

3.3.2 Correction for spectroscopic incompleteness: the completeness function

As all the faint samples used in our analysis (HELLAS2XMM, Lockmann, HDF-S, HDF-N) are spectroscopically complete up to a certain optical limit magnitude ($R\sim23$), we introduced the *completeness function* $g(L_\mathrm{X}, z, N_H)$ which provides the probability that a given object with luminosity L_X, redshift z and a certain N_H, had an apparent R-band magnitude brighter than the spectroscopic limits of each sample.
For this reason we derived an empirical relationship between unabsorbed L_X and optical luminosity L_R[a] for AGN1 and AGN2 (see Fig. 3.8).

[a]The L_R luminosity used is monochromatic and corresponds to $\log L_\mathrm{R} = -0.4 \times (M_\mathrm{R} - 51.326)$ where the flux is $f = 2.84 \times 10^{-20} \times 10^{-0.4R}$ [erg/s/Hz] according to Zombeck (1990).

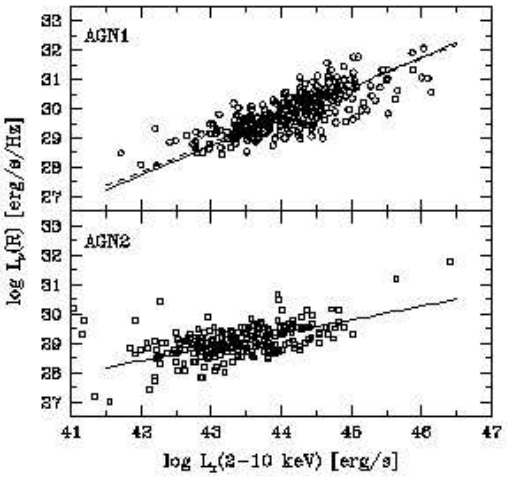

FIGURE 3.8. LogL_X – Log L_R relation for optical AGN1 and AGN2. The continuous lines correspond to eq. 2 and 3. La Franca et al. in prep.

For AGN1 we found:

$$\mathrm{Log}L_{\mathrm{R}}[\mathrm{erg/s/Hz}] = \mathrm{Log}L_{\mathrm{X}}[\mathrm{erg/s}] - 14.25, \tag{3.2}$$

with a 1σ spread of 0.48. While for AGN2 a flatter relation was found:

$$\mathrm{Log}L_{\mathrm{R}}[\mathrm{erg/s/Hz}] = 0.46 \times \mathrm{Log}L_{\mathrm{X}}[\mathrm{erg/s}] - 9.02, \tag{3.3}$$

with a 1σ spread of 0.40. The two different relations should be attributed to the dominance in the optical of the AGN component in the AGN1, which produces an almost linear relationship among X-ray and optical luminosity. At variance in type 2 objects were the AGN is obscured in the optical, the optical luminosity is dominated by the hosting galaxy.

In order to use the above L_X–L_R relationships we need also to know the probability of an AGN to appear as an optical type 1 or type 2 object as a function of L_X, N_H and z.
These probabilities were estimated from the sample itself. After several analyses, we assumed that the distributions of the observed absorption column-densities N_{H0} for AGN1 and AGN2 as a function of L_X and z are almost constant with the redshift (see Fig. 3.9).

We have thus divided the sample into two sub-samples: a) the objects having log (N_{H0})>21.5 which are mostly AGN2, and the objects having log (N_{H0})≤21.5 which are mostly AGN1.

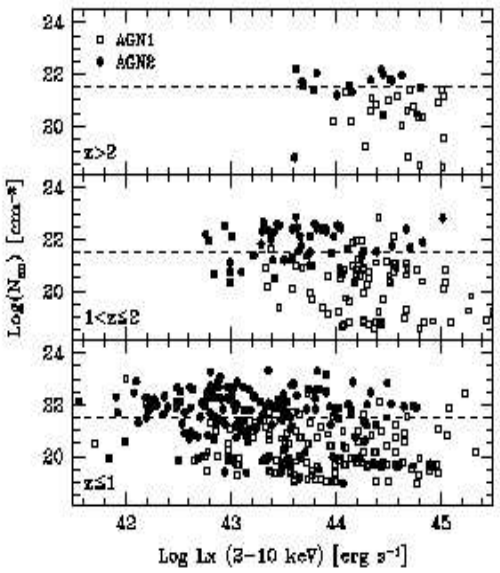

FIGURE 3.9. Log L_X - Log N_{H0} plane at $z \leq 1$ (*bottom*), $1 < z \leq 2$ (*middle*), $z > 2$ (*up*). Open squares are optical AGN1, filled circles are optical AGN2.

The observed constant distribution of N_{H0} with redshift implies that the N_H distribution shift towards higher values with increasing redshift as the intrinsic and observed absorption column-densities are related by the equation $log(N_H) = log(N_{H0}) + 2.42 \times log(1+z)$.
In both sub-samples the probability to find an AGN1 increases with increasing luminosities (see Figure 3.10), and, at variance with what usually expected, there is a relevant fraction of low luminosity (log L_X <43) not absorbed objects which are AGN2, while about 40% of the high luminosity (log L_X >45) absorbed objects are AGN1.

In summary, for each simulated object having luminosity L_X, redshift z, and absorption column-density N_H :

a) the N_{H0} was computed according to the equation $log(N_{H0}) = log(N_H) - 2.42 \times log(1+z)$,

b) the probabilities to be an AGN1 or AGN2 were computed according to the values estimated from the sample itself, values plotted in Fig. 3.10

c) the probabilities to be observed in each sample were computed according to the relations in Fig. 3.8 and summed in order to obtain the total value of the

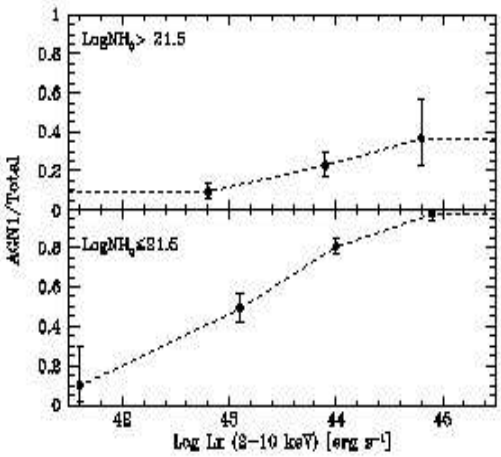

FIGURE 3.10. Fraction of optical type 1 AGN with log $N_{H0} > 21.5$ (*up*), and log $N_{H0} \leq 21.5$ (*bottom*) as function of the intrinsic luminosity L_X.

completeness function $g_i(L_X, z, N_H)$.

3.3.3 The N_H function

To describe the distribution of spectral parameters of AGNs at a given luminosity and redshift, we introduce the N_H function, $f(L_{\rm X}, z; N_{\rm H})$, a probability-distribution function for the absorption column-density as a function of L_X and z.
The N_H function has a unit of (Log N_H)$^{-1}$ and is normalized to unity at each redshift, over the N_H interval 20<LogN_H<25:

$$\int_{20}^{25} f(L_{\rm X}, z; N_{\rm H}) {\rm dLog}N_{\rm H} = 1.$$

The objects have been grouped into 5 bins of N_H wide Log $N_H = 1$, and centered at Log N_H = 20.5, 21.5, 22.5, 23.5, 24.5 cm^{-2}. As a matter of fact, the first bin collects all the AGNs having Log $N_H < 21.0$ cm^{-2}.
We assumed a flat N_H distribution between Log $N_H = 21$ and Log $N_H = 26$ while allowing to vary the fraction of objects with Log $N_H < 21.0$ cm^{-2}. This choice is, in our opinion, the simplest possible according to the uncertainties in the N_H measurements, and the observed distribution of the data.

See Fig. 3.11 where the assumed, expected and observed NH distributions, in different redshift luminosity intervals, are shown. The distribution of the less observed objects with higher column densities is consistent with a flat N_H distribution between Log $N_H = 21$ and Log $N_H = 26$ when the selection effects are taken into

account. As no object with Log $N_H > 25$ are either expected and observed, we limited our analysis of the evolution of the AGN to the objects having Log $N_H \leq 25$.

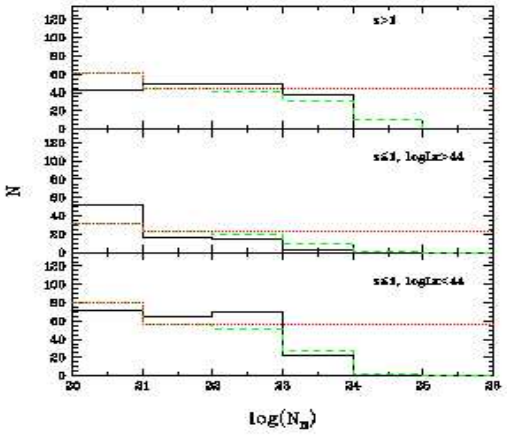

FIGURE 3.11. N_H distributions in various luminosity/redshift intervals. The continuous lines are the observed distributions, the red dotted lines are the assumed N_H distributions (constant N_H distribution with a LDDE HXLF evolution), while the green dashed line are the expectations taking into account the selection effects.

The fraction of objects in the N_H distribution with $25 <$ Log $N_H \leq 26$ was assumed equal to the fraction of objects with $24 <$ Log $N_H < 25$, and kept in the simulations of the N_H distributions for the sake of completeness.
The fraction of objects with Log $N_H < 21.0$ cm^{-2} seems to vary: to increase at larger L_X and to decrease at larger redshifts. In order to reproduce this behaviour of the N_H function, we introduced a linear dependence on the N_H distribution as a function of Log L_X and z (further details in La Franca et al. in preparation).
Note that the parametric approach allows us to include in the analysis the more obscured objects ($23 < Log(N_H) < 24$, compare the green dashed line and the continuous one respectively), highlighting the incompleteness of observed samples and the limits of studying evolution of number and luminosity densities of AGNs using non parametric methods.

3.4 The models

3.4.1 The LDDE model

As a first step we adopted a LDDE model.
By introducing the evolution factor

$$e(z) = \begin{cases} (1+z)^{p1} & (z < z_{\rm c}) \\ e(z_{\rm c})[(1+z)/(1+z_{\rm c})]^{p2} & (z \geq z_{\rm c}), \end{cases} \tag{3.4}$$

the pure density evolution (PDE) model is expressed as

$$\frac{{\rm d}\Phi(L_{\rm X}, z)}{{\rm dLog}L_{\rm X}} = \frac{{\rm d}\Phi(L_{\rm X}, 0)}{{\rm dLog}L_{\rm X}} e(z), \tag{3.5}$$

where $e(z)$ is the evolution factor as expressed in eq. 3.7.

The $z_{\rm c}$ parameter represents the maximum redshift above which the evolution stops. $p1$ is the parameter of the speed of the evolution, while $p2$ is usually negative and provides the speed of the de-evolution of the HXLF at $z{>}z_c$.

The LDDE model is obtained by introducing in the PDE model a luminosity dependence on $z_{\rm c}$, where $z_{\rm c}$ is expressed by a power law of $\rm L_X$:

$$z_{\rm c}(L_{\rm X}) = \begin{cases} z_{\rm c}^* & (L_{\rm X} \geq L_a) \\ z_{\rm c}^* (L_{\rm X}/L_a)^{\alpha} & (L_{\rm X} < L_a). \end{cases} \tag{3.6}$$

The above parameterization has been introduced by Ueda et al. 2003 in order to allow for a change with luminosity of the redshift at which the density of AGNs peaks. This behaviour is also apparent in our compilation of data, as it is possible to see, for example, in Figure 3.12.

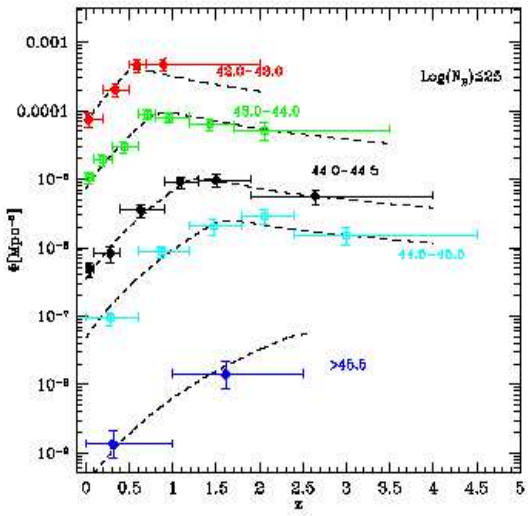

FIGURE 3.12. Density of AGN in luminosity bins as a function of redshift. The dashed lines are the best fit values of the LDDE model with a evolving N_H distribution. The attached errors are estimated from Poissonian errors (1σ) in the observed number of sources according to the formula of Gehrels (1986).

3.4.2 PLE model

We also checked if a simpler pure luminosity evolution model was consistent with the data. By introducing the evolution factor

$$e(z) = \begin{cases} (1+z)^{p1} & (z \leq z_c) \\ e(z_c) & (z > z_c), \end{cases} \tag{3.7}$$

the PLE model is expressed as

$$\frac{\mathrm{d}\Phi(L_X, z)}{\mathrm{dLog}L_X} = \frac{\mathrm{d}\Phi(L_X/e(z), 0)}{\mathrm{dLog}L_X}. \tag{3.8}$$

The PLE fit provides a less probable solution for the HXLF, while the data (obviously) still need a N_H distribution where both a dependence on redshift and luminosity similar to what found in the LDDE model is allowed (see Fig. 3.13 The PLE fit finds that the evolution stops at z_c=1.14.
This is value is smaller than previously estimated from the evolution of the HXLF of AGN1. La Franca et al. 2002 found z_c=2.4, with 1σ uncertainties of about 0.5.

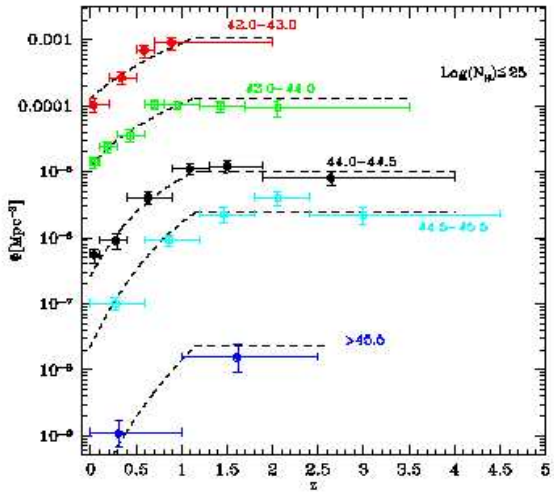

FIGURE 3.13. Density of AGN in luminosity bins as a function of redshift. The dashed lines are the best fit values of the PLE model with a evolving N_H distribution.

As expected (see Figure 3.13) the PLE model does not give rise to a change with luminosity of the redshift of the peak of the density of AGN, which, instead the data seems to show but, from a statistical point of view we cannot discard the PLE model but the LDDE is more probable.

3.4.3 Results

This analysis uses a new method in order to correct for the spectroscopic incompleteness of the faint samples, and takes into account all the selection effects due to X-ray absorption. In this way we have been able to use a deep and large sample of AGN.

We found that the evolution of the HXLF is best described by a LDDE model up to z= 4.5. This result is in agreement with the previous estimates of Cowie et al. 2003, Fiore et al. 2003 and Hasinger 2003 who found that the AGN number density for luminosities lower than 10^{44} peaks at lower redshifts than those of higher luminosities. However, the results are not able to rule out a PLE model.

We also found that the fraction of absorbed AGN increases with the decrease of the intrinsic luminosity of AGN and with the increase of the redshift. This increase of the fraction of absorbed AGN with the redshift is the most important result of this analysis.
In this respect, according to our results, it should be noted that a dependence of the fraction of absorbed AGN disappears when one flux limited sample only is analyzed. In this case, as a flux limited sample selects faint low redshift AGNs (usually more absorbed) and bright high redshift AGN (more absorbed as well !), it results that the measured fraction of absorbed AGN is higher than average, and roughly constant. Only trough the analysis of a compilation of several samples, which are able to cover wide strips of the L_X - z plane with almost constant redshift or luminosity, it is possible to disentangle the true dependencies.

3.5 Comparison with theoretical models

The study of the luminosity function of AGNs helps us to understand their evolution with cosmic time, but it is of fundamental importance to incorporate the formation and evolution of these sources into the wider scenario of formation and evolution of structure in the Universe.
Strong evidences witness the tight links and feedbacks between super-massive black holes (SMBHs), nuclear activity and galaxy evolution.
For this reason in the past years there have been several attempts aimed at linking the evolution of the galaxies in the hierarchical clustering scenarios with the changing accretion rates of cold gas onto the central SMBH that power the QSOs.
A first attempt to constrain models for the formation and evolution of structure in

the Universe using the evolving optical and X-ray LFs have been presented by Menci et al. 2003, 2004.
Key ingredients in the models by Menci et al. are the prescriptions from Cavaliere and Vittorini 2000: during encounters, and not only major mergers, among galaxies part of the available galactic cold gas is destabilized and funnelled toward the centre where, for the most (3/4), it feeds the nuclear starburst and, the remaining (1/4), the central BHs.

In Fig. 3.14 we compare theoretical predictions from the semi–analytic model of galaxy formation by Menci et al. 2004, incorporating the description of the X-ray properties of AGNs, and data from the HELLAS2XMM survey together with the samples described above.

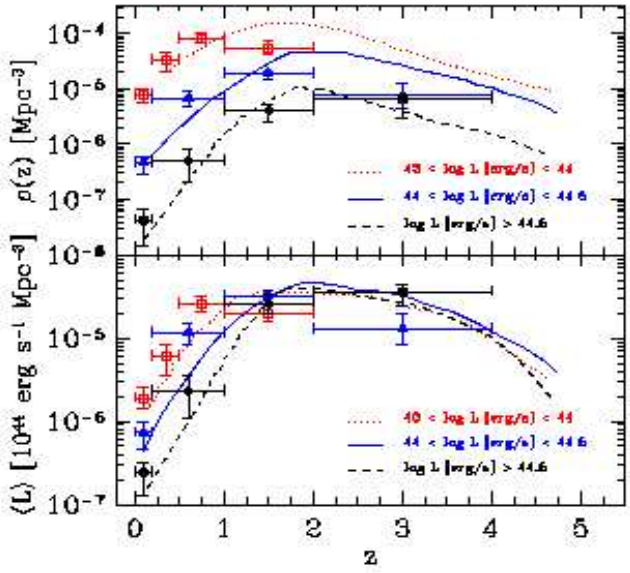

FIGURE 3.14. Top: The evolution of the number density of X–ray AGNs in three bins of luminosity (cgs, in the band $2-10$ keV): $43 < logL_X < 44$ (dotted line), $44 < logL_X < 44.5$ (solide line), $44.5 < logL_X$ (dashed line). The data are from Fiore et al. 2003. Bottom: The evolution of the X–ray luminosity density for the same luminosity bins. Menci et al. 2004.

All the predicted densities drop substantially from z $\sim$ 2 to the present.
The agreement with the data is excellent for the highest luminosity bin, not surprisingly since such objects are also sampled in the optical band, where the model was already successfully tested in Menci et al. 2003. In addition, as already mentioned in

Sect. 3.2.2 we find a nice agreement between data for high luminosity sources and the evolution of optically selected AGNs with $M_B < -24$ estimated by Hartwick and Schade 1990 (Fig. 3.6).
At lower luminosities, the decline for $z < 1-2$ is less pronounced in the predictions as well as in the observations.

In the former, this is due to the larger quantity of galactic cold gas left available for accretion in the less massive galaxies.
This is a natural feature in hierachical scenarios, since more massive potential wells originate from clumps collapsed earlier in biased regions of the primordial perturbation field; the higher densities then prevailing allowed for earlier condensation and hence enhanced star formation at high redshifts. Thus, at low z a larger fraction of cold gas will have already been converted into stars, and both star formation and BH accretion are considerably suppressed.
We note though that the decrease of the peak redshift with decreasing luminosity appears to be significantly smaller than indicated by the data.
In particular, at $z = 1-2$ the observed density of Seyfert–like AGNs is a factor ~ 2 lower than predicted by the model; a similar difference is present also for the intermediate luminosity objects ($L_{2-10} = 10^{44-44.5}\ ergs^{-1}$) in the redshift bin $z = 2-4$.

For $z > 2$, the slight excess of the number and luminosity densities of weak AGNs with $L_X < 10^{44.5}\ erg/s$ over the observations may originate both in the observations and in the modelling.
On the one hand, data incompleteness is to be expected at high z for low–luminosity objects. Although the data are corrected for absorption, the sources would be lost from the sample when heavily obscured below the detection limit (cfr Sect. 3.2, 3.3). Also, the observed number and luminosity densities do not include Compton–thick sources whose contribution is instead included in the model predictions.
However, luminosity functions computed taking into account all the incompletness causes as the best we can (Sect. 3.3) don't seem to solve the disagreement.
Future observations extended to harder bands will clarify the issue.

On the other hand, the excess of predicted low–luminosity AGNs at high z could originate from an incomplete modelling in the low mass regime at high z.
For example, the mismatch may be lifted by a mean AGN lifetime increasing with mass (see Yu and Tremaine 2002), Additional improvements may concern the following sectors:

- The properties of the accretion disks at low accretion rates. Advection-dominated accretion flows might constitute an example of such a physics, though they ought to decrease the emitted luminosity preferentially at high z to explain the excess.

- The regulation governing the amount of cool gas in low-mass host galaxies, like the Supernovae feedback.
  This still represents the most uncertain sector of all SAMs; it is known to play a key role in flattening the faint end of the optical galaxy luminosity functions, since large feed–back would deplete the cold gas reservoirs preferentially in shallow potential wells.

- The statistics of DM haloes. The most recent N–body simulations point toward a mass function of galactic DM clumps somewhat flatter at the small-mass end than previously assumed (see Sheth and Tormen 1999, Jenkins et al. 2001). While this could contribute to solve the issue, the flattening is not large enough to explain out the observed excess.

All the above points can concurr in determining the excess of the predicted low–luminosity AGNs at high z.
We note, however, that overprediction of the low-luminosity sources is a long–standing problem which also affects the number and luminosity distribution of faint, high–z galaxies. This would point toward an origin of the mismatch in the physics of galaxy formation rather than in the description of the accretion processes.

Thus, a real improvement in the modeling requires the inclusion of additional physical processes in the SAM, and in particular in the sector concerning the feedback.
One such process could be well constituted by the inclusion into SAMs of the feedback produced by the AGNs emission itself.
Since the AGN activity strongly increases with redshift, this could significantly contribute to expell/reheat part of the galactic cold gas reservoir in low–mass systems at high z.
While the modeling of such impulsive processes is particulary delicate, some steps in this direction have already been taken (see, e.g., Haehnelt et al. 1998; Silk and Rees 1998; Wyithe and Loeb 2003; Cavaliere et al. 2002; and references therein).
Comparison between observed data and models including AGN feedback could provide key informations about galaxies evolution and models itself.

A further major consideration we have to do is the following: hierarchical models compute self-consistently both the SMBH mass and accretion rate, and the present data do not allow to disentangle the contribution of BH mass and accretion to the observed LF. Indeed, different accretion rates and SMBH masses can combine to yield the same LF.
To tightly constraint the specific predictions of the different competiting models a better approach would be to compare them to mass or accretion rate selected AGN LFs.
For example, sticking to phases of strong nuclear activity only, when the nucleus accretes at, or near, its Eddington luminosity, would provide a much better constrain to the model for what regards major mergings and galaxy assembly.

The final goal of our project is to compare the expectations of galaxy formation models to the obscured and unobscured QSO densities as a function of z.
To disentangle degeneration problems we perform a characterization of our sources that allow us to study AGNs evolution in different ranges of BH masses and accretion rates.
The BH masses and accretion rates estimates have been derived through detailed spectral and morphological study of the sources.

Chapter 4

Morphology

4.1 Morfological analysis

Galaxies span a wide range of morphology and luminosity, and a very useful way to quantify them is to fit their light distribution with parametric functions.
The de Vaucouleurs $R^{1/4}$ and exponential disk functions became standard functions to use after de Vaucouleurs 1948 showed many elliptical galaxies to have $R^{1/4}$ light distributions, while Freeman 1970 found later–type galaxies to be well described by a de Vaucouleurs bulge plus an exponential disk.
Since then the empirical techniques of galaxy fitting and decomposition have led to a number of notable advances in understanding galaxy formation and evolution.
These include investigations into the Tully–Fisher relationship (Tully and Fisher 1977), the fundamental plane of spheroids (Faber et al. 1997; Dressler et al. 1987; Djorgovski and Davis 1987; Bender et al. 1992), the morphological transformation of galaxies in cluster environments (e.g., Dressler 1980; van Dokkum and Franx 2001), the bimodality of galaxy nuclear cusps (Lauer et al. 1995; Faber et al. 1997) and its implications for the formation of massive black holes (Ravindranath et al. 2002), and the cosmic evolution of galaxy morphology (e.g. Lilly et al. 1998; Marleau and Simard 1998).

There are two general types of galaxy fitting: one–dimensional fitting of surface brightness profiles (e.g., Kormendy 1977; Burstein 1979; Boroson 1981; Kent 1985;

Baggett et al. 1998) and two–dimensional fitting of galaxy images (e.g., Shaw and Gilmore 1989; Byun and Freeman 1995 ; de Jong 1996; Simard 1998; Wadadekar et al. 1999; Khosroshahi et al. 2000), each with its own tradeoffs and benefits.
In one dimension an important consideration is how to first obtain a radial surface brightness profile from a two–dimensional image, for which there is no universally agreed upon procedure.
A common practice is to use isophote fitting, which is a powerful technique when performed on well-resolved galaxies because it averages over elliptical annuli to increase the signal-to-noise ratio (S/N) at a given radius. However, as many galaxies have isophote twists and changing ellipticity as a function of radius, the galaxy profile is extracted along a radial arc that is ill defined. An alternative approach is to use a direct one-dimensional slice across an image. Burstein 1979 argues that only cuts along the major axis should be used in bulge-to-disk (B/D) decompositions. Meanwhile, Ferrarese et al. 1994 point out that galaxies with power-law central profiles may have different profiles along the major and minor axis.
Fitting profiles in one dimension is frequently used because it suffices for certain goals and is simple to implement. But many studies now resort to two-dimensional techniques.
For B/D decompositions a number of authors (e.g., Byun and Freeman 1995; Wadadekar et al. 1999) have used idealized simulations to show that two-dimensional modeling can better recover the true parameter values.
In one dimension, while the galaxy bulge and disk may appear to merge smoothly, which causes nonuniqueness in the decompositions, in two dimensions isophote twists and ellipticity changes provide additional constraints to break those degeneracies.
While exponential and de Vaucouleurs functions can model a wide range of global galaxy profiles, galaxies are generally more complex.
Well-resolved, nearby galaxies are often poorly fitted by the standard models in detail, especially in two dimensions.
More recently a growing number of theories and Hubble Space Telescope (HST) observations show that many clues of galaxy formation lay hidden in the fine details of galaxy structure. HST images reveal striking correlations between nuclear cusps of galaxies with their mass, stellar velocity dispersion, radius, and other large-scale properties (Jaffe et al. 1994; Lauer et al. 1995; Faber et al. 1997; Carollo et al. 1997 ; Rest et al. 2001; Ravindranath et al. 2001; Gebhardt et al. 2000 ; Ferrarese and Merritt 2000). Other fossil remnants of galaxy formation manifest as photometrically distinct nuclei, nuclear disks of stars and gas, dust lanes, and nuclear spiral patterns (e.g., Phillips et al. 1996; Carollo et al. 1998; Tomita et al. 2000; Tran et al. 2001).

Active galactic nuclei are intimately related to formation of bulges and black holes; their fuel-starved remnants are common tenants in nearby galaxies (Ho et al. 1997). Yet quantitative investigations of these central sources have often been hampered by the difficulties encountered in separating the faint nucleus from the surrounding bright bulge (see, e.g., Ho and Peng 2001; Sarzi et al. 2001).
In order to understand the physical implications of all these clues, one must be able to extract accurate, quantitative morphological information via detailed galaxy decomposition.
Motivated by these and other possible applications, Peng et al. 2002 developed a technique (GALFIT) to accurately model galaxy profiles.

4.2 Morphological analysis of the HELLAS2XMM high X/O sources

For a subsample, 11 sources, of high X/O and without spectroscopic[a] redshifts in the HELLAS2XMM sample we carried out a near infrared follow–up, making use of the observed property of these sources to have redder colours (Mainieri et al. 2002; Alexander et al. 2002).
We started a pilot study in the K_s band selecting a restricted (11 sources), but meaningful, sample of the HELLAS2XMM high X/O population undetected in the optical band down to the limits of our images (details on data reduction in Chapter 2).
Ten out of 11 sources were securely identified with a relatively bright ($K_s \leq 19$) near-infrared objects.
The bright near-infrared counterparts have optical to near-infrared colors considerably redder than the field population and all of them are classified as EROs, with $R - K > 5$ (Mignoli et al. 2004).
The $R - K$ color distribution of all ISAAC detections with $K_s < 21.5$ is reported in Fig. 4.1.

The exceptional nature of the high X/O counterparts is quite obvious. The six $R - K > 6$ counterparts, with $K_s < 19$ are very rare objects: in this region of the color-magnitude diagram one finds 20 galaxies in total, representing the mere 3% of th whole galaxy population; the three brightest counterparts are unique with respect to the galaxy field population, as no other object share the same photometric properties.

[a]We obtained near–infrared spectroscopy (see Sect. 2.4.1) later on this pilot study.

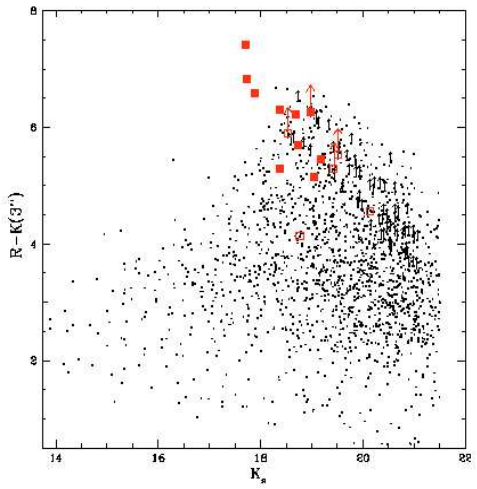

FIGURE 4.1. Fixed–aperture $R - K_s$ color versus "total" K_s magnitude for all the ISAAC detections (small dots) with $K_s < 21.5$; the large filled squares indicate the ten counterparts of the selected hard X–ray sources with high X/O. Mignoli et al. 2004

The excellent quality of the ISAAC images has been fully exploited by combining the photometric information with an accurate morphological analysis.

4.2.1 Near-infrared morphologies: one–dimensional fitting

The morphologies of the near-infrared counterparts were investigated using the IRAF task isophote, which fits each galaxy with elliptical isophotes, providing a radial intensity profile along the semi–major axis.
A least–square fitting, excluding the inner region affected by the seeing, was performed in order to distinguish between exponential and bulge ($r^{1/4}$) profiles (see Mignoli et al. 2004 for detailed description of the procedure).
With the exception of the identifications of Abell 2690 #029 and PKS 0312-77 #045, all of the other sources are clearly extended.

In Table 4.1 are reported the characteristic and morphological clasification of the high X/O sources.

4.3 Two-dimensional image decomposition: GALFIT

In order to model galaxy profiles with a maximum degree of flexibility, GALFIT, after taking in account all observational effect that could affect the real galaxy profile,

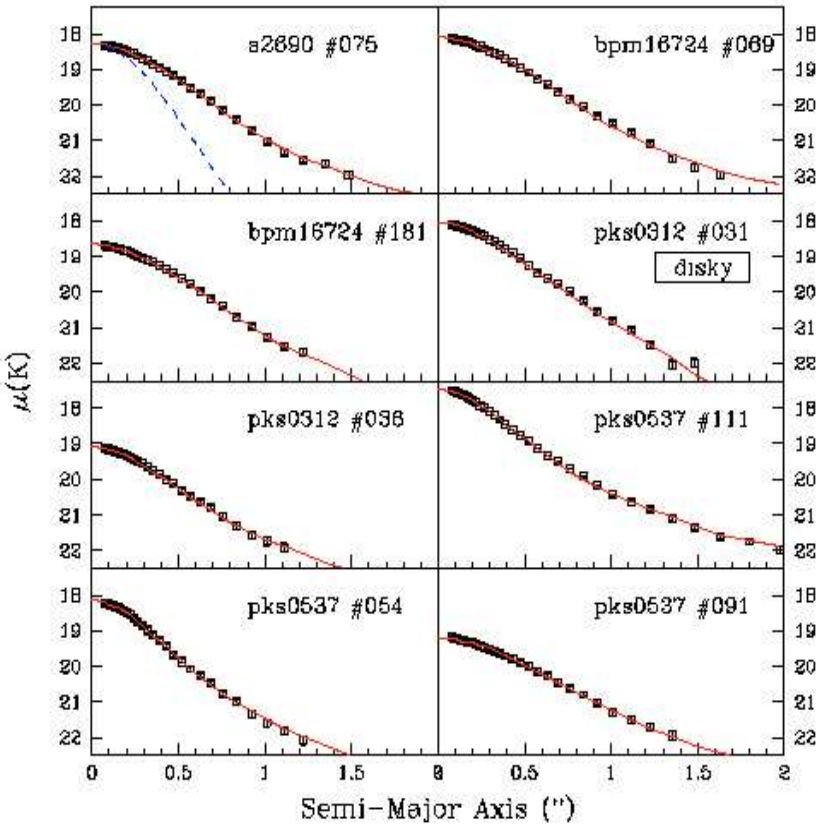

FIGURE 4.2. Surface brightness profiles along the major axis (boxes) and best-fitting models (lines) for all of the extended sources. In the upper left box we also show with a dashed line a representative PSF.

uses several functions and can combine an arbitrary number of them simultaneously.

4.3.1 Accounting for Telescope and Atmospheric Seeing

All recorded images carry an imprint of the observing setup, caused either by imperfections or diffraction in the telescope optics or sometimes by the atmosphere.
To measure the intrinsic profile of an object, the seeing must be taken into account either by convolution or deconvolution techniques.
One way to remove the seeing is to deconvolve the image.
Lauer et al. 1995 show that galaxy images with high S/N at the center can be accurately deconvolved if an accurate PSF is available.
An alternative approach uses convolution, where one constructs a model image and convolves it with a PSF before comparing the result with the data.
While both techniques rely on knowing an accurate PSF, deconvolution has benefits

TABLE 4.1. **Near infrared mono–dimensional morphological parameters**

Source Id.	K_s^a	$R-K^b$	morph	r_{hl}	r_{eff}	gal/nuc^e
Abell 2690 #075	18.32	6.3 ± 0.7	E	0. 56	0. 56	> 40
Abell 2690 #029	17.68	7.4 ± 1.0	P			
BPM 16274 #069	17.83	6.6 ± 0.8	E/D	0. 60	0. 48	> 50
BPM 16274 #181	18.69	6.2 ± 0.4	E	0. 53	0. 37	6.3
PKS 0312-77 #045	18.70	5.7 ± 0.7	P			
PKS 0312-77 #031	18.31	5.3 ± 0.5	D	0. 55	0. 47	1.9
PKS 0312-77 #036	19.11	5.5 ± 0.5	E	0. 55	0. 57	> 18
PKS 0537-28 #111	17.66	6.8 ± 0.7	E	0. 61	0. 70	33.
PKS 0537-28 #054	18.91	> 6.2	E	0. 43	0. 48	7.9
PKS 0537-28 #091	18.99	5.1 ± 0.5	E	0. 66	0. 80	> 25

a) Total magnitude: MAG BEST from SExtractor. b) Fixed 3" -diameter aperture color. d) From least-square fit: P = point-like E = Bulge profile D = Disky profile. e) Ratio between the host galaxy and the unresolved nuclear component fluxes.

when the S/N is high, the observed image needs only to be deconvolved once and one does not have to assume a particular model for the intrinsic image.
However, deconvolution will not work well for low-S/N or undersampled images, because it may amplify Poisson and pixellation noise.
In contrast, the convolution scheme works on images with both high or relatively low S/N. The drawback is that fitting an image proceeds more slowly because convolution is done repeatedly, which is computationally intensive.
GALFIT uses convolution done by using the convolution theorem: it multiplies the Fourier transforms of the PSF and the models, and then inverse transform them (details in Peng et al. 2002).

4.3.2 Computing the χ^2_ν

The four input images for GALFIT are the CCD image of the galaxy, a noise array, a PSF, and an optional dust (or bad pixel) mask. Pixels in the dust mask are rejected from the fit.
During the fit χ^2_ν (the reduced χ^2) is minimized, defined in the standard way as

$$\chi^2_\nu = \frac{1}{N_{dof}} \sum_{x=1}^{nx} \sum_{y=1}^{ny} \frac{(flux_{x,y} - model_{x,y})^2}{\sigma^2_{x,y}} \tag{4.1}$$

where

$$model_{x,y} = \sum_{\nu=1}^{nf} f_{\nu,x,y}(\alpha_1.....\alpha_n) \tag{4.2}$$

Ndof is the number of degrees of freedom in the fit; nx and ny are the x and y image dimensions; and $flux_{x,y}$ is the image flux at pixel (x, y). The $model_{x,y}$ is the sum of the nf functions $f_{\nu,x,y}(\alpha_1.....\alpha_n)$ employed, where $\alpha_1.....\alpha_n$ are the two-dimensional model parameters.
The uncertainty as a function of pixel position $\sigma_{x,y}$ is the Poisson error at each pixel, which can be provided as an input image. If no noise image is given, one is generated based on the gain and read-noise parameters contained in the image header.

4.4 Galaxy Radial Profiles

4.4.1 The Sersic profile

The Sersic (1968) profile has the following form:

$$\sum(r) = \sum_e e^{-k[(\frac{r}{r_e})^{\frac{1}{n}}-1]} \tag{4.3}$$

where r_e is the effective radius of the galaxy, $\sum_e$ is the surface brightness at r_e, n is the power-law index, and k is coupled to n such that half of the total flux is always within r_e. For $n > 2$, $k \sim 2n - 0.331$; at low n, $k(n)$ flattens out toward 0 and is obtained by interpolation.
The original de Vaucouleurs (1948) profile is a special case with $n = 4$ and $k = 7.67$. While the de Vaucouleurs profile is well suited for "classical " bulges, some bulges may be better represented by exponential profiles (e.g., Kormendy and Bruzual A. 1978; Shaw and Gilmore 1989; Kent et al. 1991; Andredakis and Sanders 1994).
The elegance of the Sersic profile is that it forms a continuous sequence from a Gaussian ($n = 0.5$) to an exponential ($n = 1$) to a de Vaucouleurs ($n = 4$) profile simply by varying the exponent. It is very useful for modeling bars and flat disks; the smaller the index n is, the faster the core flattens within $r < r_e$, and the steeper the intensity drop beyond $r > re$. The flux, integrated over all radii for an elliptical Sersic profile with an axis ratio q, is

$$F_{tot} = 2\pi r_e^2 \sum_e e^k n k^{-2n} \Gamma(2n) \frac{q}{R(c)} \tag{4.4}$$

where $\Gamma(2n)$ is the gamma function. F_{tot} is converted into a magnitude by GALFIT using the standard FITS exposure time parameter (EXPTIME) in the image header. $R(c)$ is a function that accounts for the area ratio between a perfect ellipse and a generalized ellipse of diskiness/boxiness parameter c, given by

$$R_c = \frac{\pi c}{4\beta(1/c, 1+1/c)} \tag{4.5}$$

where $\beta(1/c, 1+1/c)$ is the " beta " function with two arguments.
In the two-dimensional implementation the Sersic model has eight free parameters: x_{cent}, y_{cent}, F_{tot}, r_e, n, c, q, P.A. We note that in place of fitting $\sum_e$, F_{tot} is fitted instead, which is more often a useful parameter. This is also done for all other models below, except for the Nuker function.

4.4.2 The exponential disk profile

The exponential profile and the total flux are simply

$$\sum(r) = \sum\nolimits_0 e^{r/r_s} \tag{4.6}$$

and

$$F_{tot} = 2\pi r_s^2 \sum\nolimits_0 \frac{q}{R(c)} \tag{4.7}$$

where $\sum_0$ is the central surface brightness and r_s is the disk scale length. The relationship between the half-light radius r_e and the scale length r_s is $r_s = 1.678 r_e$ for this profile. Most disky galaxies are not composed of a single exponential disk, but also have either a central Sersic or de Vaucouleurs component. They may also have either a flat core or a truncated disk, which deviates from a simple exponential (e.g., van der Kruit 1979; Pohlen et al. 1979).

4.4.3 The Gaussian profile

The Gaussian function and its total flux are

$$\sum(r) = \sum\nolimits_0 e^{r^2/2\sigma^2} \tag{4.8}$$

and

$$F_{tot} = 2\pi\sigma^2 \sum\nolimits_0 \frac{q}{R(c)} \tag{4.9}$$

The full width at half maximum (FWHM) is 2.355σ The two-dimensional model has seven free parameters: x_{cent}, y_{cent}, F_{tot}, σ, c, q, P.A.

4.4.4 Creating Point Sources

To create a true point source, one normally creates a δ-function that is then convolved with the input PSF.
Using GALFIT it is better to approximate a δ-function by using a Gaussian (or

Moffat) function having a small width, usually FWHM<= 0.3 pixels. The benefit of using a functional representation is that the algorithm can smoothly transit between fitting a true point source or a compact source without a loss of generality.

4.4.5 Creating Bars

Spiral galaxies can have embedded bars. The usual way to model them is to use the Sersic profile with initially a relatively flat inner and a steep outer profile ($n < 1$) and a boxy shape ($c > 0$).
The true light distribution of a bar also has a bulbous component at the center, distinct from the bulge. Therefore, one should in principle use two components. However, the round component may be partially degenerate with the bulge itself unless the two profiles are significantly different. Interesting further details about point sources extraction can be found in Peng et al. 2002.

4.5 GALFIT Implementation

In the following I report the steps followed by GALFIT.

- Normalize and prepare the PSF for convolution
- " Cut out" a section of the image centered on the object to fit from the original data image
- Create model and derivative images based on the initial input parameters
- Cut out the convolution region from the model and derivative images in the previous step and pad them around the edges with values of the models
- Convolve the convolution regions (both model and derivative images) in previous step with the PSF using a fast Fourier transform (FFT) technique
- Copy the convolution region back into the model/derivative images of step 3
- Compare with data image. Minimization is done using the Levenberg-Marquardt downhill-gradient method/parabolic expansion (Press et al. 1997)
- Iterate from step 3 until convergence is achieved
- Output images and generate final parameter files

4.6 Fitting Procedures

To use GALFIT in a typical manner, such as for B/D decomposition there is little to no human interaction beyond preparing an initial parameter file. However, the task of accurately fitting galaxies is considerably more challenging; I outline the steps to usually follow:

- Always start out with a Sersic profile to understand the concentration degree of the source.
- Optimize all the parameters in a χ^2 sense.
- Examine the residuals to decide whether: to add more components; to make better pixel masks, to free parameter values that have first been held fixed, or to replace component with more flexible models.
- If there is the need for a new component, add it and repeat previous steps as necessary.

4.6.1 Degeneracy and the Significance of the Components

Degeneracy is a common problem in galaxy decompositions, mostly because the model functions used are not selected based on physical criteria.
One can, in principle, decompose a galaxy with as many " basis functions " as one might contrive. Extending to more components might, at first sight, make the situation unmanageable. However imposing the demand that models fit galaxies with high fidelity ($\chi^2 \sim 1$) severely reduces the possible solution space for a given set of models; most solutions can be easily dismissed based on χ^2 analysis.
Such demand produces components that have significantly different scale lengths, axis ratios, etc. While there is no recipe to guarantee uniqueness in the fitting, there are ways to probe the parameter spaces exhaustively and to satisfy to one's own confidence that a solution is stable and insensitive to initial conditions.
One way is to vary two parameters at a time on a Cartesian grid of values in order to trace out the local χ^2 contours.
This technique is very useful when the number of parameters is low. However, the same technique quickly becomes intractable with increasing number of fitting parameters. To more effectively explore a wider χ^2 topology it is recomended the follow the steps below:

- Randomly select a full set of parameters, possibly drawing from distributions of parameter values centered on the best-fit values.

- Using these as initial values, minimize the χ^2.
- Repeat step 1 for many different sets of random initial guesses to see whether they return the same optimized solution or to other equally plausible ones.

A different, but perhaps more interesting, tactic is to explicitly seek out components motivated by theory, such as evidence for a nuclear point source based on AGN spectra or decoupled cores based on kinematic data.
Lastly, from a purely empirical standpoint, one can decompose a galaxy simply to look for structures too subtle to be seen in full light, such as weak nuclear bars, stellar disks, and nuclear point sources.
The last scenario brings the discussion back in full circle to the issue of degeneracy. Despite possible degeneracies in decomposing large-scale components, smaller structures are better localized, and better defined in size and shape. Even if there is doubt as to what the exact profile and parameters are, often different models can reproduce a component with similar overall characteristics (e.g., profile, scale length, shape, and orientation) even if they are not exactly identical. That a similar component is repeatedly borne out through different profile assumptions is in principle the keystone of its reality, since its inclusion is essential to achieving a rea- sonable model fit in that region of the image.

4.7 Near-infrared morphologies: bi–dimensional fitting

We benefited of the very good quality of the near–infrared images (seeing $< 0.8''$) to study the near-infrared morphologies in a more detailed way, performing the bidimensional images decomposition.
We used the GALFIT algorithm and the procedure described above; in the following I will report two–dimensional fitting results and the comparison between these latter and those obtained performing one–dimensional approach.

Source A2690 #75
Through the mono–dimesional approach this source is classified like an elliptical galaxy.
Through bi–dimesional B/T decomposition we classify this source like a disky galaxy: looking at the surface brightness profile along the major axis compared to the best fitting model reported in Fig. 4.3 we note that the different classification could be due to the weight that the background, i.e. the extern region $r \sim 1.5''$, has on the mono–dimensional fit, see Fig. 4.2.

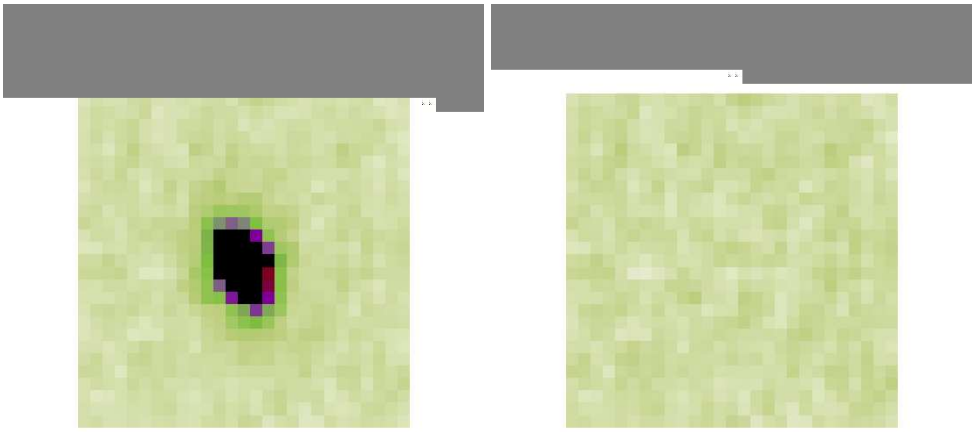

FIGURE 4.3. Left: near–infrared image of the source A2690_75. Right: Residual image.

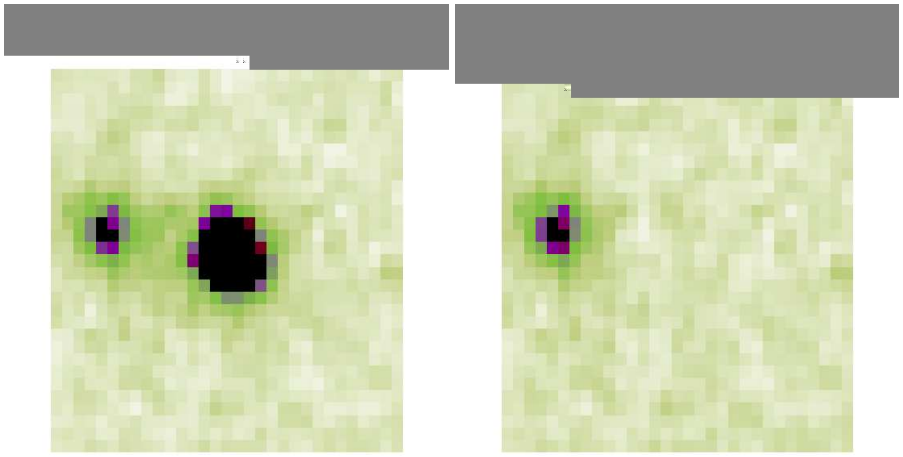

FIGURE 4.4. Left: near–infrared image of the source BPM16274_181. Right: Residual image.

Source BPM 16274 #181

In this case mono– and bi–dimensional approach yield the same classification, Fig. 4.4.

Source BPM 16274 #69

As regard this source the mono–dimensional fitting yields an ambiguos classification. Through bi–dimesional B/T decomposition we classify this source like an elliptical

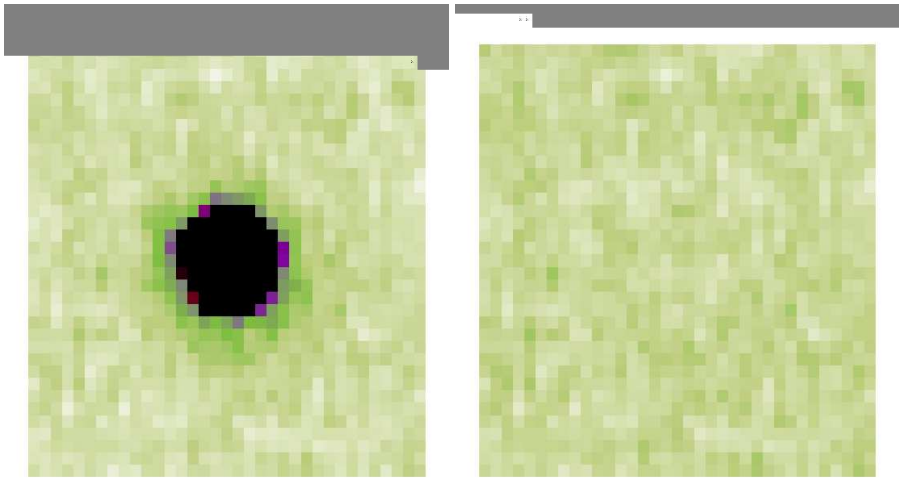

FIGURE 4.5. Left: near–infrared image of the source BPM16274_69. Right: Residual image.

galaxy Fig. 4.5.
We have to note that mono–dimesional classification is chosen after cheking by eye the two-dimensional "object-model" image of the model giving the smallest residuals compared to the observed profile: this procedure can often produce confusion.

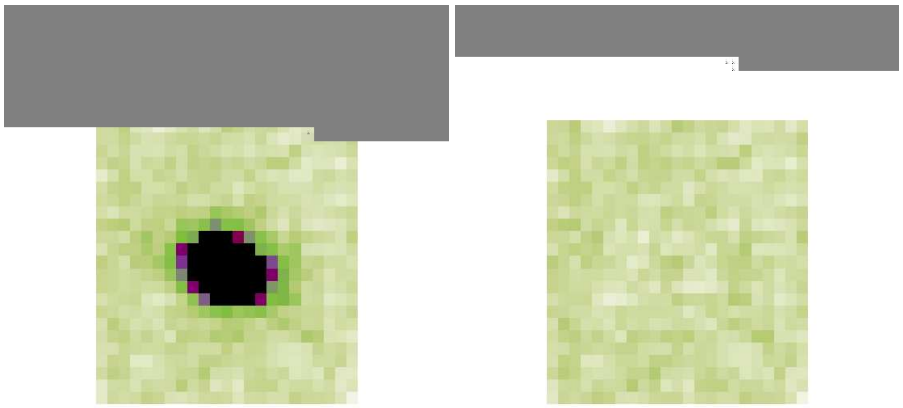

FIGURE 4.6. Left: near–infrared image of the source PKS0312_31. Right: Residual image.

Source PKS0312 #31

Through mono–dimesional fitting this source is classified like a disky galaxy.
Our classification prefers a model with two components with a bulge/total ratio ~ 0.8, Fig. 4.6.
We note in Table 4.1 that for this source the gal/nuc ratio is rather small, this is the sign that mono–dimensional approach find a concentrated source.

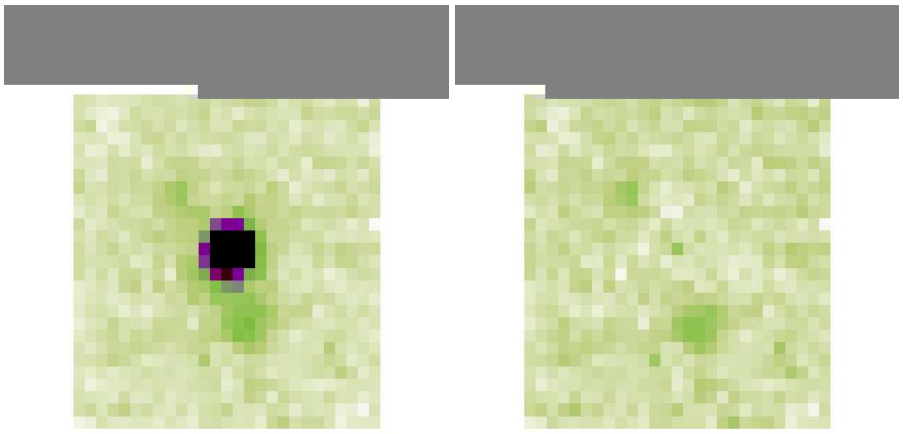

FIGURE 4.7. Left: near–infrared image of the source PKS0312_45. Right: Residual image.

Source PKS0312 #45

Also the bi–dimensional decomposition classifies this sources like a point–source one. Even if there are two near galaxies that could influence the fit, there is no doubt that the source is very compact, Fig. 4.7.

Source PKS0312 #36

Mono and bi–dimesional fitting agree in classifying the source like an elliptical galaxy, Fig. 4.8.

Source PKS0537 #54

Mono and bi–dimesional fitting agree in classifying the source like an elliptical galaxy,

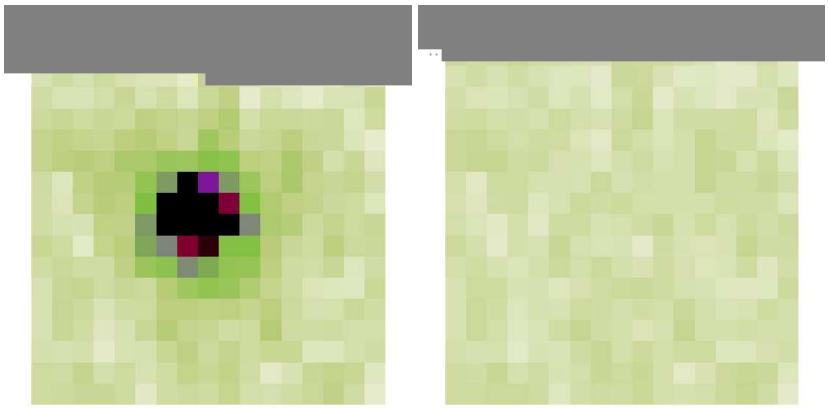

FIGURE 4.8. Left: near–infrared image of the source PKS0312_36. Right: Residual image.

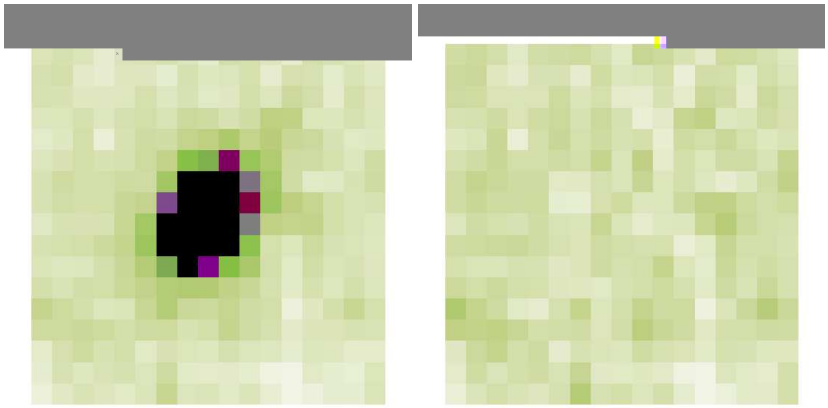

FIGURE 4.9. Left: near–infrared image of the source PKS0537_54. Right: Residual image.

Fig. 4.9.

Source PKS0537 #91

We classify the source like an elliptical galaxy, Fig. 4.10.

Source PKS0537 #111

Mono and bi–dimesional fitting agree in classifying the source like an elliptical galaxy Fig. 4.11.

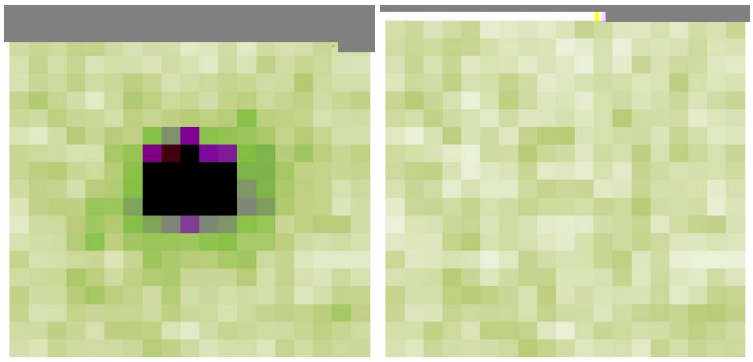

FIGURE 4.10. Left: near–infrared image of the source PKS0537_91. Right: Residual image.

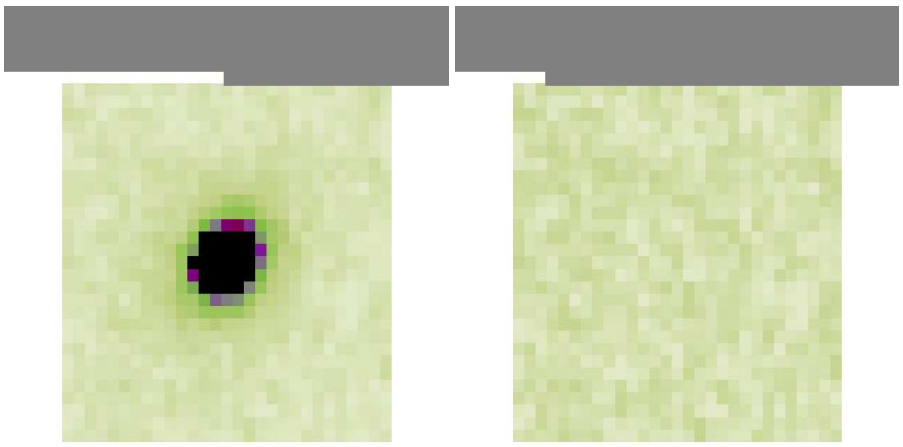

FIGURE 4.11. Left: near–infrared image of the source PKS0537_111. Right: Residual image.

4.8 Morphological analysis of the GOODS high X/O sources

We extended our analisys to a sample of optically obscured sources in the GOODS fields taking advantage of the superior image quality of the HST images.
The Great Observatories Origins Deep Survey (GOODS) is designed to reach unprecedented depths in two fields, the Chandra Deep Field-South (CDF–S) and Hubble Deep Field-North (HDF–N), using HST (Advanced Camera for Surveys, ACS), Chandra, and SIRTF.
The GOODS project provides an ACS mosaic covering 163 arcmin2 (in B435, V606,

i775, and z850 bands), supported by U'UBVRIJHKs broadband imaging from the Very Large Telescope (VLT), New Technology Telescope, and 2.2 m telescopes.
We limit our present analysis to the GOODS CDF–S field, where the most complete multiwavelength photometric data are currently available (Giavalisco et al. 2004).
We performed our morphological analysis on the reddest band available (z band for ACS images; K_s ISAAC band) in order to accurately measure the ligth coming from the bulge stellar population.

We selected a subsample of hard X–ray selected sources in the CDF–S samples choosing objects with the highest X/O ratios: $-0.9 < Log(X/O) < 1.2$

In recent years, high–resolution images from the Hubble Space Telescope (HST) have proved extremely valuable in obtaining the structural parameters of galaxies out to moderate redshifts.
High–resolution allow us to look for structure such as nuclear bars or dusty lanes but, at the same time makes very complex a detailed bi–dimensional image decomposition.

I report some examples of bi–dimensional morphological analisys in the following figures (Fig. 4.12 ÷ 4.17).

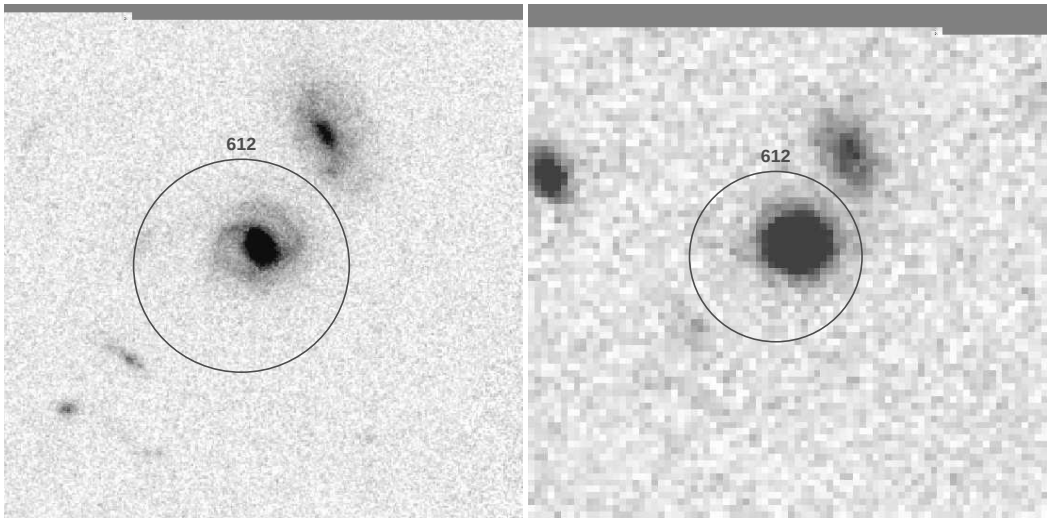

FIGURE 4.12. Left: ACS z band image of the source CDFS #612 (LEX–AGN2). Right: K_S band image. Circles are the *Chandra*–detection error–box (2″).

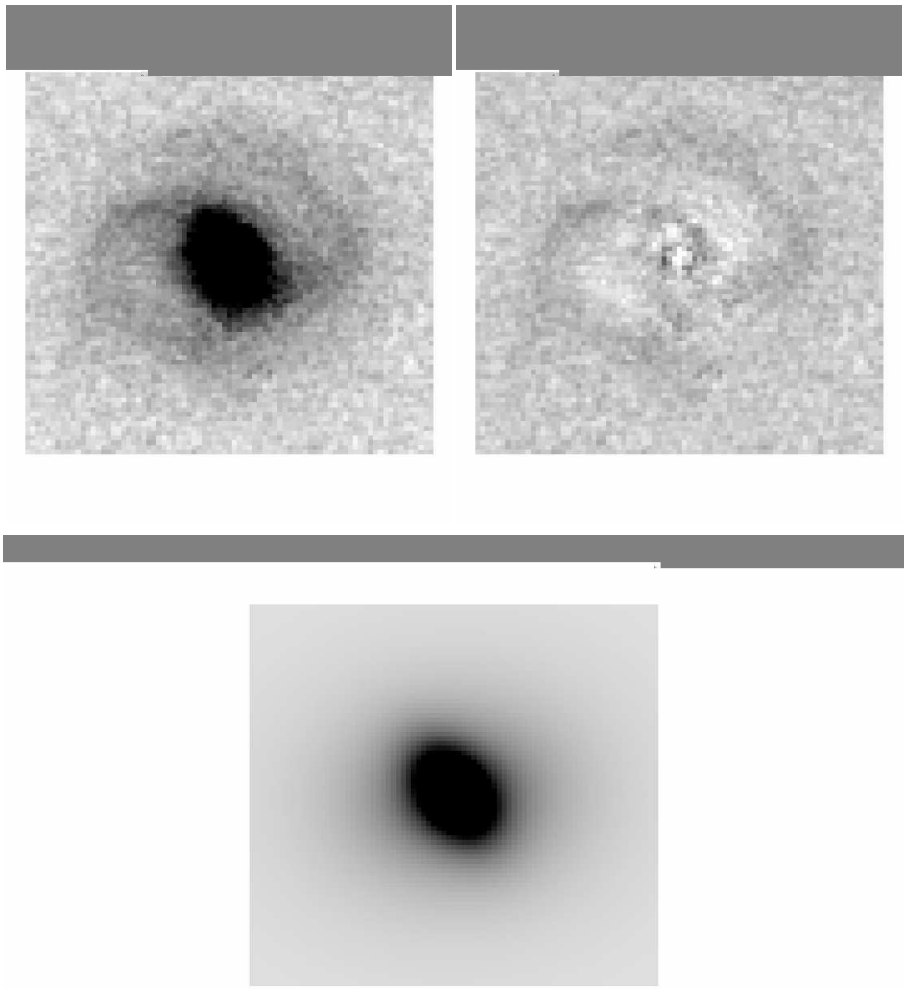

FIGURE 4.13. Left: ACS z band image of the source CDFS #612 (LEX–AGN2). Right: residual image. Bottom: model image fitted.
Decomposition analysis yield a classification with bulge–disk components: B/T = 0.39.

4.9 The Black Hole Mass estimate

Once we obtained the measure of the bulges magnitude we proceeded to estimate the BH masses making use of the well known correlation (cfr. Introduction) between BH masses and bulge luminosities.

We chose the correlation from McLure and Dunlop 2002:

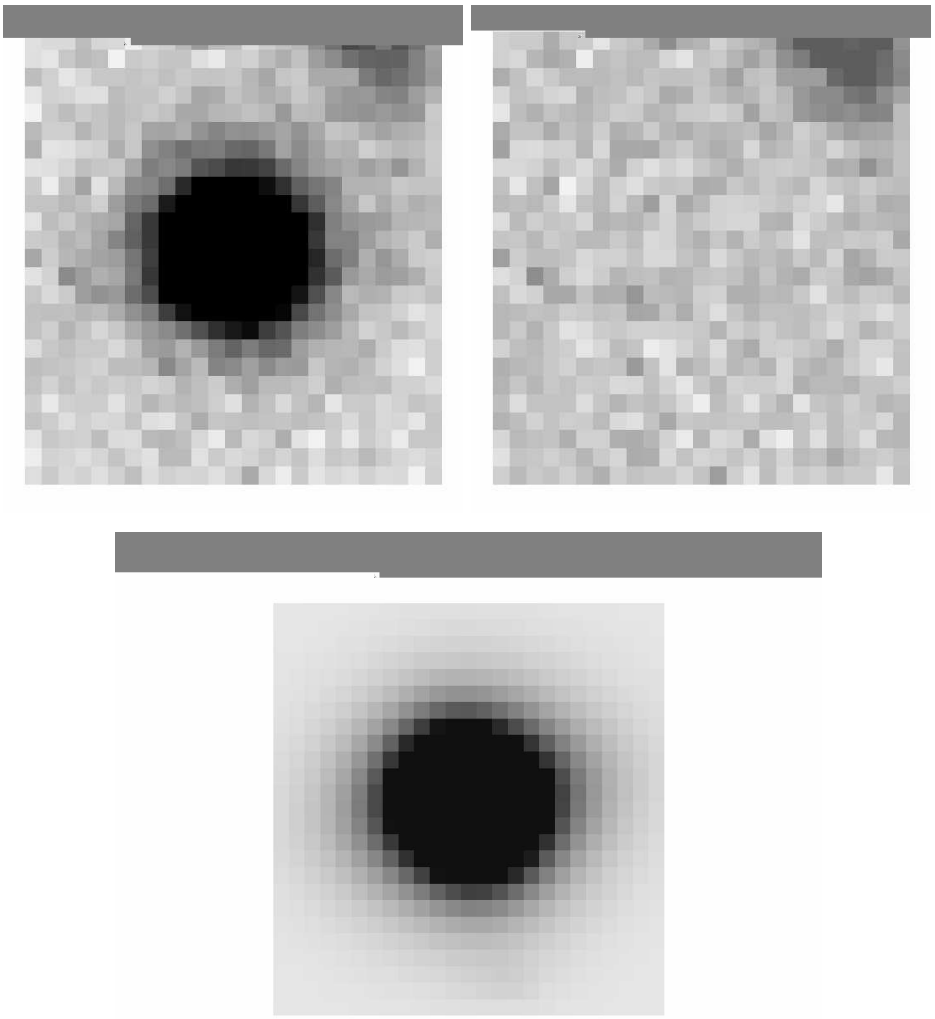

FIGURE 4.14. Left: K_s band image of the source CDFS #612. Right: residual image. Bottom: model image fitted.
Decomposition analysis yield a classification with bulge–disk components: B/T = 0.5.

$$Log(\frac{M_{BH}}{M_{\odot}}) = -0.5(\pm 0.02)\, M_R - 2.96(\pm 0.48) \tag{4.10}$$

McLure and Dunlop 2002 analysed a sample consisting of 90 objects comprising three subsamples of 53 quasars, 19 Seyfert 1 galaxies and 18 inactive nearby galaxies. The principle objective behind the construction of the sample was to allow the study of the bulge/black hole mass relationship over the widest possible dynamic range in

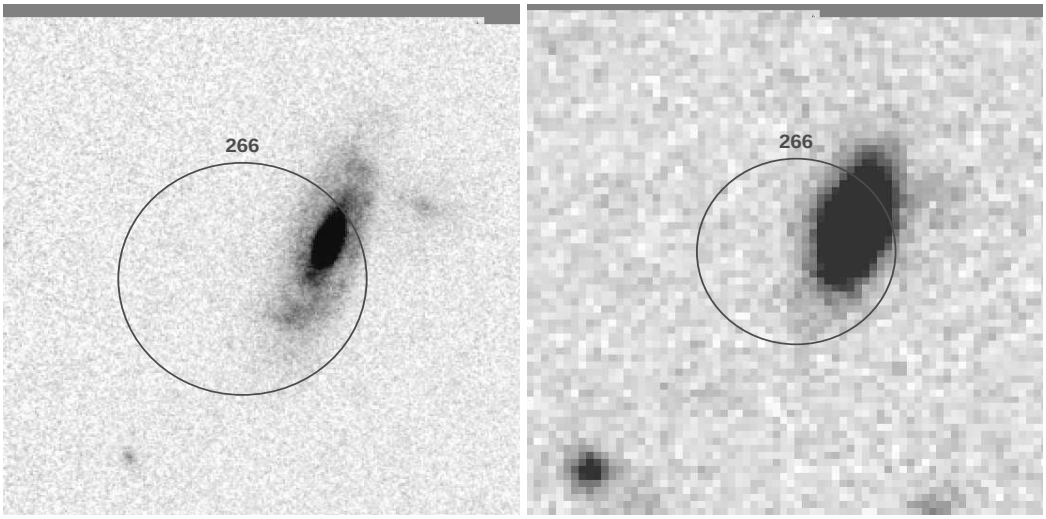

FIGURE 4.15. Left: ACS z band image of the source CDFS #266 (LEX–AGN2). Right: K_S band image. Circles are the *Chandra*–detection error–box (2″).

both nuclear luminosity and central black hole mass.
They found that the M_{BH}-L_{bulge} relation is consistent with a linear scaling between black hole and bulge mass ($M_{BH} \propto {M_{bulge}}^{0.95\pm0.05}$) in agreement with recent black hole mass studies based on stellar velocity dispersions. Furthermore, the scatter around the relation for the full sample is found to be significantly smaller than previously reported, e.g. Kormendy and Gebhardt 2001, (Δ Log $M_{BH} = 0.39$ dex) and comparable with that of M_{BH}–σ relation, demonstrating that much of the previous measured scatter can be due to the difficulty of accurately determining the bulge luminosities of late-type galaxies, even at z$<$ 0.1 (Shankar et al. 2004).

To use the correlation from McLure and Dunlop 2002 we converted all our magnitudes in the Vega system then we used the Elliptical/$S0$ template from Coleman et al. 1980 (CWW, Fig. 4.18), the most popular among the observed templates of local galaxies, to obtain k and color corrections to convert our z and K_S magnitudes to R ones.
The estimated black hole masses as function of redshift are reported in Fig. 4.19.

As we can clearly note in the upper panel of Fig. 4.19 there is a mismatch between BH mass estimates obtained from z and K_S bands images.
We compared our image–decomposition results with results from Mignoli et al. 2004: in Fig. 4.20 we show the Kormendy relation obtained through mono–dimensional analysis in Mignoli et al. 2004 and the Kormendy relation obtained through our

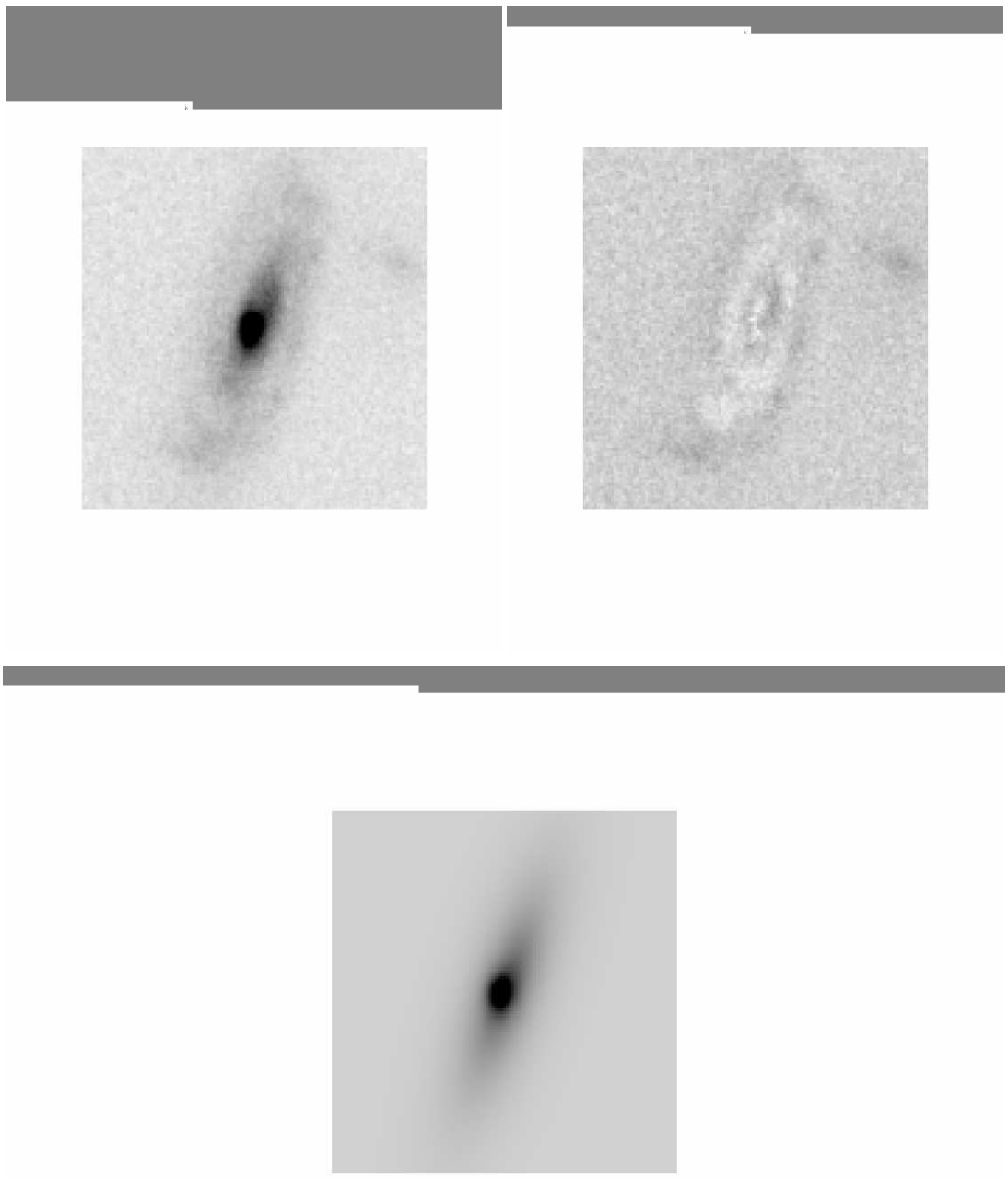

FIGURE 4.16. Left: ACS z band image of the source CDFS #266 (LEX–AGN2). Right: residual image. Bottom: model image fitted.
Decomposition analysis yield a classification with bulge–disk components: B/T = 0.1.

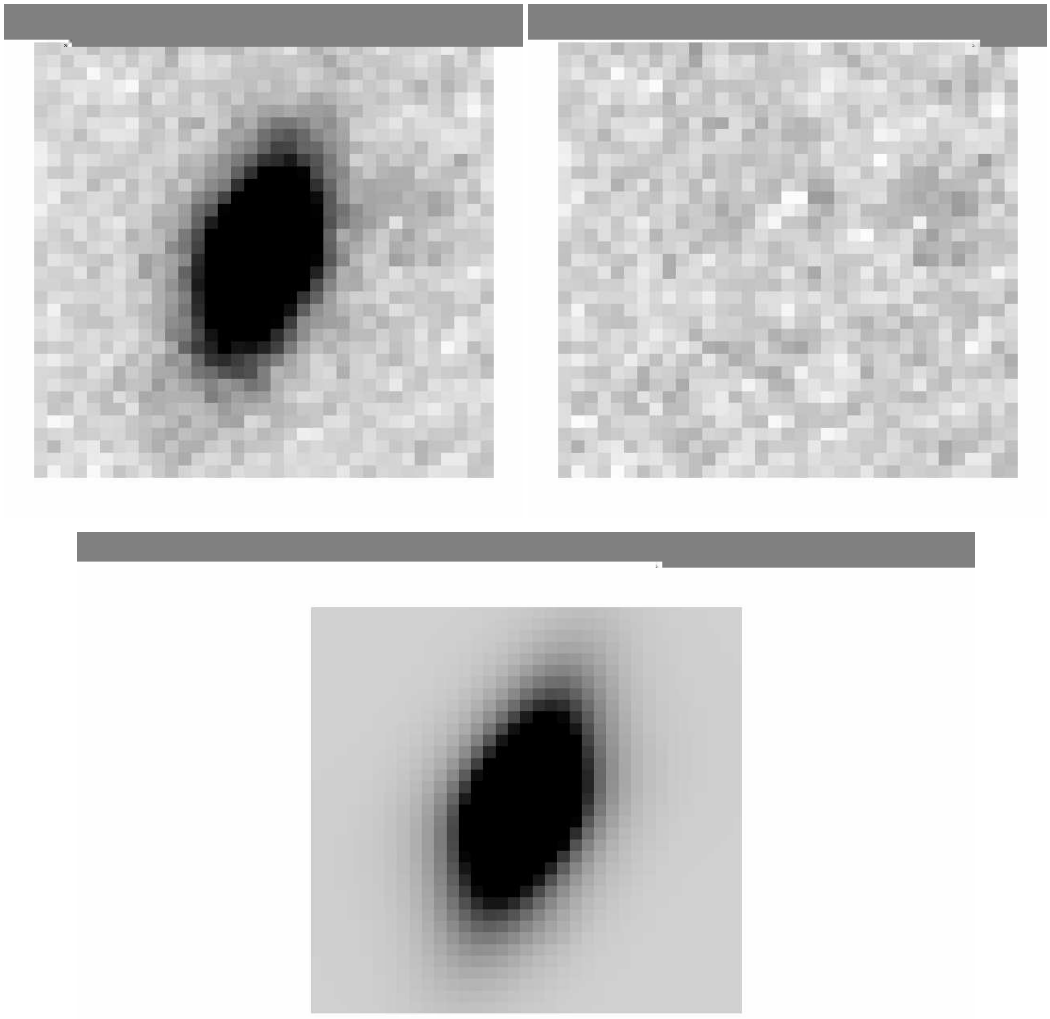

FIGURE 4.17. Left: K_s band image of the source CDFS #266. Decomposition analysis yield a classification with bulge–disk components: B/T = 0.2.

bi–dimensional image decomposition for the HELLAS2XMM high X/O sources. The agreement between our results is good, both in magnitude and effective radius, so we retain reliable our K_S band image analysis.
Furthermore, we can see in Fig. 4.19 that BH mass estimates for HELLAS2XMM and K_S–GOODS samples are consistent so, in the subsequent analysis, we consider results from K_S image decomposition only.
Nevertheless, there is no doubt that the mismatch between z and K_S bands estimates demands an accurate study of all the possible causes yielding these results;

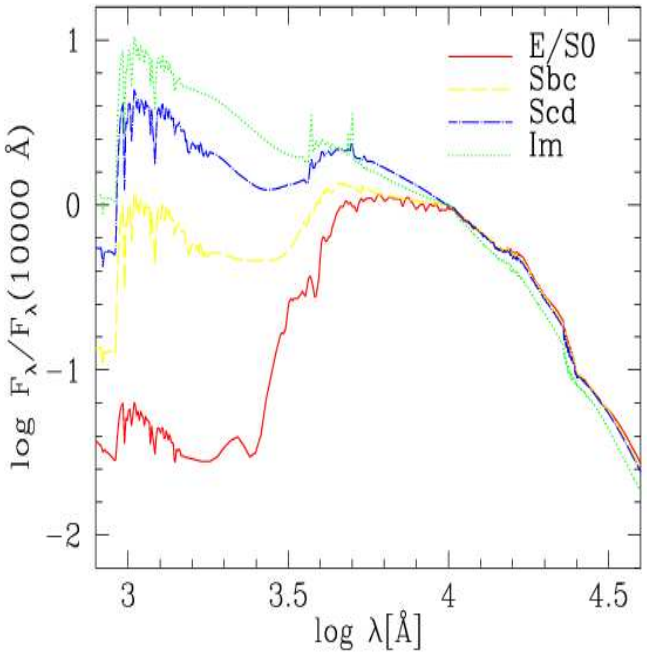

FIGURE 4.18. The four CWW mean observed spectra of local galaxies. The original data of CWW extend only from 1400 to 10000 $\dot{A}$, the extrapolations at UV and near–infrared wavelengths are from the spectral evolutionary models of Bruzual A. and Charlot 1993.

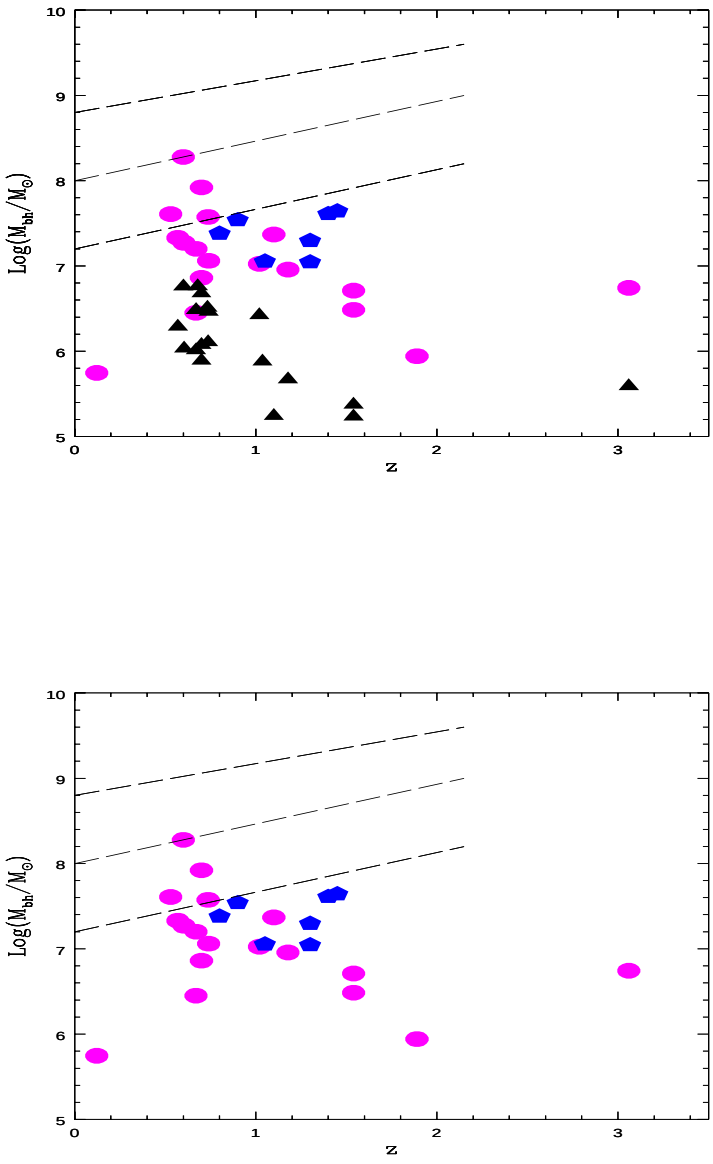

FIGURE 4.19. Black hole masses as function of z for the HELLAS2XMM (pentagons) and GOODS (K_S = circles; z = triangles) high X/O sources. Dashed lines represents the locus of virial black hole mass estimate versus redshift for the SDSS quasar (type 1) sample from McLure and Dunlop 2004.

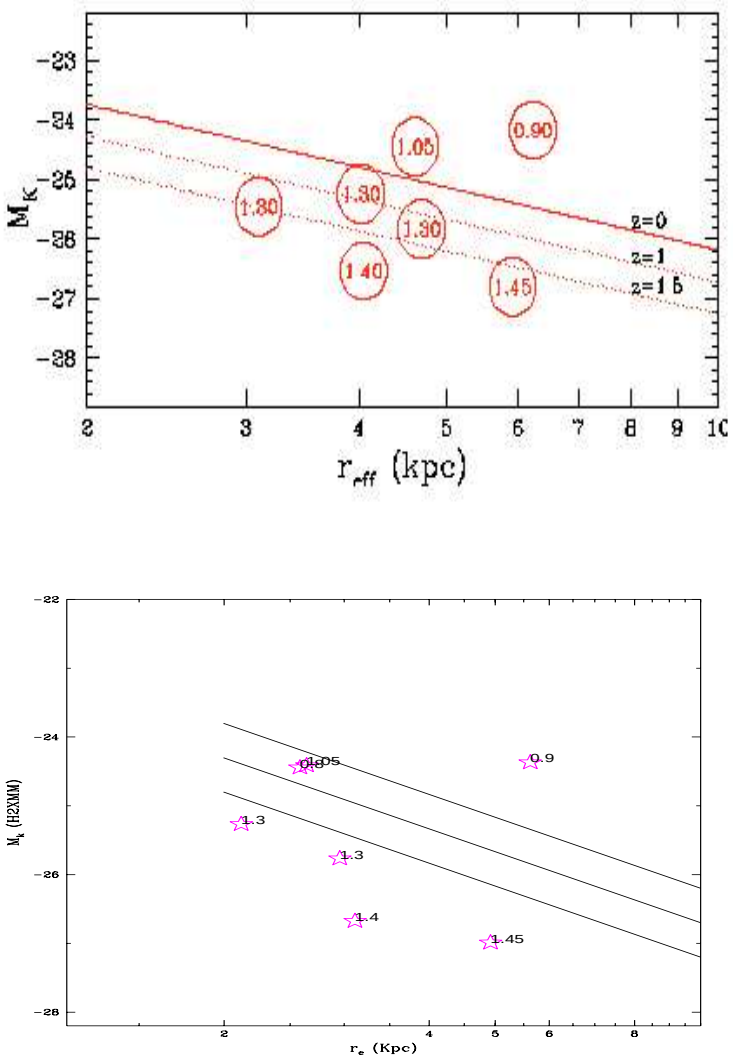

FIGURE 4.20. Effective radius vs. luminosity relation for extended objects with a bulge component. Objects are identified by their z.
The solid line shows the local relation from Pahre et al. 1998, while the dotted lines show its evolution at z = 1 and z = 1.5, assuming the luminosity evo- lution derived by Pozzetti et al. 2003.

the analysis is ongoing.

The Eddington and the bolometric luminosities were estimated through:

$$L_{Edd} = 1.38 \times 10^{38} \times \frac{M_{BH}}{M_{\odot}} \qquad (erg/s) \qquad (4.11)$$

$$L_{bol} = k \times L_{X_{2-10keV}} \qquad (erg/s) \qquad (4.12)$$

where the k correction factor from X–ray to bolometric luminosity is from Marconi et al. 2004.

The bolometric luminosity as a fraction of the Eddington limit versus redshift and black hole masses are reported in Fig. 4.21.

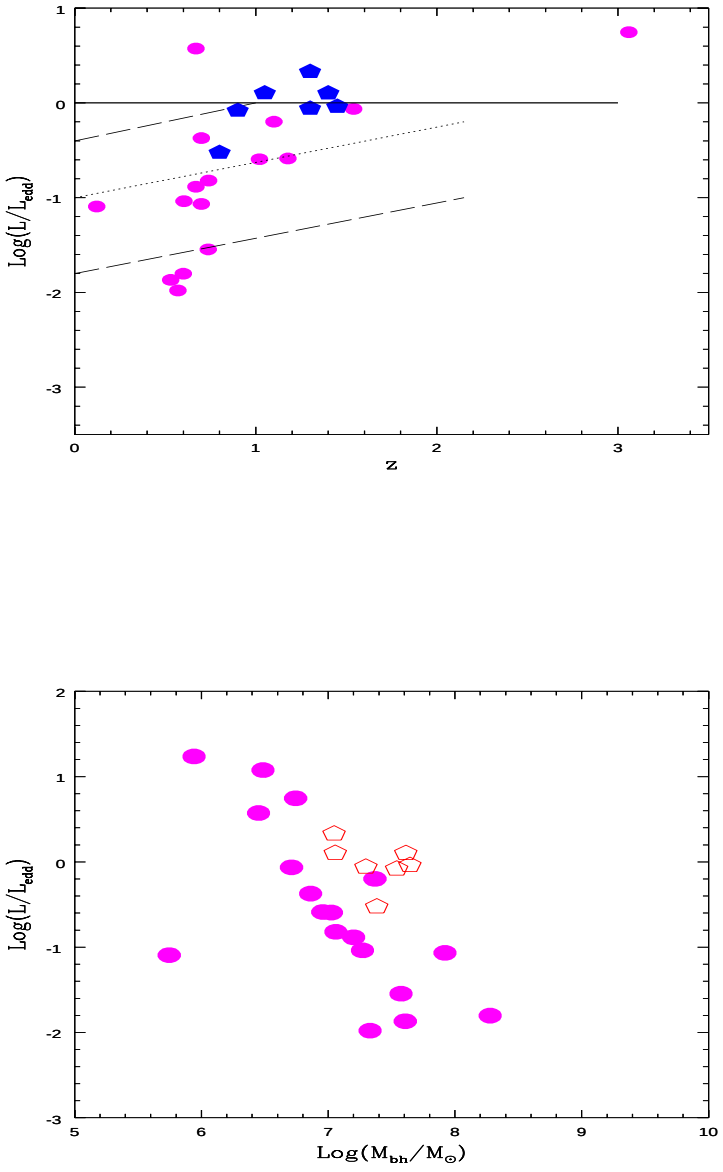

FIGURE 4.21. Bolometric luminosity as a fraction of the Eddington limit as function of z and black hole masses for the HELLAS2XMM (pentagons) and GOODS (circles) high X/O sources. Dashed lines represents the locus of virial black hole mass estimate versus redshift for the SDSS quasar (type 1) sample from McLure and Dunlop 2004.

Chapter 5

The HELLAS2XMM survey: The broad line AGN sample

To estimate the black hole masses of the type 1 AGN sample drawn from the HELLAS2XMM survey we performed a detailed analisys of their optical spectra in order to make use of the well known relations between the FWHM of the broad emission lines and the BH masses.
On the other hand the morphological analysis described in the previous chapter is not well suited to accurately measure the light from the bulge of the unobscured AGNs hosting galaxies as, in these sources, the light from the nucleus dominates the whole host galaxy altering, in this way, its surface brightness profile.

The sample cover a redshift range of $0.246 < z < 3.276$, with most objects lying at $z \leq 2$ and consists of 87 type 1 quasars.
The remaining objects were excluded for having too weak emission lines or for beeing affected by strong absorption lines.
A $H_0 = 70$ km s^{-1} Mpc^{-1}, Ω_M=0.3, $\Omega_\Lambda = 0.7$ cosmology is adopted throughout.

5.1 The virial black hole mass estimate

Our objetcs have $0.246 < z < 3.276$, so we used either optical or UV mass estimators. The optical (Hβ) and UV (MgII) mass estimators are that derived by McLure and

Jarvis 2002

$$\frac{M_{bh}}{M_{\odot}} = 3.37(\frac{\lambda L_{3000}}{10^{37}W})^{0.47}[\frac{FWHM(MgII)}{Kms^{-1}}]^2 \quad (5.1)$$

$$\frac{M_{bh}}{M_{\odot}} = 4.74(\frac{\lambda L_{5100}}{10^{37}W})^{0.61}[\frac{FWHM(H\beta)}{Kms^{-1}}]^2 \quad (5.2)$$

while the UV (CIV) mass estimator is taken from Vestergaard 2002

$$\frac{M_{bh}}{M_{\odot}} = 1.6 \times 10^6(\frac{\lambda L_{1350}}{10^{44}W})^{0.7}[\frac{FWHM(CIV)}{Kms^{-1}}]^2 \quad (5.3)$$

The emission lines were fitted using two gaussians, representing the narrow and broad components, after subtracting a power law continuum.
The narrow components were forced to fulfill the condition FWHM$<$ 2000 km s^{-1}.
To account for the blending with FeII emission we constructed a FeII emission template around MgII from an archival IUE spectrum of the narrow–line Seyfert 1 galaxy I Zw 1. The obtained template was riscaled in intensity in pure FeII emission windows, as described by Vestergaard and Wilkes 2001, to match the observed spectra, and then subtracted out (Fig. 5.2).
The continuum luminosity was estimated by fitting a continuum to the QSO template spectrum taken from Francis et al. 1991.
We used the measured R band magnitudes to riscale in intensity the template spectrum, so that, once convolved with the R filter, the integrated flux of the template corresponds to the observed R magnitude. We used this method to accurately measure continuum intensity as our spectra could suffer flux loss especially in the bluer range of wavelength due to observations conditions.
The measured parameters are reported in Table 2.
Considering that our sample is X-ray selected and, therefore, can be affected by substantial absorption (as compared with an optically selected one), we used, in addition to an absorption free template, some QSO template spectra with different amounts of absorption ($A_V = 0.1, 0.3, 0.5, 1$ magnitudes).
The absorbed spectra were constructed using a SMC extinction law, following Richards et al. 2003.
The calculated factors to apply to the mass estimate in case of absorption are reported in Table 1. We note that for moderate absorption the BH masses estimate result affected by a factor < 2, well within the scatter of the FWHM–BH mass relation ($\delta\ Log M_{BH} \sim 0.3$).

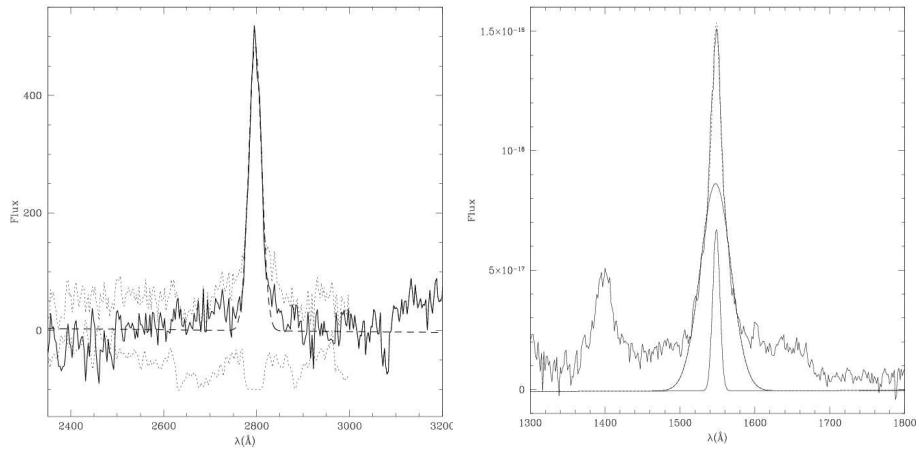

FIGURE 5.1. Left panel: example of FeII template subtraction and gaussian fit of MgII (flux in arbitrary units). Right panel: two-component gaussian fit of CIV.

5.2 Results

We compared the MgII and the CIV FWHM and mass estimates for the 13 objects in the appropriate redshift range.

A discrepancy of a factor of ≈ 10 between the two estimates is apparent from the inspection of Figure 2.

As it has been noted by other authors (Dietrich and Hamann 2004 and references therein), it may be due to the uncertainty in the slope of the relation between the Broad Line Region radius (R) and the continuun luminosity (L).

It has been shown that a flatter slope in the R-L relation, like that obtained by

TABLE 5.1. **The effects of absorption on the BH mass estimate: factors to be applied to the mass estimate for different A_V and z.**

L(3000 Å)					
Obs.	z	A_V=0.1	A_V=0.3	A_V=0.5	A_V=1
16274066	0.463	1.078	1.231	1.324	1.745
16274314	1.106	1.087	1.285	1.52	2.299
18350240	1.52	1.117	1.375	1.69	2.807
L(1350 Å)					
Obs.	z	A_V=0.1	A_V=0.3	A_V=0.5	A_V=1
18350240	1.52	1.069	1.456	1.976	4.219
42100302	1.94	1.243	1.816	2.644	6.695

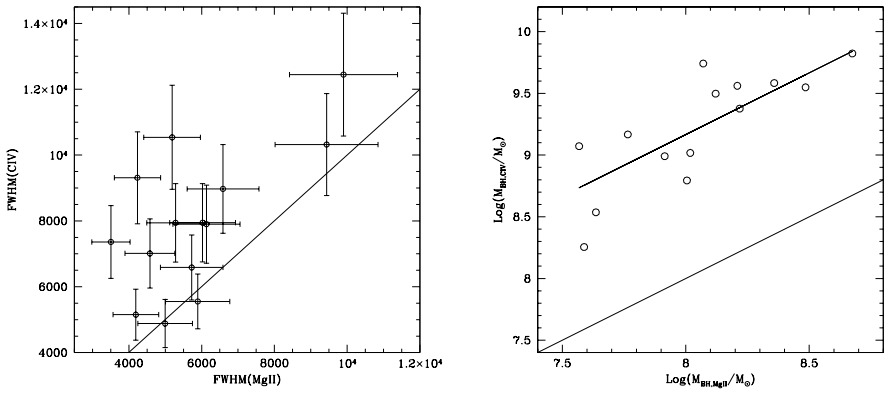

FIGURE 5.2. Left panel: Comparison between CIV and MgII FWHM, in Km/s. Right panel: the two mass estimates for 13 objects, and the best fit.

Mclure, would produce a mass estimate two times lower with respect to the original value of Kaspi et al. 1991 ($\beta = 0.7 \pm 0.03$).

We find the same result of Dietrich and Hamann 2004 who found a discrepancy of a factor of ~ 5 between MgII and CIV based estimates for their sample of high z QSO.

For our sample the discrepancy may be also partly explained by the difference in the FWHM of the emission lines, CIV beeing on average broader.

In order to have an homogeneous sample we rescaled the CIV mass estimate to the MgII one using the slope=1 best fitting relation displayed in Figure 2 (Log $M_{BH,CIV} =$ 1.148+ Log $M_{BH,MgII}$).

In Fig. 5.3 we show the black-hole masses and the Eddington ratio as functions of redshift for the full sample. As it as been reported in recent studies (McLure and Dunlop 2004) there appears to be an approximate upper limit for M_{BH} at $\approx 3 \times 10^9 M_\odot$.

Eddington ratios for spherical accretion were calculated assuming the bolometric correction, $L_{bol} = k \times L_X$, from Marconi et al. 2004.

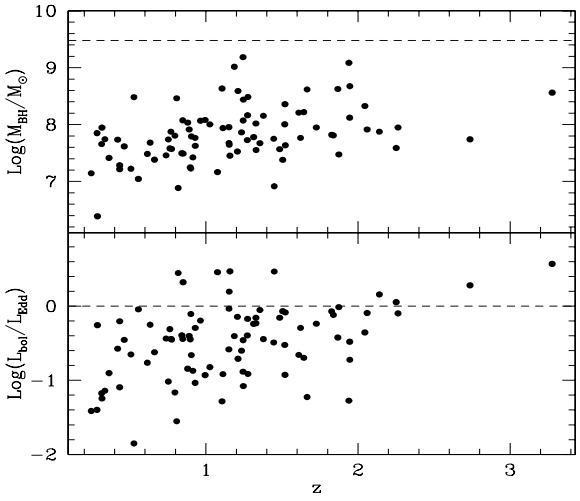

FIGURE 5.3. Left panel: Virial black hole mass estimate for the whole sample. Filled squares show the mean black hole mass within $\Delta z = 0.2$ bins. Right panel: Eddington ratio as a function of z. The solid line indicates the Eddington limit ($L_{bol} = L_{Edd}$).

Chapter 6

Conclusions

This thesis concerns the study of the cosmological evolution of Active Galactic Nuclei.

I carried out my work in the context of the HELLAS2XMM collaboration. HELLAS2XMM is a serendipitous survey that uses ten suitable XMM-Newton archive observations with the goal of covering ~ 2 square degrees of sky.
To date the survey covers ~ 1.5 square degrees and consists of a sample of 232 sources selected in the $2-10$ keV band at fluxes ranging over 6×10^{-15}–4×10^{-13} $erg\,cm^{-2}\,s^{-1}$ with nearly complete medium-deep optical photometry ($R = 24-25$), along with high S/N ratio optical spectra and broad-band (e.g. radio and near infrared) multiwavelength coverage.

The final aim of this project is to trace the accretion history in the Universe and to derive, over a wide range of redshifts and luminosities, the luminosity function of obscured AGNs with a level of statistical accuracy adequate for a meaningful comparison with that of the unobscured AGNs.

- **The survey**
  The HELLAS2XMM survey has provided optical identifications and spectroscopic classifications for 160 out of 232 hard X–ray selected sources: the spec-

troscopic completeness of the sample ($\sim 70\%$) is one of the highest for sources detected at our flux levels and our results represent a complementary and essential extension to results from deep, pencil–beam *Chandra* and XMM–*Newton* surveys.

The overall picture emerging from our results indicates a wide spread in the optical and X–ray properties of the HELLAS2XMM sample, confirming and extending results obtained from both deep and shallow surveys.
One of the most interesting results is that about 20% of the hard X–ray selected sources have an X–ray to optical flux ratio (X/O) ten times or more higher than that of optically selected AGN. Many of the extreme X/O sources in our sample have $R < 25$ so we have obtained their optical spectroscopy: we have confirmed that the large majority of these sources are type 2 QSO at moderate and high redshift.
These results strongly confirm that spectroscopic follow-up of high X/O selected in large area survey provides an efficient method to find high luminosity, narrow line objects and constitute the first spectroscopic proof over a statistically significant sample that high X/O sources (that constitute a significant fraction of the optically faint population) lie at $z > 1$.

Thanks to the optical identifications and classifications in the context of the HELLAS2XMM survey and fully exploiting shallow and ultra-deep data we have calibrated and tested a new statistical method to evaluate the properties of fainter, optically unidentifid obscured sources from other surveys.

- **The luminosity function**

  The measure of the evolution of the density of active galactic nuclei (AGN) is a key issue in order to trace the history of the accretion in the Universe and thus to understand the physics of the formation of both massive black holes and galaxies which are their hosts.

  To study the evolution of the hard X–ray luminosity function of AGN we have utilized two different approaches, statistical and parametric, combining the data from the full HELLAS2XMM sample with other existing flux limited samples in order to cover the widest possible range of luminosities and redshifts.
  Our results confirm that the evolution of the HXLF is best described by a

luminosity dependent density model up to z = 4.5, with lower luminosities sources dominating at lower redshifts.

Also we have found that the fraction of absorbed AGN increases with the decrease of the intrinsic luminosity of AGN and with the increase of the redshift, demonstrating also the key role of samples covering the widest strips of the luminosity–redshift plane.

- **Sources characterization**

  The study of the luminosity function of AGNs helps us to understand their evolution with cosmic time, but it is of fundamental importance to incorporate the formation and evolution of these sources into the wider scenario of formation and evolution of structure in the Universe.
  Comparison between observed data and models can provide key informations about galaxies and AGNs evolution and models itself.

  To constraint more tightly the specific predictions of the models we think that an effective approach is to compare them to mass or accretion rate selected AGN luminosity functions. This comparison can help in both disentangling among competing models, and understanding the role of relative feedbacks and delays between nuclear activity, star formation and galaxy evolution.

  A first step in this direction has been made performing a characterization of our sources through a detailed spectral and morfological study of our sample that allowed us to estimate the BH masses and accretion rates.
  We followed two different approaches:

  – Unobscured sources: we perferomed the analysis of the optical Broad Emission Lines that allowed us to make use of the correlation between the FWHM of these lines and BH masses to estimate the latter, and so their luminosity in terms of the Eddington one.

  – Obscured sources: we performed the morphological analysis of high X/O sources from HELLAS2XMM and CFDS-GOODS sample to use the well known relationship between black hole masses and the light of the bulges of the host galaxies evaluating, in this way, the black hole mass of our sources, and so their luminosity in terms of the Eddington one.

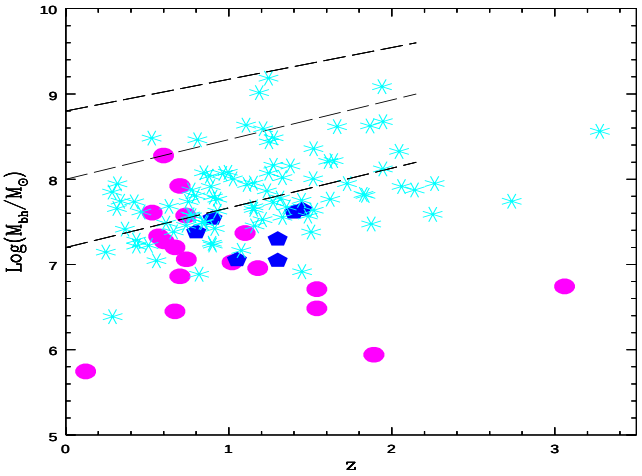

FIGURE 6.1. Black hole mass estimate versus redshift for our full sample: type 1 (cyan), HELLAS2XMM high X/O sources (blue), GOODS high X/O sources (magenta). Shaded lines delimit the region occupied by BH masses of type 1 sources from McLure and Dunlop 2004.

Our first results are shown in Fig. 6.1, Fig. 6.2.

Our preliminary analysis shows a good agreement with the results from McLure and Dunlop 2004.
Both BH masses and Eddington ratio can be seen to increase as a function of redshift confirming, at face value, an anti-hierarchical evolution of the SMBH population between z= 0 and z$\sim$ 2.5 The physical origin of such a behavior at redshift below 3 should be the combined effects of the decrease in the galaxy interaction rate in the era of the formation of groups and clusters, the expansion of the Universe affecting the gas cooling efficiency, the progressive depletion of the cold gas reservoirs within galaxies needed to power accretion and strong feedback from both stars and AGN.

The next step in our analysis will be the extension of the morphological study to the other photometric bands available for the CDFS–GOODS sample and the comparative study of ACS – K_S images in order to understand all the

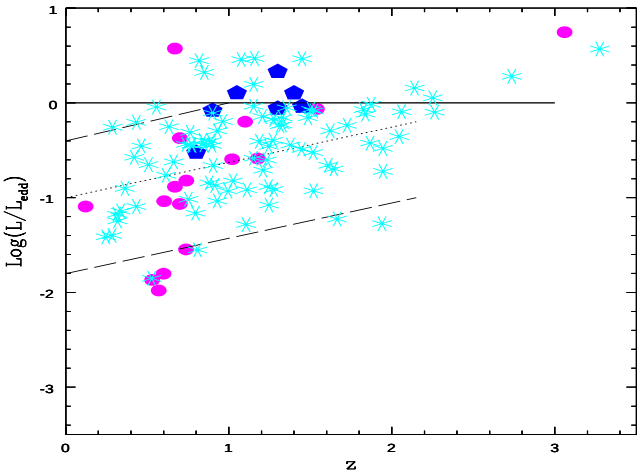

FIGURE 6.2. Bolometric luminosity as a fraction of the Eddington limit versus redshift for the full sample. Symbols as in Fig. 6.1. Shaded lines delimit the region occupied by L/L_{Edd} versus z from McLure and Dunlop 2004.

possible causes of the mismatch we found between the z and K_S derived BH masses.

Finally, we will compare mass and accretion rate selected AGN luminosity functions to the predictions of theoretical semi–analitical models of formation and evolution of structure in the Universe.

Bibliography

A., C. and F., F. (2004), "The density and masses of obscured Black Holes," *Baryons on Cosmic Structures, Astrophys.Space Sci.*, 294, 63.

Akiyama, M., Ohta, K., and Yamada, T. e. a. (2000), "Optical Identification of the ASCA Large Sky Survey," *ApJ*, 532, 700A.

Alexander, D. M., Vignali, C., Bauer, F. E., Brandt, W. N., Hornschemeier, A. E., Garmire, G. P., and Schneider, D. P. (2002), "The Chandra Deep Field North Survey. X. X-Ray Emission from Very Red Objects," *AJ*, 123, 1149.

Andredakis, Y. C. and Sanders, R. H. (1994), "Exponential bulges in late-type spirals: an improved description of the light distribution," *MNRAS*, 267, 283.

Antonucci, R. (1993), "Unified Models for Active Galactic Nuclei and Quasars," *ARA&A*, 31, 473.

Baggett, W. E., Baggett, S. M., and Anderson, K. S. J. (1998), "Bulge-Disk Decomposition of 659 Spiral and Lenticular Galaxy Brightness Profiles," *AJ*, 116, 1626.

Barcons, X., Carrera, F. J., Watson, M. G., McMahon, R. G., Aschenbach, B., Freyberg, M. J., Page, K., Page, M. J., Roberts, T. P., Turner, M. J. L., , and coauthors, . (2002), "The XMM-Newton serendipitous survey . II. First results from the AXIS high galactic latitude medium sensitivity survey," *A&A*, 382, 522.

Barger, A. J., Cowie, L. L., Bautz, M. W., Brandt, W. N., Garmire, G. P., Hornschemeier, A. E., Ivison, R. J., and Owen, F. N. (2001), "The Nature of the Hard X-Ray Background Sources: Optical, Near-Infrared, Submillimeter, and Radio Properties," *AJ*, 121, 662.

Barger, A. J., Cowie, L. L., Brandt, W. N., Capak, P., Garmire, G. P., Hornschemeier, A. E., Steffen, A. T., and Wehner, E. H. (2002), "X-Ray, Optical, and

Infrared Imaging and Spectral Properties of the 1 Ms Chandra Deep Field North Sources," *AJ*, 124, 1839.

Bassani, L., Dadina, M., and Maiolino, R. e. a. (1999), "A Three-dimensional Diagnostic Diagram for Seyfert 2 Galaxies: Probing X-Ray Absorption and Compton Thickness," *ApJS*, 121, 473B.

Beckert, T., Duschl, W. J., and Mezger, P. G. & Zylka, R. (1996), "Anatomy of the Sagittarius A complex. V. Interpretation of the SGR A* spectrum," *A&A*, 307, 450B.

Bender, R., Burstein, D., and Faber, S. M. (1992), "Dynamically hot galaxies. I - Structural properties," *ApJ*, 399, 462.

Bertin, E. and Arnouts, S. (1996), "SExtractor: Software for source extraction." *A&AS*, 117, 393.

Blandford, R. D. and Begelman, M. C. (1999), "On the fate of gas accreting at a low rate on to a black hole," *MNRAS*, 303, 1.

Boldt, E. and Leiter, D. (1987), "Constraints on possible precursor AGN sources of the cosmic X-ray background," *ApJ*, 322, 1.

Boroson, T. (1981), "The distribution of luminosity in spiral galaxies," *ApJS*, 46, 177.

Bragg, A. E., Greenhill, L. J., Moran, J. M., and Henkel, C. (2000), "Accelerations of Water Masers in NGC 4258," *ApJ*, 535, 73.

Brotherton, M. S., Tran, H. D., Becker, R. H., Gregg, M. D., Laurent-Muehleisen, S. A., and White, R. L. (2001), "Composite Spectra from the FIRST Bright Quasar Survey," *ApJ*, 546, 775.

Brusa, M., Comastri, A., and Mignoli, M. e. a. (2003), "The HELLAS2XMM survey. III. Multiwavelength observations of hard X-ray selected sources in the PKS 0312-77 field," *A&A*, 409, 65.

Bruzual A., G. and Charlot, S. (1993), "Spectral evolution of stellar populations using isochrone synthesis," *ApJ*, 405, 538.

Burstein, D. (1979), "Structure and origin of S0 galaxies. III - The luminosity distribution perpendicular to the plane of the disks in S0'," *ApJ*, 234, 829.

Byun, Y. I. and Freeman, K. C. (1995), "Two-dimensional Decomposition of Bulge and Disk," *ApJ*, 448, 563.

Carollo, C. M., Stiavelli, M., de Zeeuw, P. T., and Mack, J. (1997), "Spiral Galaxies with WFPC2.I.Nuclear Morphology, Bulges, Star Clusters, and Surface Brightness Profiles," *AJ*, 114, 2366.

Carollo, C. M., Stiavelli, M., and Mack, J. (1998), "Spiral Galaxies with WFPC2. II. The Nuclear Properties of 40 Objects," *AJ*, 116, 68.

Cavaliere, A. and Vittorini, V. (2000), "The Fall of the Quasar Population," *ApJ*, 543, 599.

Cavaliere, A., Lapi, A., and Menci, N. (2002), "Quasar Feedback on the Intracluster Medium," *ApJ*, 581, 1.

Ciliegi, P., Vignali, C., Comastri, A., Fiore, F., La Franca, F., and Perola, G. C. (2003), "The BeppoSAX High Energy Large Area Survey (HELLAS) - VI. The radio properties," *MNRAS*, 342, 575.

Coleman, G. D., Wu, C.-C., and Weedman, D. W. (1980), "Colors and magnitudes predicted for high redshift galaxies," *ApJS*, 43, 393.

Comastri, A., Setti, G., and Zamorani, G.and Hasinger, G. (1995), "The contribution of AGNs to the X-ray background," *A&A*, 296, 1.

Comastri, A., Fiore, F., Vignali, C., Matt, G., Perola, G. C., and La Franca, F. (2001), "The BeppoSAX High Energy Large Area Survey (HELLAS) - III. Testing synthesis models for the X-ray background," *MNRAS*, 327, 781.

Cowie, L. L., Barger, A. J., Bautz, M. W., Brandt, W. N., and Garmire, G. P. (2003), "The Redshift Evolution of the 2-8 keV X-Ray Luminosity Function," *ApJ*, 584, 57.

Croom, S. M.and Smith, R. J., Boyle, B. J., Shanks, T., Miller, L., Outram, P. J., and Loaring, N. S. (2004), "The 2dF QSO Redshift Survey - XII. The spectroscopic catalogue and luminosity function," *MNRAS*, 349, 1397.

de Jong, R. S. (1996), "Near-infrared and optical broadband surface photometry of 86 face-on disk dominated galaxies. II. A two-dimensional method to determine bulge and disk parameters." *A&A*, 118, 557.

Di Matteo, T., Croft, R. A. C., and Springel, V. e. a. (2003), "Black Hole Growth and Activity in a Λ Cold Dark Matter Universe," *ApJ*, 593, 56.

Dickey, J. M. and Lockman, F. J. (1990), "H I in the Galaxy," *ARA&A*, 28, 215.

Dietrich, M. and Hamann, F. (2004), "Implications of Quasar Black Hole Masses at High Redshifts," *ApJ*, 611, 761.

Djorgovski, S. and Davis, M. (1987), "Fundamental properties of elliptical galaxies," *ApJ*, 313, 59.

Dressler, A. (1980), "Galaxy morphology in rich clusters - Implications for the formation and evolution of galaxies." *ApJ*, 236, 351.

Dressler, A., Lynden-Bell, D., Burstein, D., Davies, R. L., Faber, S. M., Terlevich, R., and Wegner, G. (1987), "Spectroscopy and photometry of elliptical galaxies. I - A new distance estimator," *ApJ*, 313, 42.

Dunlop, J. S., McLure, R. J., Kukula, M. J., Baum, S. A., O'Dea, C. P., and Hughes, D. H. (2003), "Quasars, their host galaxies and their central black holes," *MNRAS*, 340, 1095.

Fabbiano, G., Kim, D.-W., and Trinchieri, G. (1992), "An X-ray catalog and atlas of galaxies," *ApJS*, 80, 531.

Faber, S. M., Tremaine, S., Ajhar, E. A., Byun, Y.-I., Dressler, A., Gebhardt, K., Grillmair, C., Kormendy, J., Lauer, T. R., and Richstone, D. (1997), "The Centers of Early-Type Galaxies with HST. IV. Central Parameter Relations." *AJ*, 114, 1771.

Fabian, A. (1996), "X-ray emission from Seyfert 1 galaxies and Quasars," *MPE Report*, p. 263.

Fabian, A. and Vaughan, S. (2003), "The iron line in MCG-6-30-15 from XMM-Newton: evidence for gravitational light bending?" *MNRAS*, 340L, 28F.

Ferrarese, L. (2002), "Beyond the Bulge: A Fundamental Relation between Supermassive Black Holes and Dark Matter Halos," *ApJ*, 578, 90F.

Ferrarese, L. and Merritt, D. (2000), "A Fundamental Relation between Supermassive Black Holes and Their Host Galaxies," *ApJ*, 539, 9.

Ferrarese, L., van den Bosch, F. C., Ford, H. C., Jaffe, W., and O'Connell, R. W. (1994), "Hubble Space Telescope photometry of the central regions of Virgo cluster elliptical galaxies. 3: Brightness profiles," *AJ*, 108, 1598.

Fiore, F., Antonelli, L. A., Ciliegi, P.and Comastri, A., Giommi, P., La Franca, F., Maiolino, R., Matt, G., Molendi, S., Perola, G. C., and Vignali, C. (2001a), "The BeppoSAX hellas survey: On the nature of faint hard X-ray selected sources," in *X-RAY ASTRONOMY: Stellar Endpoints,AGN, and the Diffuse X-ray Background*, eds. N. E. White, G. Malaguti, and G. G. Palumbo, vol. 599, p. 111.

Fiore, F., Giommi, P., Vignali, C., Comastri, A., Matt, G., Perola, G. C., La Franca, F., Molendi, S., Tamburelli, F., and Antonelli, L. A. (2001b), "The BeppoSAX High Energy Large Area Survey (HELLAS) - II. Number counts and X-ray spectral properties," *MNRAS*, 327, 771.

Fiore, F., Brusa, M., Cocchia, F., Baldi, A., Carangelo, N., Ciliegi, P., Comastri, A., La Franca, F., Maiolino, R., Matt, G., , and coauthors, . (2003), "The HELLAS2XMM survey. IV. Optical identifications and the evolution of the accretion luminosity in the Universe," *A&A*, 409, 79.

Franceschini, A., Silva, L., Fasano, G., Granato, G. L., Bressan, A., Arnouts, S., and Danese, L. (1998), "Early-Type Galaxies in the Hubble Deep Field: The Star Formation History," *ApJ*, 506, 600.

Franceschini, A., Hasinger, G., Miyaji, T., and Malquori, D. (1999), "On the relationship between galaxy formation and quasar evolution," *MNRAS*, 310, 5.

Franceschini, A., Braito, V., and Fadda, D. (2002), "Origin of the X-ray background and AGN unification: new perspectives," *MNRAS*, 335, 51.

Francis, P. J., Hewett, P. C., Foltz, C. B., Chaffee, F. H., Weymann, R. J., and Morris, S. L. (1991), "A high signal-to-noise ratio composite quasar spectrum," *ApJ*, 373, 465.

Gebhardt, K., Bender, R., Bower, G., Dressler, A., Faber, S. M., Filippenko, A. V., and Green, R. e. a. (2000), "A Relationship between Nuclear Black Hole Mass and Galaxy Velocity Dispersion," *ApJ*, 539, L13.

Genzel, R., Pichon, C., Eckart, A., Gerhard, O., and Ott, T. (2000), "Stellar dynamics in the Galactic Centre: proper motions and anisotropy," *MNRAS*, 317, 348.

Ghez, A. M., Klein, B. L., Morris, M., and Becklin, E. E. (1998), "High Proper-Motion Stars in the Vicinity of Sagittarius A*: Evidence for a Supermassive Black Hole at the Center of Our Galaxy," *ApJ*, 509, 678.

Giacconi, R. and Zamorani, G. (1987), "X–ray background, discrete sources, and diffuse processes," *ApJ*, 313, 20.

Giacconi, R., Gursky, H., Paolini, F. R., and Rossi, B. B. (1962), "Evidence for x Rays From Sources Outside the Solar System," *PhRvL*, 9, 439.

Giavalisco, M., Ferguson, H. C., Koekemoer, A. M., Dickinson, M., Alexander, D. M., Bauer, F. E., Bergeron, J., Biagetti, C., Brandt, W. N., Casertano, S., , and coauthors, . (2004), "The Great Observatories Origins Deep Survey: Initial Results from Optical and Near-Infrared Imaging," *ApJ*, 600, 93.

Gilli, R., Comastri, A., Brunetti, G., and Setti, G. (1999), "The contribution of AGN to the X-ray background: the effect of iron features," *NewA*, 4, 45.

Gilli, R., Salvati, M., and Hasinger, G. (2001), "Testing current synthesis models of the X-ray background," *A&A*, 366, 407.

Granato, G. L., De Zotti, G., Silva, L., Bressan, A., and Danese, L. (2004), "A Physical Model for the Coevolution of QSOs and Their Spheroidal Hosts," *ApJ*, 600, 580G.

Grossan, B. (1992), "Ph.D. thesis," *MIT*.

Haehnelt, M. G., Natarajan, P., and Rees, M. J. (1998), "High-redshift galaxies, their active nuclei and central black holes," *MNRAS*, 300, 81.

Hartwick, F. D. A. and Schade, D. (1990), "The space distribution of quasars," *ARA&A*, 28, 437.

Hasinger, G. (2003), "Formation and Evolution of Supermassive Black Holes in Galactic Centers: Observational Constraints," *The Emergence of Cosmic Structure*, Stephen S. Holt and Chris Reynolds (eds), 227.

Hasinger, G., Altieri, B., Arnaud, M., Barcons, X., Bergeron, J., Brunner, H., Dadina, M., Dennerl, K., Ferrando, P., Finoguenov, A., , and coauthors, . (2001), "XMM-Newton observation of the Lockman Hole. I. The X-ray data," *A&A*, 365, 45.

Heckman, T. M., Kauffmann, G., Brinchmann, J., Charlot, S., Tremonti, C., and White, S. D. M. (2004), "Present-Day Growth of Black Holes and Bulges: The Sloan Digital Sky Survey Perspective," *ApJ*, 613, 109H.

Herrnstein, J. R., Greenhill, L. J., and Moran, J. M. (1996), "The Warp in the Subparsec Molecular Disk in NGC4258 as an Explanation for Persistent Asymmetries in the Maser Spectrum," *ApJ*, 468, L17.

Ho, L. C. and Peng, C. Y. (2001), "Nuclear Luminosities and Radio Loudness of Seyfert Nuclei," *ApJ*, 555, 650.

Ho, L. C., Filippenko, A. V., and Sargent, W. L. W. (1997), "A Search for "Dwarf" Seyfert Nuclei. V. Demographics of Nuclear Activity in Nearby Galaxies," *ApJ*, 487, 568.

Hornschemeier, A. E., Brandt, W. N., Garmire, G. P., Schneider, D. P., Barger, A. J., Broos, P. S., Cowie, L. L., Townsley, L. K., Bautz, M. W., Burrows, D. N., , and coauthors, . (2001), "The Chandra Deep Survey of the Hubble Deep Field-North Area. II. Results from the Caltech Faint Field Galaxy Redshift Survey Area," *ApJ*, 554, 742.

Iwasawa, K., Fabian, A. C., Reynolds, C. S., Nandra, K., Otani, C., and Inoue, H. a. (1996), "The variable iron K emission line in MCG-6-30-15," *MNRAS*, 282, 1038I.

Jaffe, W., Ford, H. C., O'Connell, R. W., van den Bosch, F. C., and Ferrarese, L. (1994), "Hubble Space Telescope photometry of the central regions of Virgo Cluster elliptical galaxies. 1: Observations, discussion, and conclusions," *AJ*, 108, 1567.

Jansen, F., Lumb, D., Altieri, B., Clavel, J., Ehle, M., Erd, C., Gabriel, C., Guainazzi, M., Gondoin, P., Much, R., , and coauthors, . (2001), "XMM-Newton observatory. I. The spacecraft and operations," *A&A*, 365, 1.

Jenkins, A., Frenk, C. S., White, S. D. M., Colberg, J. M., Cole, S., Evrard, A. E., Couchman, H. M. P., and Yoshida, N. (2001), "The mass function of dark matter haloes," *MNRAS*, 321, 372.

Kadler, M., Ros, E., Kerp, J., Roy, A. L., Marscher, A. P., and Zensus, J. A. (2005), "A Multiband Approach to AGN: Radioscopy and Radio Astronomy," *MmSAI*, 76, 126.

Kaspi, S., Smith, P. S., Netzer, H., Maoz, D., Jannuzi, B. T., and Giveon, U. (1991), "Reverberation Measurements for 17 Quasars and the Size-Mass-Luminosity Relations in Active Galactic Nuclei," *ApJ*, 533, 631.

Kauffmann, G., Heckman, T. M., and Tremonti, C. e. a. (2003), "The host galaxies of active galactic nuclei," *MNRAS*, 346, 1055K.

Kent, S. M. (1985), "CCD surface photometry of field Galaxies. II - Bulge/disk decompositions," *ApJS*, 59, 115.

Kent, S. M., Dame, T. M., and Fazio, G. (1991), "Galactic structure from the Spacelab infrared telescope. II - Luminosity models of the Milky Way," *ApJ*, 378, 131.

Khosroshahi, H. G., Wadadekar, Y., and Kembhavi, A. (2000), "Correlations among Global Photometric Properties of Disk Galaxies," *ApJ*, 533, 162.

Kormendy, J. (1977), "Brightness distributions in compact and normal galaxies. III - Decomposition of observed profiles into spheroid and disk," *ApJ*, 217, 406.

Kormendy, J. and Bruzual A., G. (1978), "The minor-axis brightness profile of the spiral galaxy NGC 4565 and the problem of massive halos," *ApJ*, 223, 63.

Kormendy, J. and Gebhardt, K. (2001), "Supermassive Black Holes in Galactic Nuclei," *AIPC*, 586, 363.

Koyama, K., Maeda, Y., Sonobe, T., Takeshima, T., Tanaka, Y., and Yamauchi, S. (1996), "ASCA View of Our Galactic Center: Remains of Past Activities in X-Rays?" *PASJ*, 48, 249.

La Franca, F. and Cristiani, S. (1997), "The QSO Evolution Derived from the HBQS and Other Complete QSO Surveys," *AJ*, 113, 1517.

La Franca, F., Fiore, F., Vignali, C., Antonelli, A., Comastri, A., Giommi, P., Matt, G., Molendi, S., Perola, G. C., and Pompilio, F. (2002), "The BeppoSAX High-Energy Large-Area Survey. V. The Nature of the Hard X-Ray Source Population and Its Evolution," *ApJ*, 570, 100.

Lauer, T. R., Ajhar, E. A., Byun, Y.-I., Dressler, A., Faber, S. M., Grillmair, C., Kormendy, J., Richstone, D., and Tremaine, S. (1995), "The Centers of Early-Type Galaxies with HST.I.An Observational Survey," *AJ*, 110, 2622.

Lehmann, I., Hasinger, G., Schmidt, M., Giacconi, R., Trmper, J., Zamorani, G., Gunn, J. E., Pozzetti, L., Schneider, D. P., and Stanke, T. (2001), "The ROSAT Deep Survey. VI. X-ray sources and Optical identifications of the Ultra Deep Survey," *A&A*, 371, 833.

Lilly, S., Schade, D., Ellis, R., Le Fevre, O., Brinchmann, J., Tresse, L., Abraham, R., Hammer, F., Crampton, D., Colless, M., , and coauthors, . (1998), "Hubble Space Telescope Imaging of the CFRS and LDSS Redshift Surveys. II. Structural

Parameters and the Evolution of Disk Galaxies to Z approximately 1," *ApJ*, 500, 75.

Lilly, S. J., Tresse, L., Hammer, F., Crampton, D., and Le Fevre, O. (1995), "The Canada-France Redshift Survey. VI. Evolution of the Galaxy Luminosity Function to Z approximately 1," *ApJ*, 455, 108.

Livio, M., Pringle, J. E., and King, A. R. (2003), "The Disk-Jet Connection in Microquasars and Active Galactic Nuclei," *ApJ*, 593, 184.

Magorrian, J., Tremaine, S., Richstone, D., Bender, R., Bower, G., and Dressler, A. e. a. (1998), "The Demography of Massive Dark Objects in Galaxy Centers," *AJ*, 115, 2285.

Mainieri, V., Bergeron, J., Hasinger, G., Lehmann, I., Rosati, P., Schmidt, M., Szokoly, G., and Della Ceca, R. (2002), "XMM-Newton observation of the Lockman Hole. II. Spectral analysis," *A&A*, 393, 425.

Maiolino, R. and Rieke, G. H. (1995), "Low-Luminosity and Obscured Seyfert Nuclei in Nearby Galaxies," *ApJ*, 454, 95.

Maiolino, R., Salvati, M., Bassani, L., Dadina, M., della Ceca, R., Matt, G., Risaliti, G., and Zamorani, G. (1998), "Heavy obscuration in X-ray weak AGNs," *A&A*, 338, 781.

Maiolino, R., Marconi, A., Salvati, M., Risaliti, G., Severgnini, P., Oliva, E., La Franca, F., and Vanzi, L. (2001), "Dust in active nuclei. I. Evidence for "anomalous" properties," *A&A*, 365, 28M.

Marconi, A. and Hunt, L. K. (2003), "The Relation between Black Hole Mass, Bulge Mass, and Near-Infrared Luminosity," *ApJ*, 589, 21.

Marconi, A., Risaliti, G., Gilli, R., Hunt, L. K., Maiolino, R., and Salvati, M. (2004), "Local supermassive black holes, relics of active galactic nuclei and the X-ray background," *MNRAS*, 351, 169.

Marleau, F. R. and Simard, L. (1998), "Quantitative Morphology of Galaxies in the Hubble Deep Field," *ApJ*, 507, 585.

Marshall, F. E., Boldt, E. A., Holt, S. S., Miller, R. B., Mushotzky, R. F., Rose, L. A., Rothschild, R. E., and Serlemitsos, P. J. (1980), "The diffuse X-ray background spectrum from 3 to 50 keV," *ApJ*, 235, 4.

Mather, J. C., Cheng, E. S., Eplee, R. E., J., Isaacman, R. B., Meyer, S. S., Shafer, R. A., Weiss, R., Wright, E. L., Bennett, C. L., Boggess, N. W., , and coauthors, . (1990), "A preliminary measurement of the cosmic microwave background spectrum by the Cosmic Background Explorer (COBE) satellite," *ApJ*, 354, 37.

Matt, G. (1997), "The X-ray spectrum of Compton-thick Seyfert 2 galaxies," *MmSAI*, 68, 127.

McLure, R. J. and Dunlop, J. S. (2002), "On the black hole-bulge mass relation in active and inactive galaxies," *MNRAS*, 331, 795M.

McLure, R. J. and Dunlop, J. S. (2004), "The cosmological evolution of quasar black hole masses," *MNRAS*, 352, 1390.

McLure, R. J. and Jarvis, M. J. (2002), "Measuring the black hole masses of high-redshift quasars," *MNRAS*, 337, 109.

Menci, N.and Fiore, F., Perola, G. C., and Cavaliere, A. (2004), "X-Ray Evolution of Active Galactic Nuclei and Hierarchical Galaxy Formation," *ApJ*, 606, 58.

Menci, N., Cavaliere, A., Fontana, A., Giallongo, E., Poli, F., and Vittorini, V. (2003), "Quasar Evolution Driven by Galaxy Encounters in Hierarchical Structures," *ApJ*, 587, 63.

Merloni, A., Rudnick, G., and Di Matteo, T. (2004), "Tracing the cosmological assembly of stars and supermassive black holes in galaxies," *MNRAS*, 354, 37.

Mignoli, M., Pozzetti, L., Comastri, A., Brusa, M., Ciliegi, P., Cocchia, F., Fiore, F., La Franca, F., Maiolino, R., Matt, G., , and coauthors, . (2004), "The HELLAS2XMM survey. V. Near-Infrared observations of X-ray sources with extreme X/O ratios," *A&A*, 418, 827.

Miyaji, T., Hasinger, G., and Schmidt, M. (2000), "Soft X-ray AGN luminosity function from it ROSAT surveys. I. Cosmological evolution and contribution to the soft X-ray background," *A&A*, 353, 25.

Miyaji, T., Hasinger, G., and Schmidt, M. (2001), "Soft X-ray AGN luminosity function from it ROSAT surveys. II. Table of the binned soft X-ray luminosity function," *A&A*, 369, 49.

Miyoshi, M., Moran, J., Herrnstein, J., Greenhill, L., Nakai, N., Diamond, P., and Inoue, M. (1995), "Evidence for a Black-Hole from High Rotation Velocities in a Sub-Parsec Region of NGC4258," *Nature*, 373, 127.

Monaco, P., Salucci, P., and Danese, L. (2000), "Joint cosmological formation of QSOs and bulge-dominated galaxies," *MNRAS*, 311, 279M.

Moran, E. C., Barth, A. J., Kay, L. E., and Filippenko, A. V. (2000), "The Frequency of Polarized Broad Emission Lines in Type 2 Seyfert Galaxies," *ApJ*, 540, 73.

Moretti, A., Campana, S., Lazzati, D., and Tagliaferri, G. (2003), "The Resolved Fraction of the Cosmic X-Ray Background," *ApJ*, 588, 696.

Mukherjee, R., Bttcher, M., Hartman, R. C., Sreekumar, P., Thompson, D. J., Mahoney, W. A., Pursimo, T., Sillanp, A., and Takalo, L. O. (1999), "Broadband Spectral Analysis of PKS 0528+134: A Report on Six Years of EGRET Observations," *ApJ*, 527, 132.

Mushotzky, R. F., Fabian, A. C., Iwasawa, K., Kunieda, H., Matsuoka, M., Nandra, K., and Tanaka, Y. (1995), "Detection of broad iron K lines in active galaxies," *MNRAS*, 272L, 9M.

Nandra, K. and Pounds, K. (1994), "GINGA Observations of the X-Ray Spectra of Seyfert Galaxies," *MNRAS*, 268, 405.

Nandra, K., George, I. M., Mushotzky, R. F., Turner, T. J., and Yaqoob, T. (1997), "ASCA Observations of Seyfert 1 Galaxies. II. Relativistic Iron K alpha Emission," *ApJ*, 477, 602N.

Page, M. J., McHardy, I. M., Gunn, K. F., Loaring, N. S., Mason, K. O., Sasseen, T., Newsam, A., Ware, A., Kennea, J., Sekiguchi, K., and Takata, T. (2003), "X-ray and optical properties of X-ray sources in the 13hr XMM-Newton/Chandra deep survey," *AN*, 324, 101.

Pahre, M. A., Djorgovski, S. G., and de Carvalho, R. R. (1998), "Near-Infrared Imaging of Early-Type Galaxies. III. The Near-Infrared Fundamental Plane," *AJ*, 116, 159.

Panessa, F. and Bassani, L. (2002), "Unabsorbed Seyfert 2 galaxies," *A&A*, 394, 435.

Pappa, A., Georgantopoulos, I., Stewart, G. C., and Zezas, A. L. (2001), "The X-ray spectra of optically selected Seyfert 2 galaxies: are there any Seyfert 2 galaxies with no absorption?" *MNRAS*, 326, 995.

Pariev, V. I., Bromley, B. C., and Miller, W. A. (2001), "Estimation of Relativistic Accretion Disk Parameters From Iron Line Emission," *ApJ*, 547, 649P.

Peng, C. Y., Ho, L. C., Impey, C. D., and Rix, H.-W. (2002), "Detailed Structural Decomposition of Galaxy Images," *AJ*, 124, 266.

Pentericci, L., Rix, H.-W., Prada, F., Fan, X., Strauss, M. A., Schneider, D. P., Grebel, E. K., Harbeck, D., Brinkmann, J., and Narayanan, V. K. (2003), "The near-IR properties and continuum shapes of high redshift quasars from the Sloan Digital Sky Survey," *A&A*, 410, 75P.

Perola, G. C., Puccetti, S., Fiore, F., Sacchi, N., Brusa, M., Cocchia, F., Baldi, A., Carangelo, N., Ciliegi, P., and Comastri, A. a. (2004), "The HELLAS2XMM survey. VI. X-ray absorption in the 1df AGN sample through a spectral analysis," *A&A*, 421, 491P.

Petrucci, P. (2002), "The formation of the Seyfert continuum," astro-ph/0212235.

Phillips, A. C., Illingworth, G. D., MacKenty, J. W., and Franx, M. (1996), "Nuclei of Nearby Disk Galaxies.I.A Hubble Space Telescope Imaging Survey," *AJ*, 111, 1566.

Pohlen, M., Dettmar, R., and Ltticke, R. (1979), "Cut-off radii of galactic disks. A new statistical study on the truncation of galactic disks," *A&A*, 38, 15.

Pompilio, F., La Franca, F., and Matt, G. (2000), "The X-ray background and the evolution of AGN," *A&A*, 353, 440.

Pozzetti, L., Cimatti, A., Zamorani, G., Daddi, E., Menci, N., Fontana, A., Renzini, A., Mignoli, M., Poli, F., Saracco, P., , and coauthors, . (2003), "The K20 survey. V. The evolution of the near-IR Luminosity Function," *A&A*, 402, 837.

Predehl, P. and Truemper, J. (1994), "ROSAT observation of the SGR A region," *A&A*, 290L, 29P.

Press, W. H., Teukolsky, S. A., Vetterling, W. T., and Flannery, B. P. (1997)*Numerical Recipes in C (Cambridge: Cambridge Univ. Press)*.

Ptak, A., Yaqoob, T., Serlemitsos, P. J., Kunieda, H., and Terashima, Y. (1996), "The Nature of the Low-Luminosity Active Galactic Nuclei in NGC 3147," *ApJ*, 459, 542.

Ravindranath, S., Ho, L. C., Peng, C. Y., Filippenko, A. V., and Sargent, W. L. W. (2001), "Central Structural Parameters of Early-Type Galaxies as Viewed with Nicmos on the Hubble Space Telescope," *AJ*, 122, 653.

Ravindranath, S., Ho, L. C., and Filippenko, A. V. (2002), "Nuclear Cusps and Cores in Early-Type Galaxies as Relics of Binary Black Hole Mergers," *ApJ*, 566, 80.

Rest, A., van den Bosch, F. C., Jaffe, W., Tran, H., Tsvetanov, Z., Ford, H. C., Davies, J., and Schafer, J. (2001), "WFPC2 Images of the Central Regions of Early-Type Galaxies. I. The Data," *AJ*, 121, 2431.

Richards, G. T., Hall, P. B., Vanden Berk, D. E., Strauss, M. A., Schneider, D. P., Weinstein, M. A., Reichard, T. A., York, D. G., Knapp, G. R., Fan, X., , and coauthors, . (2003), "Red and Reddened Quasars in the Sloan Digital Sky Survey," *AJ*, 126, 1131.

Risaliti, G., Maiolino, R., and Salvati, M. (1999), "The Distribution of Absorbing Column Densities among Seyfert 2 Galaxies," *ApJ*, 522, 157.

Rogers, A. E. E., Doeleman, S., Wright, M. C. H., Bower, G. C., Backer, D. C., Padin, S., Philips, J. A., Emerson, D. T., Greenhill, L., Moran, J. M., and Kellermann, K. I. (1994), "Small-scale structure and position of Sagittarius A(*) from VLBI at 3 millimeter wavelength," *ApJ*, 434L, 59R.

Sarzi, M., Rix, H.-W., Shields, J. C., Rudnick, G., Ho, L. C., McIntosh, D. H., Filippenko, A. V., and Sargent, W. L. W. (2001), "Supermassive Black Holes in Bulges," *ApJ*, 550, 65.

Schmidt, M. (1968), "Space Distribution and Luminosity Functions of Quasi-Stellar Radio Sources," *ApJ*, 151, 393.

Schmidt, M. and Green, R. F. (1986), "Counts, evolution, and background contribution of X-ray quasars and other extragalactic X-ray sources," *ApJ*, 305, 68.

Serabyn, E., Carlstrom, J., Lay, O., Lis, D. C., Hunter, T. R., and Lacy, J. H. (1997), "High Frequency Measurements of the Spectrum of SGR A*," *ApJ*, 490L, 77S.

Setti, G. and Woltjer, L. (1989), "Active Galactic Nuclei and the spectrum of the X-ray background," *A&A*, 224, 21.

Shafer, R. A. and Fabian, A. C. (1983), "The (an)isotropy of the X-ray sky," *IAUS*, 104, 333.

Shankar, F., Salucci, P., Granato, G. L., De Zotti, G., and Danese, L. (2004), "Supermassive black hole demography: the match between the local and accreted mass functions," *MNRAS*, 354, 1020.

Shaw, M. A. and Gilmore, G. (1989), "The luminosity distributions of edge-on spiral galaxies. I - A two-dimensional model and its application to NGC 891 and 4565," *MNRAS*, 237, 903.

Sheth, R. K. and Tormen, G. (1999), "Large-scale bias and the peak background split," *MNRAS*, 308, 119.

Shields, G. A., Gebhardt, K., Salviander, S., Wills, B. J., Xie, B., Brotherton, M. S., Yuan, J., and Dietrich, M. (2003), "The Black Hole-Bulge Relationship in Quasars," *ApJ*, 583, 124S.

Silk, J. and Rees, M. J. (1998), "Quasars and galaxy formation," *A&A*, 331L, 1S.

Simard, L. (1998), "GIM2D: an IRAF package for the Quantitative Morphology Analysis of Distant Galaxies," *Astronomical Data Analysis Software and Systems VII, A.S.P. Conference Series, 1998, R. Albrecht, R.N. Hook and H.A. Bushouse, eds.*, 145, 108.

Tanaka, Y., Nandra, K., Fabian, A. C., Inoue, H., Otani, C., Dotani, T., Hayashida, K., Iwasawa, K., Kii, T., and Kunieda, H. a. (1995), "Gravitationally Redshifted Emission Implying an Accretion Disk and Massive Black-Hole in the Active Galaxy MCG:-6-30-15," *Nature*, 375, 659.

Tomita, A., Aoki, K., Watanabe, M., Takata, T., and Ichikawa, S.-i. (2000), "The Central Gas Systems of Early-Type Galaxies Traced by Dust Features, Based on the Hubble Space Telescope WFPC2 Archival Images," *AJ*, 120, 123.

Tozzi, P., Rosati, P., Nonino, M., Bergeron, J., Borgani, S., Gilli, R., Gilmozzi, R., Hasinger, G., Grogin, N., Kewley, L., , and coauthors, . (2001), "New Results from the X-Ray and Optical Survey of the Chandra Deep Field-South: The 300 Kilosecond Exposure. II." *ApJ*, 562, 42.

Tran, H. D. (2001), "Hidden Broad-Line Seyfert 2 Galaxies in the CFA and 12 μM Samples," *ApJ*, 554, 19.

Tran, H. D., Tsvetanov, Z., Ford, H. C., Davies, J., Jaffe, W., van den Bosch, F. C., and Rest, A. (2001), "Dusty Nuclear Disks and Filaments in Early-Type Galaxies," *AJ*, 121, 2928.

Tremaine, S., Gebhardt, K., Bender, R., Bower, G., Dressler, A., Faber, S. M., and Filippenko, A. V. (2002), "The Slope of the Black Hole Mass versus Velocity Dispersion Correlation," *ApJ*, 574, 740T.

Tully, R. B. and Fisher, J. R. (1977), "A new method of determining distances to galaxies," *A&A*, 54, 661.

Turner, T. J., George, I. M., Nandra, K., and Mushotzky, R. F. (1997), "ASCA Observations of Type 2 Seyfert Galaxies. I. Data Analysis Results," *ApJS*, 113, 23.

Turner, T. J., Perola, G. C., Fiore, F., Matt, G., George, I. M., Piro, L., and Bassani, L. (2000), "BeppoSAX Observation of NGC 7582: Constraints on the X-Ray Absorber," *ApJ*, 531, 245.

Ueda, Y., Akiyama, M., Ohta, K., and Miyaji, T. (2003), "Cosmological Evolution of the Hard X-Ray Active Galactic Nucleus Luminosity Function and the Origin of the Hard X-Ray Background," *ApJ*, 598, 886.

van der Kruit, P. C. (1979), "Optical surface photometry of eight spiral galaxies studied in Westerbork," *A&AS*, 38, 15.

van Dokkum, P. G. and Franx, M. (2001), "Morphological Evolution and the Ages of Early-Type Galaxies in Clusters," *ApJ*, 553, 90.

Vestergaard, M. and Wilkes, B. J. (2001), "An Empirical Ultraviolet Template for Iron Emission in Quasars as Derived from I Zwicky 1," *ApJS*, 134, 1.

Wadadekar, Y., Robbason, B., and Kembhavi, A. (1999), "Two-dimensional Galaxy Image Decomposition," *AJ*, 117, 1219.

Weisskopf, M. C., Brinkman, B., Canizares, C., Garmire, G., Murray, S., and Van Speybroeck, L. P. (2002), "An Overview of the Performance and Scientific Results from the Chandra X-Ray Observatory," *PASP*, 114, 1.

Wilkes, B. J., Schmidt, G. D., Cutri, R. M., Ghosh, H., Hines, D. C., Nelson, B., and Smith, P. S. (2002), "The X-Ray Properties of 2MASS Red Active Galactic Nuclei," *ApJ*, 564L, 65W.

Wyithe, J. S. B. and Loeb, A. (2003), "Self-regulated Growth of Supermassive Black Holes in Galaxies as the Origin of the Optical and X-Ray Luminosity Functions of Quasars," *ApJ*, 595, 614W.

Yamauchi, S., Kawada, M., Koyama, K., Kunieda, H., and Tawara, Y. (1990), "Optically thin hot plasma near the Galactic center - Mapping observations of the 6.7 keV iron line," *ApJ*, 365, 532.

Yu, Q. and Tremaine, S. (2002), "Observational constraints on growth of massive black holes," *MNRAS*, 335, 965.